ALMA MATER STUDIORUM
UNIVERSITÀ DI BOLOGNA

DOTTORATO DI RICERCA IN
CHIMICA

Ciclo XXXVI

Settore Concorsuale: 03/C2

Settore Scientifico Disciplinare: CHIM/04

Zirconia-based catalytic systems for the valorisation of biomass in chemical products of high industrial interest: an experimental and computational study

Presentata da: Alessia Ventimiglia

Coordinatore Dottorato

Prof. Luca Prodi

Supervisore

Prof. Nikolaos Dimitratos

Co-Supervisori

Prof. Ivan Rivalta

Prof. Stefania Albonetti

Esame Finale anno 2024

Index

Abstract

Nowadays, the optimization of industrial processes more sustainable from an environmental point of view is a central theme to deal with the problems generated by pollution and climate change. The use of renewable raw sources is a fundamental starting point. Among these, lignocellulosic biomass has a great potential to obtain products of high industrial interest. Zirconia is a particularly promising material as heterogeneous catalyst: in fact, thanks to its innumerable properties, it can be used for a large number of reactions, both as an actual catalyst and as a support for nanoparticles.

In this thesis work, various reactions, both oxidations and hydrogenations, for the valorisation of biomass were studied using zirconia-based catalysts in the gas phase and liquid phase.

The hydrogenation reaction of methyl levulinate (ML) in continuous gas phase by CTH mechanism was studied, using alcohols such as H-donor. For this reaction, the two crystalline phases of zirconia were compared, the tetragonal (t-ZrO_2) and the monoclinic (m-ZrO_2): these were synthesized and subsequently characterized using XRD, BET and TPD techniques. From the results obtained it was seen that the desired crystalline phases were obtained with comparable surface areas. The TPD analysis allowed to evaluate the strength and density of the acidic and basic sites. From the catalytic tests carried out, t-ZrO_2 was more active in the reaction in question and more selective towards the formation of GVL (yield of 63%). m-ZrO_2, however, was found to deactivate more quickly. Through material characterizations, combined with computational and NMR spectroscopy studies, it has been seen that t-ZrO_2 tends to adsorb ethanol, the H-donor, more strongly; in this way, in addition to activating it for the CTH reaction, it limits the adsorption of the intermediate angelica lactone (AL), which on the catalytic surface tends to polymerize and poison the reactive sites. At the same time, m-ZrO_2, having stronger basic sites, confirmed by TPD analysis and computational studies, interacts more with AL, deactivating more quickly.

Other zirconia-based materials with higher surface areas, compared to crystalline zirconia, have been subsequently tested, with the aim of pushing the reaction further towards consecutive products, such as Pentenoates, products interested in obtaining Pentanoates. Among these, $ZrSi_{30}$ was found to be the most active and selective for the formation of Ethyl Pentenoates (EP). In particular, with a 1:20 ML:EtOH molar ratio, the ML conversion was total for the ten hours of reactions, with EP yields between 68% and 73% from 185 min of reaction onwards.

During a period of research abroad at the Université de Lille, catalysts based on metal nanoparticles supported on commercial zirconia were synthesized using the sol-immobilization technique based on Au and Pd, both mono and bimetallic. These have been tested for:

- liquid phase reaction of hydrogenation of furfural by CTH mechanism using isopropanol as H-donor
- oxidation reaction of HMF in the liquid phase, using O_2 as an oxidizing agent

For the furfural hydrogenation reaction, the most active and selective catalyst for the formation of Furfuryl alcohol (FA) was found to be Pd 0.5%wt/ZrO_2 (61192), with a FA yield of 55% and a conversion of 76 % in optimized reaction conditions (t=2h; T=130°C; rpm=600; PN_2=20 bar). It has been seen that as the quantity of gold increases, the selectivity of the reaction tends to shift towards the formation of isopropoxymethylfuran (IPF).

For the HMF oxidation reaction, the most active catalyst was found to be the bimetallic Au:Pd(3:1)/ZrO_2 (61192). The presence of gold, in fact, tends to dilute the Pd nanoparticles, keeping them separate and increasing their activity. Increasing the Au:Pd ratio in bimetallic catalysts resulted in an increase in catalytic activity.

The catalysts with the best catalytic performances were characterized by XPS and TEM-EDX technique.

Finally, the oxidation reaction of glucose (GLU) to glucaric acid (GLA) was studied computationally. Gold clusters of 55 atoms were modelled and the adsorption of some target molecules for the reaction was studied on these. From the results obtained it was seen that, by carrying out the reaction in the presence of a base (NaOH), GLA tends to adsorb more strongly than GLU and the intermediate gluconic acid on the surface of the catalyst: this is due to the presence of an additional carboxylic acid group, which tends to form a network of hydrogen bonds with the hydroxyl groups present on the cluster, leading to a deactivation of the catalyst in a short time. The interaction of three stabilizing agents, PVA, PEG and PVP with the gold cluster was also studied. It has been seen that PVA tends to interact less with the cluster than the other two stabilizers. As a result, it is washed away more easily, leaving the catalytic sites free.

Abbreviations

Angelica lactone (AL)

Catalytic Transfer Hydrogenation (CTH)

Deposition-Precipitation method (DP)

2,5-diformylfuran (DFF)

Ethyl levulinate (EL)

Flame ionization detector (FID)

5-formyl-2-furancarboxylic acid (FFCA)

Furandicarboxylic acid (FDCA)

Furfural diisopropyl acetal (FDIA)

Furfuryl alcohol (FA)

ɣ-valerolactone (GVL)

Gas chromatograph (GC)

Glucaric Acid (GLA)

Gluconic Acid (GLO)

Glucose (GLU)

High Performance Liquid Chromatography (HPLC)

5-hydroxymethyl-2-furancarboxylic acid (HMFCA)

Hydroxymethylfurfural (HMF)

Imprenation method (IMP)

Incipient wetness impregnation (IW-IMP)

2-(isopropoxy)methyl furan (IPF)

Levulinic acid (LA)

Levulinic ester (LE)

Methyl levulinate (ML)

Mass spectrometer (MS)

Methyltetrahydrofuran (MTHF)

Monoclinic zirconia (m-ZrO_2)

Nanoparticle (NP)

Polyethylenglicole (PEG)

Polyvinylpirrolidone (PVP)

Polyvinyl alcohol (PVA)

Screening Pressure Reactor (SPR)

Sol-immobilization technique (SOL-IM)

Tetragonal zirconia (t-ZrO_2)

Zirconia (ZrO_2)

1. Introduction

1.1 **Biomass: an important alternative to fossil resources to combat climate change**

In recent years, climate change turns out to be increasingly a hot topic. In fact, global warming is bringing numerous changes to the balance of the planet, generating catastrophes that are putting the lives of human beings and other forms of life at risk. Hurricanes, storms, harm to agriculture and forests, species extinctions and ecosystem damage are just some of the currently visible effects, which are causing thousands of victims and numerous damages also from an economic point of view. In particular, EPA determined in 2009 that emissions of greenhouse gases, mainly produced by human activities, such as CO_2, CH_4, N_2O and fluorinated gases, are the main cause of global warming, because they trap heat in the atmosphere.

Those who will suffer most from the effect of this climate change are future generations. Several scientific bodies have emphasized the fact that it is necessary to act as soon as possible to counter the production of greenhouse gases, which persist in the atmosphere for a very long period.

For all these reasons, in recent years the use of renewable raw materials, i.e. biomass, becomes a crucial issue for the future of the chemical process industries.

In the early 1990s, the concept of "Green Chemistry" was introduced for the first time in the U.S. environmental Protection Agency (EPA) [1]. In particular, The Pollution Prevention Act has highlighted the fact that, instead of treating waste from chemical processes, the problem must be tackled "upstream", using raw materials more efficiently. Green chemistry has therefore been universally defined as the design of the chemical process which reduces the production of toxic substances as much as possible. John Warner in 1993 developed the twelve principles of Green Chemistry [2], reported in Figure 1:

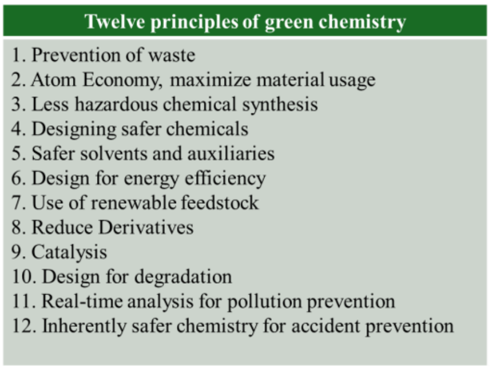

Twelve principles of green chemistry

1. Prevention of waste
2. Atom Economy, maximize material usage
3. Less hazardous chemical synthesis
4. Designing safer chemicals
5. Safer solvents and auxiliaries
6. Design for energy efficiency
7. Use of renewable feedstock
8. Reduce Derivatives
9. Catalysis
10. Design for degradation
11. Real-time analysis for pollution prevention
12. Inherently safer chemistry for accident prevention

Figure 1. The twelve principles of green chemistry [2]

The 12 principles could be seen as design rules to help chemists to achieve the international goal of sustainability. These principles provide the starting point to design process as sustainable as possible from an environmental and economic point of view. In particular, the use of heterogeneous catalysts is of great importance, because they allow to keep the reaction selective for the desired products, lowering the production of unwanted by-products which would result in waste; furthermore, the use of renewable feedstock is of vital importance in a society that currently has a shortage of fossil fuel raw materials, the use of which also has a large impact on the environment. In this work we have focused on both of these principles in order to design processes with low environmental impact.

1.2 Lignocellulosic feedstocks biorefinery

One of the principles of "Green Chemistry" is to use renewable feedstock. Plant-based raw materials (i.e. biomass) appears to have the potential to replace fossil fuels. In fact, biomass is abundant and uniformly distributed on the planet. Consequently, in addition to being a renewable raw material, it allows the creation of energy independence in countries that today have a low production of fossil fuels, allowing them to create new jobs and become self-sufficient, consequently strengthening their economy.

Thus, the concept of biorefinery is introduced: biorefinery was defined by the IEA Bioenergy Task as ‘‘the sustainable processing of biomass into a spectrum of marketable products and energy” [3]. Biorefinery brings together different technologies that can separate biomass resources from its main constituents, which are then subsequently converted into high added value products, chemicals and biofuels [4].

Of all the raw materials of biorefineries, lignocellulosic biomass is the most interesting, due to its high availability and low cost depending on the price of fossil fuels. It can be obtained by cultivation or as a residue; Its cultivation has the advantage of not competing with the cultivation for food, thanks to the fact that it can be produced in dedicated fields that otherwise would not be exploited. It can also be obtained from various wastes, such as straw from agriculture, or wood waste from paper production. Other sources of lignocellulosic biomass are waste and residues, such as straw from agriculture, wood waste from the paper manufacturing industry.

Lignocellulosic biomass is composed of three main components: cellulose, hemicellulose and lignin (Figure 2).

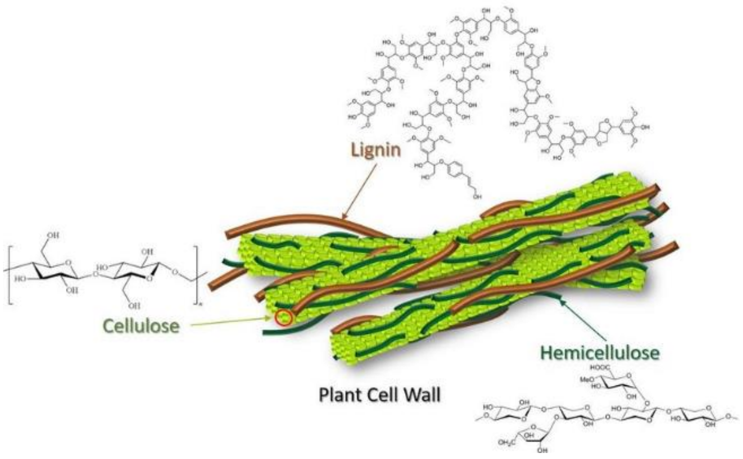

Figure 2. Lignocellulosic biomass composition.

- Cellulose makes up 30-50% of dry lignocellulose. It is made up of several glucose molecules (C6 sugar) joined by a glycosidic bond. Cellulose has a rigid structure due to the bond configuration that joins the hexose groups, making it difficult for them to be hydrolysed by enzymes or acids [5].
- Hemicellulose consists of 20-40% of dry lignocellulose. It consists of a set of sugars with 5 and 6 carbons. Being an amorphous polysaccharide, it is easier to hydrolyse than cellulose.
- Lignin corresponds to the remaining 15-25% of lignocellulose. It is composed of a polymeric structure of phenylpropane units. The "woody" plants are defined in this way precisely because of the high percentage of this component, which makes the structure rigid and resistant acting as a glue [4,6]. It is composed by many methoxylated derivatives of benzene, especially coniferyl, sinapyl and coumaryl alcohols (Figure 3).

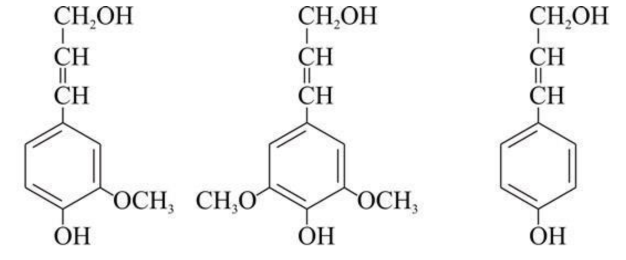
coniferyl alcohol sinapyl alcohol *p*-coumaryl alcohol

Figure 3. Composition of ligninic fraction of lignocellulosic biomass.

1.3 Conversion of biomass

Biomass can be converted into biofuels and chemicals following three main processes, such as, thermochemical, chemical and biochemical processes.

Thermochemical processes

Thermochemical processes are based on the use of high temperatures to convert biomass into electricity, fuels and heat. Thermochemical processes include pyrolysis, gasification, liquefaction and combustion [7-10].

- *Liquefaction* In this process the production of liquids from the biomass is maximised, using low temperatures (250-400 °C) and high pressures (5-20 MPa) in the absence of oxygen and in the presence of catalysts such as metals and carbonates. The products of these reactions are hydrocarbons called heavy oils. They contain few oxygen and have a high calorific value. [11]
- *Pyrolysis* In this process biomass is thermally decomposed at high temperatures in the absence of oxygen. Depending on the process and the final temperature, various products can be obtained through the pyrolysis process: biochar at temperatures around 450 °C, with a slow heating rate; a mixture of light gases similar to syngas at high temperatures around 800 °C, with an increased and high heating rate. At intermediate temperatures the bio-oil is obtained [12].
- *Gasification* In this process biomass is partially oxidized using a gasifying agent, such as oxygen, air and stream at high temperatures (700-900 °C) to produce syngas (H_2, CO, CO_2 and CH_4) [12].

In addition to thermochemical processes, biomass is treated by chemical and biochemical processes. The common factor of these processes is that initially the main fractions of lignocellulosic biomass (i.cellulose, hemicellulose and lignin) are separated; subsequently these are broken down into their simplest components, in order to convert them into chemicals and fuels.

Chemical processes

Among the possible chemical processes, the most important one is the hydrolysis. In particular, strong inorganic acids such as HCl and H_2SO_4 are used to depolymerize the polysaccharides. Generally, the hydrolysis temperature is around 100-160°C [13].

Biochemical processes

Biochemical process is based on fermentation by microorganisms and enzymes, or on anaerobic digestion in the absence of oxygen by bacteria. [14] Chemical process can sometimes be used as a pre-treatment.

1.4 Twelve "Top Value-Added Chemicals”

In biorefineries, the fraction of carbohydrates that is obtained from cellulose and hemicellulose of lignocellulosic biomass is the starting point for the main biochemical products: in order to work as efficiently as possible, it is necessary to start from a limited number of platform molecules, which are bio-based or bio-derived chemicals that could be used as building blocks for the production of interesting products from an industrial point of view. The polysaccharides are in fact hydrolysed to monosaccharides, which are converted into the main platform molecules through fermentation processes. Kamm in 2004 [14] reported the principal chemicals and fuels that can be obtained starting from lignocellulosic biomass. As reported in Figure 4, from hemicellulose it is possible to obtain xylose, which can be converted to furfural, molecule used to produce various chemical compounds. From the hydrolysis of cellulose, glucose is obtained by chemical hydrolysis or by enzymes, as previously reported. Glucose itself can be converted into interesting industrial chemicals as presented in Figure 4.

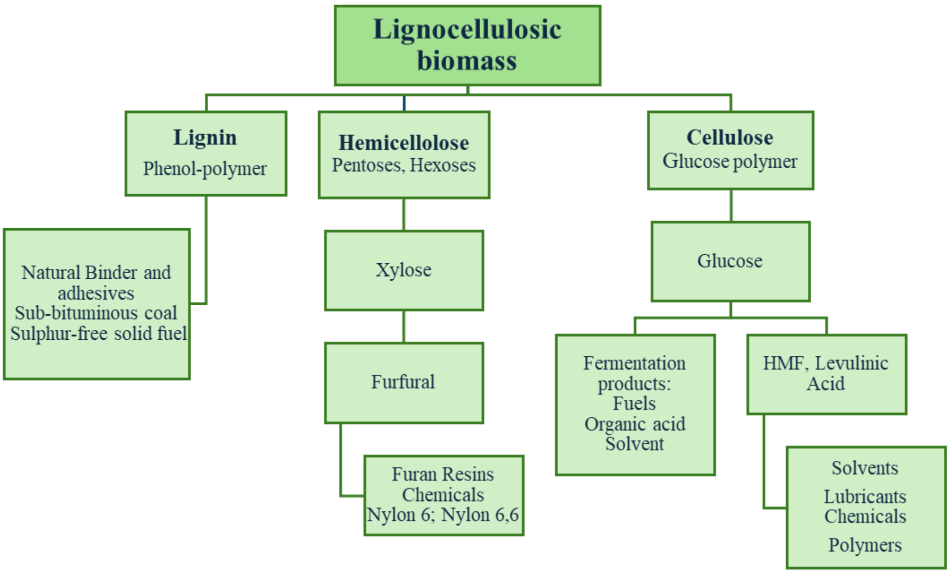

Figure 4. Principal chemicals and fuels obtainable from lignocellulosic biomass [14].

The United States Department of Energy (DOE), in 2004, identified 12 "Top Value-Added Chemicals" obtainable from lignocellulosic biomass (Figure 5). These molecules were identified as they have the potential to be converted into products of high industrial interest, presenting easily transformable functional groups.

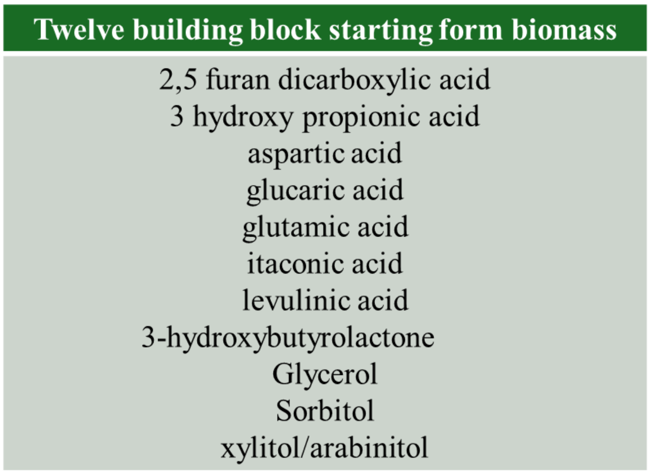

Twelve building block starting form biomass
2,5 furan dicarboxylic acid
3 hydroxy propionic acid
aspartic acid
glucaric acid
glutamic acid
itaconic acid
levulinic acid
3-hydroxybutyrolactone
Glycerol
Sorbitol
xylitol/arabinitol

Figure 5. The twelve top value-added chemicals from lignocellulosic biomass.

In this work we will focus on some of them, on their versatility in the industrial field, where through different processes and reactions it is possible to obtain interesting chemical products. In particular, the attention will go from the development, synthesis and characterization of the catalysts which will then be tested in different target reactions, optimizing the reaction conditions in order to control the selectivity and yield of the desired products.

2. Hydrogenation of levulinic acid and its derivatives

2.1 Introduction

2.1.1 Levulinic Acid (LA)

Among the twelve top value-added chemicals form lignocellulosic biomass, Levulinic acid (LA) and its esters (LE) have always found a particular interest, thanks to their versatility [15]. LA is a water-soluble gamma-keto-carboxylic acid (pKa = 4.59), with a boiling point of 246 °C and a melting point of 37 °C. It can be obtained directly from cellulose with acid-catalysed reactions using homogeneous and heterogeneous catalysts: the first step is the hydrolysis of cellulose to glucose, which is subsequently isomerized to fructose; fructose is then dehydrated to hydroxymethylfurfural (HMF) with the loss of three molecules of water, then the latter is hydrated with a coproduction of LA and formic acid as shown in Figure 6 [16].

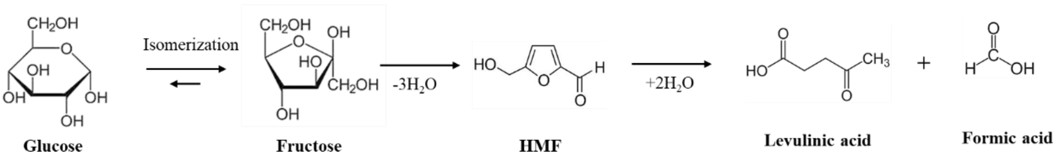

Figure 6. Reaction pathway and mechanism of formation of Levulinic Acid starting from Glucose.

Thanks to the presence of interesting functional groups such as ketones and carboxyl groups, LA and its derivatives can be converted into various interesting and important products following various possible reactive processes, including oxidation, hydrogenation, condensation, etc. (Figure 7) [17-19].

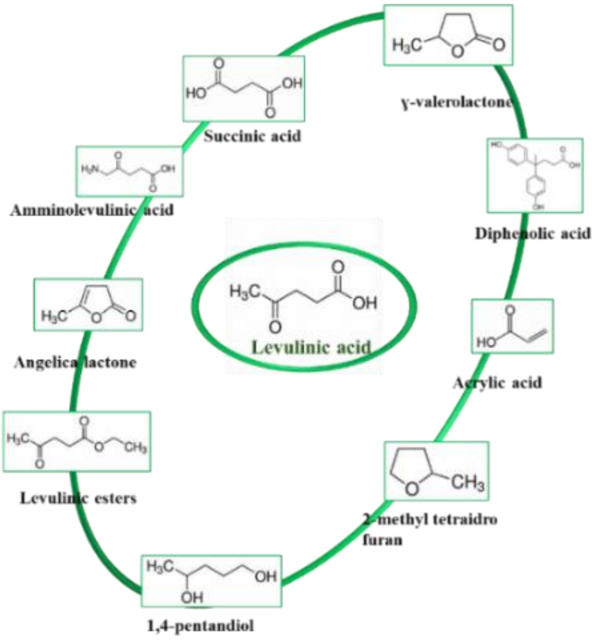

Figure 7. Main products produced from Levulinic Acid.

From the oxidation of levulinic acid it is possible to obtain succinic acid, another molecule of the top 12 value-added chemicals. This reaches an annual value of 400 billion USD per year [20] and finds applications in various industrial sectors, such as the production of surfactants and detergents or foaming agents. Furthermore, Succinic acid is used in the food industry mainly as a flavouring agent and for the production of antibiotics, aminoacids and vitamins [21]. Generally, these molecules are obtained by petrochemical processes, with the hydrogenation of maleic anhydride derived from fossil *n*-butane [22]. The oxidation of levulinic acid can be an interesting alternative to obtain succinic acid starting from biomass, using molecular oxygen as oxidizing agent at temperatures around 200-400 °C and using as heterogeneous catalyst V_2O_5 as oxidizing agent [23] or ruthenium supported nanoparticles at 150 °C and 14 bar of O_2, with a selectivity for succinic acid of 98.6% [24]. Moreover, another route is the esterification of LA yield valuable chemicals, namely the alkyl levulinates, that have potential applications in the flavouring and fragrance industries and as additives for diesel and biodiesel fuels.

Levulinic Acid can be hydrogenated to different products. One of them is methyltetrahydrofuran (MTHF), that is an additive present in gasoline. Moreover, 2-MTHF is an interesting product with different applications: it can be used as electrolyte for lithium rechargeable batteries or as an alternative biofuel.

2.1.2 Ɣ-valerolactone (GVL): an interesting product of Levulinic Acid hydrogenation

One of the most interesting products obtainable from the hydrogenation of levulinic acid is ɣ-valerolactone (GVL). In fact, it is itself an important platform molecule that has many applications in various sectors such as a component in fragrance manufacture, as a food additive, as a bio-based solvent and as a fuel additive. It is particularly interesting thanks to its properties: in fact, it has a high boiling point (207 °C) and a low melting point (-31°C). It is soluble in water and at the same time stable [25], which is very important because it does not react to generate explosive compounds. Being non-toxic and biogredable, GVL finds various applications in the fragrance and food sector [26]; it is also an interesting bio-based solvent thanks to its non-toxicity, biodegradability and because it does not form peroxides at low temperatures [27]. Furthermore, due to its high energy power and low vapor pressure, it is an excellent candidate as biofuel [28].

2.1.3 Levulinic Acid hydrogenation: type of catalyst

2.1.3.1 Levulinic Acid hydrogenation using homogeneous catalysts

Different processes have been proposed and developed to obtain GVL starting from the LA, both with homogeneous and heterogeneous catalysts. In particular, in homogeneous catalysis, phosphine complexes of transition metals resulted particularly active in this reaction: the $[Ru(II)Cl_2(PPh_3)_3]$ complex under optimized batch conditions (180 °C, 12 bar of H_2 24 hours) allows to obtain an almost complete conversion to GVL, with a yield of 99% [29]. Ruthenium catalysts generated in situ were also tested: in particular, Horvath and coworkers, by combining the $Ru(acac)_3$ (acac =acetylacetonate) complex with $PnBu_3$ phosphines in the presence of NH_4PF_6, managed to obtain a quantitative conversion of LA to GVL [30], using however a high pressure of molecular hydrogen (135°C, 100 bar H_2, 8 h reaction). Ir-based complexes also gave interesting results: in particular, chlorinated complexes such as $Ir(COE)_2Cl_2$ (COE=cyclooctene) and tridentate complexes have given interesting results (100°C, 50 bar H_2) in the presence of base [31]; those with electron donor binders such as *t*Bu and *i*Pr reported the best catalytic performance, with GVL yields in the 96-99% range.

Palladium-diphosphine complexes were found to be active in the hydrogenation reaction of LA to GVL: in particular Pd(diphosphine)X_2, where X= Cl, H or Me, showed good results in catalytic terms for the catalytic transfer hydrogenation (CTH) reaction using furfuryl alcohol as H-donor in mild reaction conditions (80°C, 5 bar H_2, 5 hours), with yields above 99% in GVL and TON of 1000 [32].

2.1.3.2 Levulinic Acid hydrogenation using heterogeneous catalysts

From the examples reported above it has been seen that various homogeneous catalysts are active in the hydrogenation reaction of LA to GVL. However, these have the fundamental problem of not being able to be easily reused at the end of a reaction, being difficult to separate from the reaction products as they are in the same physical phase, consequently increasing costs and making the process less sustainable both from an environmental and an economic point of view, considering the waste generated at the end of the reaction. For this reason, the research moved towards heterogeneous catalysts, which are for definition in a different phase from reaction medium and they are generally in solid phase and they can be easily recovered at the end of the reaction are regenerate to be reused. The heterogeneous catalysts used for hydrogenation reactions can be of various types: for example, they can be metal oxides or supported metals.

Among the supported noble metals, Ruthenium has shown very promising results: a 5% wt Ru/C catalyst in water under optimized conditions (temperature 30 °C; H_2 12 bar; 160 min of reaction) gave interesting results with a GVL selectivity of 86.6% and a conversion almost total of LA. Furthermore, the addition of sulphonated acid resins (Amberlyst-70) mixed mechanically with the same Ru-based catalyst, has made it possible to achieve similar results but in milder temperature and pressure conditions (temperature of 70 °C; pressure 5 bar of H_2) [33].

Catalysts based on Ru nanoparticles supported on TiO_2 were up to 3 times more active in the LA hydrogenation reaction compared to Ru/C based catalysts [34]. Catalysts based on bimetallic nanoparticles were also active for the reaction in question: Luo and co-workers [35] have synthesized a Ru-Pd/TiO_2 catalyst by a modified impregnation method using dilute HCl in order to obtain very small and size-controlled nanoparticles. Its catalytic activity in the LA hydrogenation reaction was compared to its monometallic counterpart Ru/TiO_2: the bimetallic catalyst gives a complete conversion of LA after 30 min of reaction, unlike the monometallic one which has a complete conversion after 40 min. Furthermore, at reaction times greater than

2 hours, using the bimetallic catalyst the selectivity towards the formation of GVL remains constant, unlike the monometallic one where the selectivity decreases as the time increases. This may be due to the presence of Pd which tends to move the Ruthenium sites away during the reaction.

Palladium is a particularly active catalyst for hydrogenation reactions. Pd nanoparticles encapsulated in metal-organic framework (MOF) UiO-66-NH_2 were characterized and tested in the reaction in question. The catalyst showed excellent GVL productivity (1741.1 mmol g^{-1} h^{-1}) in the liquid phase (T=140°C, PH_2= 2Mega Pascal). [36]

Pd nanoparticles deposited on multi-walled carbon nanotubes (CNT) are synthesized by liquid impregnation method and tested in the LA hydrogenation reaction. They showed excellent results, with GVL yields from 53.6% to 57.6% in mild conditions in the liquid phase (200°C, 60 bar H_2, 6h reaction). [37]

In order to make a process as sustainable as possible, it is necessary to take into consideration different aspects, in order to make the process economical, sustainable and with a low environmental impact. The use of heterogeneous catalysts is certainly to be preferred, since they can be easily recovered and reused and reducing costs at an industrial level. Furthermore, the use of noble metals is not in long term sustainable both from an economic and environmental point of view, since these are rare, difficult to find and with high economic and environmental cost.

2.1.4 Catalytic Transfer Hydrogenation: an interesting alternative to molecular hydrogen reduction

In recent years, research has moved towards the use of easily available and low-cost materials as catalysts, which however at the same time gave promising results in terms of GVL yields [38]. Furthermore, research has moved towards alternative processes to the use of pressurized molecular hydrogen as a reducing agent: this, in fact, leads to numerous problems in terms of safety and maintenance of the plant.

For these reasons, in this work we focused on Catalytic Transfer Hydrogenation (CTH) via the Meerwein-Ponndorf-Verley (MPV) mechanism. In this process molecular hydrogen is not used, but small molecules, generally alcohols, which function as reducing agents by donating hydrogen (H-donor) to the substrate of interest, in this case LA [39-45].

For this mechanism the design and presence of a catalyst with amphoteric properties is required: indeed, the presence of Lewis acid and basic sites and resistance to high temperatures are essential. Dumesic at al. [46] reported how zirconium oxide, also called zirconia, is an excellent material for this mechanism, thanks to its resistance to high temperatures and the high presence of Lewis acid and basic sites, so to activate at the same time both the carbonylic group and the alcohol.

The generally accepted mechanism is the following: the first step, after the adsorption of the alcohol and the substrate on the desired sites of the catalyst, is the formation of a six-membered intermediate on the catalyst surface; the second step is the hydrogenation: two hydrogens are transferred from the alcohol to the substrate: both the one in alpha, proper to the carbon in alpha, and the hydrogen of the -OH group, thus oxidizing the alcohol to ketone. The reduction mechanism of Cyclohexanone with 2-PrOH over ZrO_2 Catalyst is reported in Figure 8.

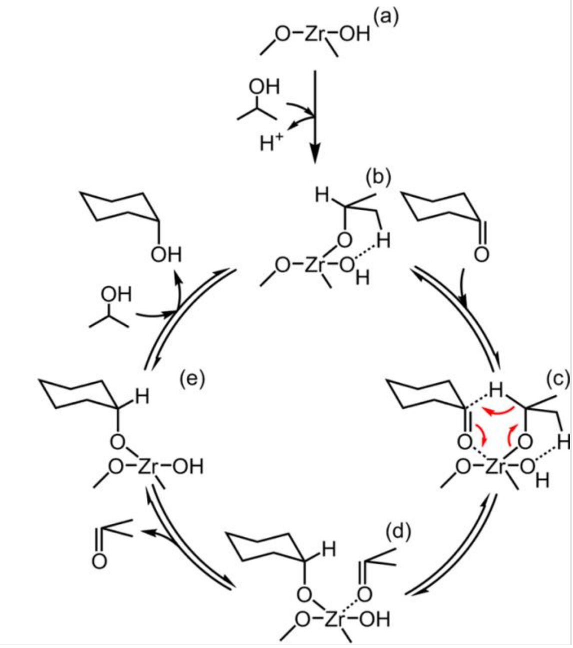

Figure 8. Plausible Reaction Pathway for MPV Reduction of Cyclohexanone with 2-PrOH over ZrO_2 Catalyst (mixture of monoclinic and tetragonal) via Acid−Base Concerted Mechanis [47]

Alcohols are generally used as H-donors since they are very efficient in these types of reactions and, moreover, they can be obtained through fermentation processes, thus resulting bioalcohols, for example bio-ethanol. With the tearing of the hydride, a carbocation is formed; the higher the number of carbonyl groups to which the positively charged carbon of the carbocation is bonded, the more stable it is. Consequently, a secondary alcohol such as isopropanol is more active as H-donor than a primary alcohol, such as methanol or ethanol, because the carbocation that is formed is more stable, while tertiary alcohols are not active in these reactions since they have no alpha hydrogens. Isopropanol is one of the most common alcohols for CTH reactions due to its low cost, high availability and its high reactivity and the possibility to produce a useful byproduct as acetone [48]. Primary alcohols, on the other hand, are not very reactive and one of the main disadvantages is the loss of a hydride and they can oxidize to aldehydes which are often poisonous, such as the case of formaldehyde for methanol and acetaldehyde for ethanol.

The conversion of LA or LEs to GVL using ZrO_2 as one of the most promising heterogeneous catalysts and alcohols such as H-donor in the liquid phase and in batch processes allows to obtain excellent GVL yield (91-96%). However, long time of reaction (around 8-10 h) are necessary to have a high conversion of LA in batch reactor [49,50]. Moreover, the autogenous pressure of the alcohol generated by the high temperatures is high. Since 2019, continuous gas phase processes have been proposed in fixed bed reactors in order to improve productivity [51,52]. One of the main advantages of these processes is that they allow to act in a large range of temperatures (up to 500 °C) at atmospheric pressure, thus resulting much safer.

In particular, in the work of our research group, Vasquez et al. [51] studied the CTH mechanism in the gas phase using tetragonal zirconia with a high surface area (120 m^2/g) and ethanol as H-donor as catalyst. In particular, they started from methyl levulinate (ML) and ethyl levulinate (EL) instead of LA, since the ethers have a lower boiling point of acid, thus allowing them to act even at lower temperatures. In this process it was possible to achieve a total conversion of the ML and a maximum yield of GVL around 70% under optimized conditions (P=atm, T=250°C, contact time= 1s).

In the same work a reaction mechanism for the reduction of LA in the gas phase on zirconia was proposed (illustrated in Figure 9).

The proposed reaction mechanism using ZrO_2, is the following one. In the first step, the LA (or LE), rapidly cycles to the angelica lactones (α/β AL). The ALs, in turn, can undergo CTH with ethanol leading to the formation of the desired product, GVL, with the formation of acetaldehyde due to the transformation of ethanol. In turn, acidic sites of the catalyst can favor the ring-opening of the GVL and the subsequent dehydration, with the formation of ethyl pentanoate (EL). The parallel reaction to the formation of GVL from ALs is the formation of Ethyl GVL, which occurs by hydroxy-ethylation of the formed acetaldehyde and by dehydration and reduction of the C-OH group. Ethyl levulinate (EL) can be formed from AL, which formation favors the deactivation of the catalyst, leading to subsequent transesterification reactions and so to the formation of heavy carbonaceous products which deposit on the Lewis acid sites and therefore deactivating the catalyst.

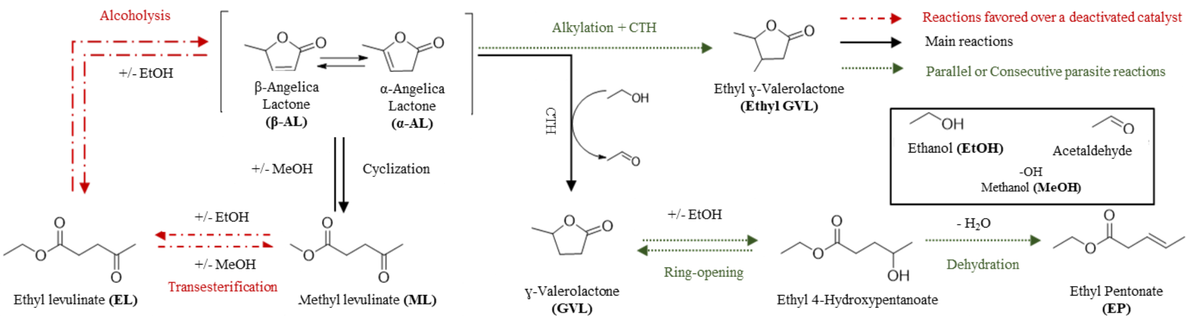

Figure 9. Mechanism of H-transfer hydrogenation of methyl levulinate.

2.1.4 Zirconia

Zirconia, or zirconium oxide (ZrO_2), is a polymorphic ceramic material (Figure 10). It can be used in the field of heterogeneous catalysis both as a catalyst itself and as a support [53]. It exists in several allotropic forms. From 0 to 1180 °C it appears in monoclinic (*m*-ZrO_2) form (P21 /c symmetry). This structure consists of heptacoordinated Zr and tri- and tetracoordinated oxygens; at higher temperatures up to 2370 °C, zirconium oxide occurs in tetragonal (*t*-ZrO_2) form (P42 symmetry / nmc), where the zirconium atoms are eight-coordinated and the oxygens tetra-coordinated. At temperatures above 2370 °C the stable phase is the cubic (*c*-ZrO_2) one, called fluorite (Fm$\bar{3}$m symmetry), where the zirconium atoms are eight-coordinated and the oxygens tetra-coordinated. The melting temperature of zirconia is 2680 °C [54,55].

During heating, the transformation from *m*-ZrO_2 to *t*-ZrO_2 occurs with a volumetric contraction of about 5%, vice versa during cooling and the transition from *t*-ZrO_2 to *m*-ZrO_2. To stabilize the tetragonal phase at room temperature there are two ways: either by doping with bi and trivalent ions such as Mg^{2+}, Ca^{2+}, and Y^{3+} [56,57], or stabilizing it in nanostructures with a diameter of less than 50 nm [58].

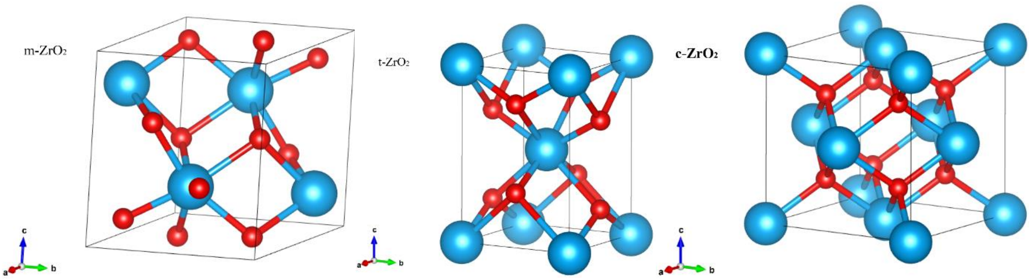

Figure 10. The three crystalline phases of zirconia, form left: monoclinic, tetragonal and cubic.

As previously mentioned, zirconia has innumerable uses in the catalytic field. It can in fact be used both as a catalyst and as a support. In this work we will examine different reactions starting from biomass in which zirconia can be used as a catalyst. These will be hydrogenation and oxidation reactions.

In this work we have focused on two phases of zirconia, *m*-ZrO_2 and *t*-ZrO_2, in order to compare their catalytic properties. In particular, for an atomistic study of these two structures, it is important to know the exposure of the surface atoms, i.e. those with reactivity in catalytic reactions. In particular, by cutting the bulk zirconia structure, the thermodynamically most stable exposed surface area for *m*-ZrO_2 and *t*-ZrO_2 is $(1\bar{1}1)$ and (101) respectively, as reposted by Christensen and Carter Christensen, A.,[54] while the most stable termination is the O-terminated one [59].

In addition to the field of catalysis, zirconia is mainly used to produce ceramics [60]. Furthermore, thanks to its high ionic conductivity (oxygen ions can move in the crystalline structure) it finds application in fuel cells and, thanks also due to its low electronic conductivity, it can be used in the field of electro-ceramics. Zirconia is also used in the biomedical field in nanoparticle form. In this structure, in fact, there is an increase in the mechanical and optical properties, and greater resistance to low temperatures, excellent characteristics for biomedical materials in order to make them resistant and durable.

2.1.5 Zirconia: support for metal nanoparticles

Zirconia can also be used as a carrier for metal nanoparticles. In particular, nanoparticles are particles with dimensions ranging from 1 to 100 nm [61]. Precisely thanks to their size, nanoparticles have properties that make them unique with respect to their bulk form which make them particularly interesting in various fields: an example in the field of polymers, where the presence of nanoparticles in composite materials with a polymeric matrix increases their temperature of glass transition, making them more resistant and with better mechanical performance; in the biomedical field, thanks also to their biocompatibility, gold nanoparticles are used to detect the presence of cancer cells by acting as carriers of antibodies that bind to them, highlighting them [62].

Nanoparticles, thanks to their high surface area and the under-coordination of the reactive sites, are particularly interesting materials in the catalytic field. In fact, the sub-coordination of the atoms in nanoparticle materials makes elements reactive, such as gold, silver, copper, which in bulk form are inactive, since they are part of group VIII, in which in bulk form the d-band is complete. Surface atoms in nanoparticle structures, on the other hand, are undercoordinated, and consequently much more reactive even in mild conditions [63,64].

In order to make the nanoparticles catalysts of a heterogeneous type, it is necessary to deposit them on a support with enhanced metal-support interaction, so that the catalyst, being in the solid phase and stable and therefore be easily separated and reused at the end of the reaction.

The main characteristics that a support must have are: high surface area, in order to disperse the nanoparticles as much as possible and not cause them to agglomerate; have strong interactions with the nanoparticles, so that there are no leaching phenomena during the reaction; be stable.

Zirconia, being extremely stable and resistant to high temperatures, is an excellent candidate to be used as a support. In fact, it is possible to obtain mono and bimetallic catalysts with nanoparticles of gold, palladium, platinum, etc.

2.1.6 Synthesis of supported nanoparticles

There are various methods for synthesizing supported nanoparticle-based catalysts. These methods profoundly affect the final structure of the catalyst, in particular the size of the nanoparticles and their degree of dispersion, thus affecting their reactivity. The size of the nanoparticles in fact significantly influences their reactivity: smaller nanoparticles have a larger exposed surface area, and consequently a greater number of available catalytic sites. Since nanoparticles are thermodynamically unstable, every small variation in a synthetic method greatly affects their characteristics and properties, leading to a different activity and selectivity. The main methods used are listed below.

Imprenation method (IMP)

The impregnation method is one of the most used as it is very simple and easily controlled. In particular, the impregnation can be classic (IMP) or the incipient wetness impregnation (IW-IMP) type.

In the classic IMP method, we start from one (or more for bimetallic catalysts) chlorinated precursors of the metals of interest which are dissolved in distilled water. To this solution is added the support at room temperature and keeping the system under stirring; the water is subsequently evaporated, obtaining a paste. Finally, the obtained catalyst is dried and calcined.

To reduce metals in nanoparticulate form to the metallic state, the catalyst is treated with H_2. The experimental procedure is summarized in Figure 11.

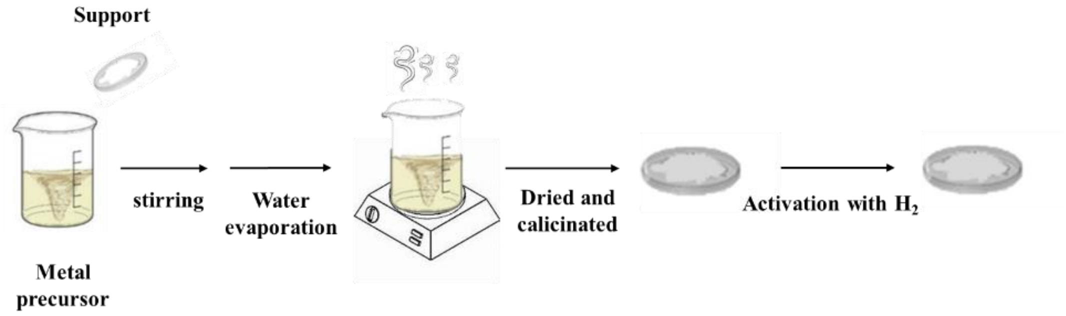

Figure 11. Metallic nanoparticles synthesis via impregnation method.

In the IW-IMP, the precursor is dissolved in deionized water: the amount of water used for this step is chosen according to the pore volume of the support. The obtained solution is added to a beaker where the support has been previously added, all while keeping the system under stirring and proceeding by adding the solution slowly, in about 20 minutes, at room temperature. Finally drying and heat treatment are performed of the obtained catalyst under the desired gas (air, oxygen or hydrogen). Also in this case it is necessary to proceed with the treatment with molecular hydrogen to activate the catalyst and also to remove the chlorine atoms which would favor the sintering of the nanoparticles [65].

Deposition-Precipitation method (DP)

The DP method consists in the deposition of a hydroxide or hydrated oxide of a metal on a support using the precipitation technique. This is done by making the precursor of the metal insoluble, acting on the pH by going to a value above the Isoelectric Point (IEP) by adding a base. The procedure involves preparing a beaker containing a solution of the support and the precursor; one proceeds successively by slowly adding the base, increasing the pH, until the metal hydroxide precipitates. Finally, the catalyst is filtred, dryed and washed, and than it is activated before being used using a heat treatment protocol. Figure 12 shows the general experimental procedure.

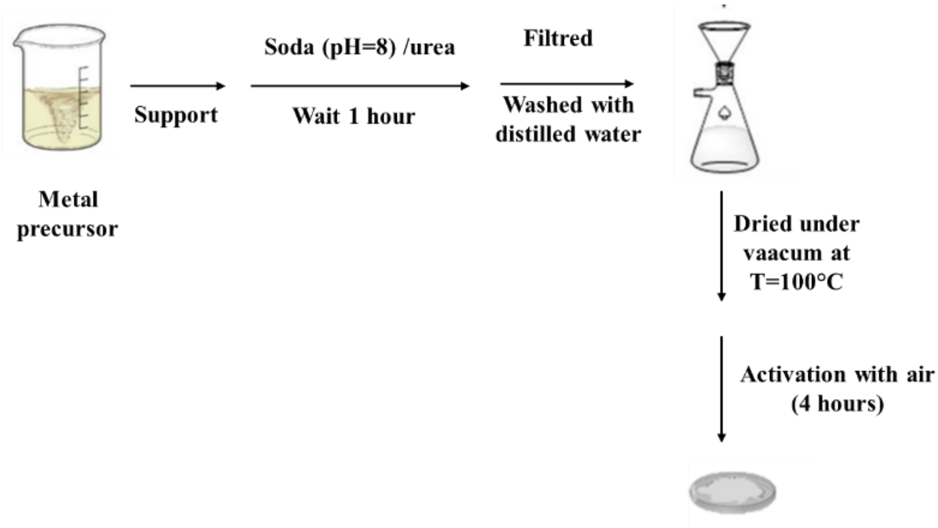

Figure 12. Metallic nanoparticles synthesis via deposition-precipitation method.

Sol-immobilization technique (SOL-IM)

In the SOL-IM technique, first proposed by Prati and Co. [66] in 1999, one starts by preparing the metal nanoparticles in the form of a solution (sol) and subsequently these are immobilized by adding the support, where they are deposited.

Nanoparticles are thermodynamically unstable [67]: this means that under normal conditions they tend to agglomerate, forming increasingly larger nanoparticles. In order not to sinter the nanoparticles in the sol phase, it is necessary to keep them separate: to do this, a stabilizing agent is used, which takes care of decreasing the interactions between the nanoparticles. The stabilizing agent can be mainly of three types: steric, electrostatic or steric-electrostatic. In steric stabilization, the stabilizing agent consists of large molecules that bind to the nanoparticles: precisely because of their volume, they tend to keep them separate; in electrostatic stabilization, anions and cations are present in solution which avoid the interactions between the nanoparticles forming a double electronic layer; however, this technique has the disadvantage that by adding an electrolyte (such as NaCl), this can lead to agglomeration of the nanoparticles [67]. Finally there is electrostatic-steric stabilization, where the two effects are combined; examples of the latter type of stabilizers is polyvinyl alcohol (PVA): part of it in fact adsorbs on the surface of the nanoparticles, separating them sterically; another part dissolves in solution, creating a second protective layer [68].

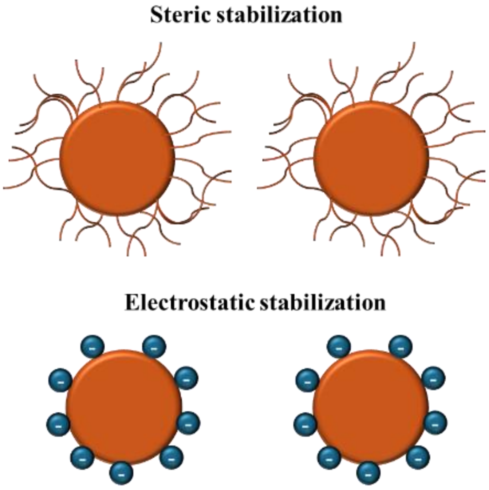

Figure 13. Nanoparticles stabilization: steric and electrostatic.

The procedure consists in preparing an aqueous solution of the metal precursor. It is important that the solution is very diluted, in order to avoid that the nanoparticles, once formed, are in strong contact with each other, a factor which would favor aggregation. After dissolving the metal precursor in water, an aqueous solution of stabilizing agent is added; after three minutes a reducing agent is added, such as $NaBH_4$. Using a strong reducing agent, allows for an immediate reduction of the metal nanoparticles, thus favoring the formation of small-sized metallic nanoparticles, around few nanometers (2-5 nm). The successful formation of the nanoparticles can be seen from the immediate color change of the solution, which is different for each specific metals: the nanoparticles, due to their small size, undergo the phenomenon of plasmon resonance, thus absorbing in the UV-Vis region. Subsequently, after about another 30 minutes, the support is added, which will immobilize and stabilize the nanoparticles into the support. It is necessary to acidify the aqueous solution containing the nanoparticles and the support at a pH lower than the isoelectric point of the support. In this way it will favor the interactions between the nanoparticles and the support. Subsequently the necessary time is needed until all the nanoparticles have been deposited on the support. This can be seen from the fact that if the aqueous part, in the catalyst filtering, is colorless, it means that all the nanoparticles have been deposited onto the surface of the support. The time required for the deposition to take place depends on the type of support, due to its surface area, the interactions it makes with the nanoparticles, etc. Once the nanoparticles have been deposited, the catalyst is filtered and washed with plenty of water to remove all unwanted synthesis waste. Finally, the catalyst is first dried overnight in air and then in an oven to remove the remaining physisorbed water. The procedure is reported in Figure 14.

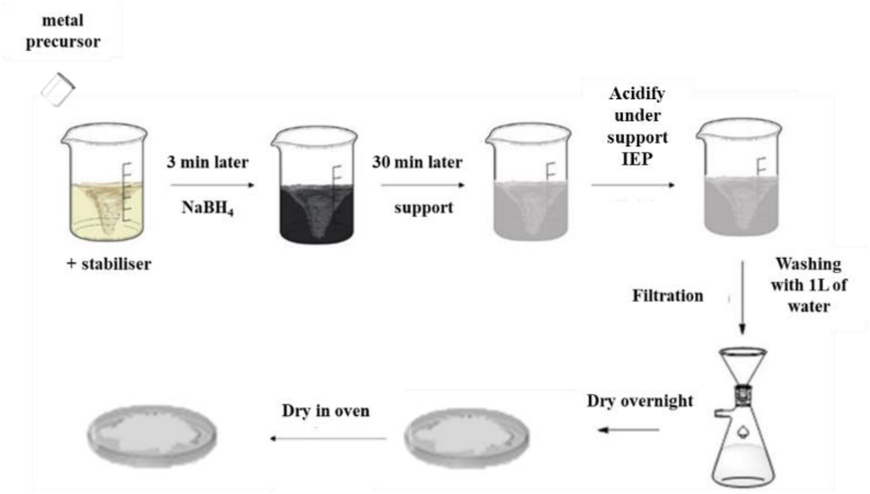

Figure 14. Colloidal metallic supported nanoparticles synthesis via sol-immobilization method

2.2. Scope

The aim of this work is to study the hydrogenation reaction by CTH mechanism of LA derivatives in a continuous gas phase plant. In particular, in the first part we focus on the reaction to obtain GVL, a very interesting product on an industrial level. For this part of the work, we focused on the synthesis and characterization of *t*-ZrO_2 and *m*-ZrO_2, then testing them under the same reaction conditions in order to compare their catalytic activity. Several parameters were varied, such as the temperature, the type of H-donor alcohol, the alcohol/ reagent ratio, in order to optimize the catalytic process.

In order to better understand the reasons for the different catalytic activity for the two crystalline phases, NMR and computational studies were carried out to better explain the deactivation phenomena.

The reaction was subsequently studied with the aim of obtaining Ethyl pentanoates as the main products. For this reaction, zirconia-based catalysts with high surface areas were characterized and tested for the reaction under examination.

2.3 Experimental part

2.3.1 Synthesis of zirconia catalysts

Different types of zirconia catalysts have been synthesized as the desired heterogeneous catalysts.

In order to better understand the effect of the crystalline phases of zirconia in CTH of levulinic esters (LE), *m*-ZrO_2 and *t*-ZrO_2 phases have been synthesized, with the hypothesis that the different structure can affect catalytic performance in terms of selectivity/yield to the desired products, stability and therefore long-term performance and possible deactivation phenomena.

2.3.1.1 Synthesis of high surface tetragonal zirconia

t-ZrO_2 was prepared by precipitation methodology (Figure 15), following the procedure of Chuah et al. [53]. A solution of $ZrO(NO_3)_2 \cdot 2H_2O$ 0.3 M was added dropwise to a stirred solution of NH_4OH 5M at room temperature. Afterwards, the solution was digested at 100 °C for 24 or 48 h under reflux system. The pH of the solution was adjusted to 9 during the digestion by the addition of NH_4OH. The precipitate was separated by filtration and washed with NH_4OH 5 M. After the filtration step, the sample was dried at 100 °C overnight and then calcined in air at 500 °C for 12 h at 5 °C/min.

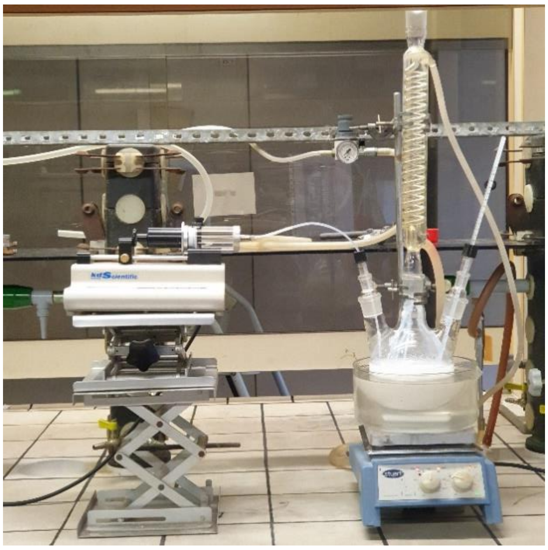

Figure 15. Set up for the synthesis of high area tetragonal zirconia.

2.3.1.2 Synthesis of monoclinic zirconia

m-ZrO_2 catalyst was prepared by hydrothermal synthesis. A solution was prepared by adding 3.38 g of $ZrO(NO_3)_2 \cdot 2H_2O$ to 20 mL of distilled water. Afterwards, 6.06 g of urea were added, and the solution was then transferred to an autoclave with a Teflon inlet. The autoclave was placed inside a furnace with a temperature of 140 °C for 20 h. Afterwards, the precipitate was firstly centrifuged with ethanol, and then with distilled water. The sample was then dried at 100 °C overnight and then calcined in air at 450 °C for 3 h with a heating rate of 5 °C/min. The synthesis, having yields around 1 gram, was repeated countless times to have a sufficient quantity for subsequent tests.

2.3.1.3 Synthesis of supported nanoparticles on zirconia: sol-immobilization technique

Supported metal catalysts were prepared by sol immobilization technique. In particular, different type of metal and support have been used, and both mono and bimetallic catalysts have been prepared. The results of the catalytic test using this catalyst are reported in “Future work”.

Synthesis of Palladium supported nanoparticles

To obtain 1 g of catalyst with 1%wt of metal loading, the metal precursor solution was prepared: 0.0312 g of Potassium tetrachloropalladate(II) were dissolved in 385 mL of distilled water and the solution was stirred at room temperature. After that, 1.188 mL of a PVA aqueous solution previously prepared (0.1010g in 10 mL of distilled water) was added, keeping the solution stirred (PVA: metal = 1.2:1 weight ratio). After three minutes, a fresh aqueous solution of the reducing agent $NaBH_4$ was added ($NaBH_4$: metal = 5:1 molar ratio). The change of the colour of the solution indicates the correct formation of the colloidal metal nanoparticles; in particular, for gold the solution changes from yellow to red; for palladium, the solution changes from yellowish to grey. The change of color from yellow to dark read indicated the correct formation of gold colloidal nanoparticles. After 30 minutes, the support was added (0.99 g) and the solution was acidified with sulphuric acid under the isoelectric point of the support (pH=5) to maximize the interaction between the nanoparticles and the support. The solution was left under stirring overnight, then it was filtered and the catalyst was washed with distilled water (about 1 L) in order to remove the impurities, until the washing water had reached neutral pH. The catalyst was left to dry overnight at room temperature and subsequently dried in an oven for 4 hours at 150 ° C. The procedure is reported in Figure 16.

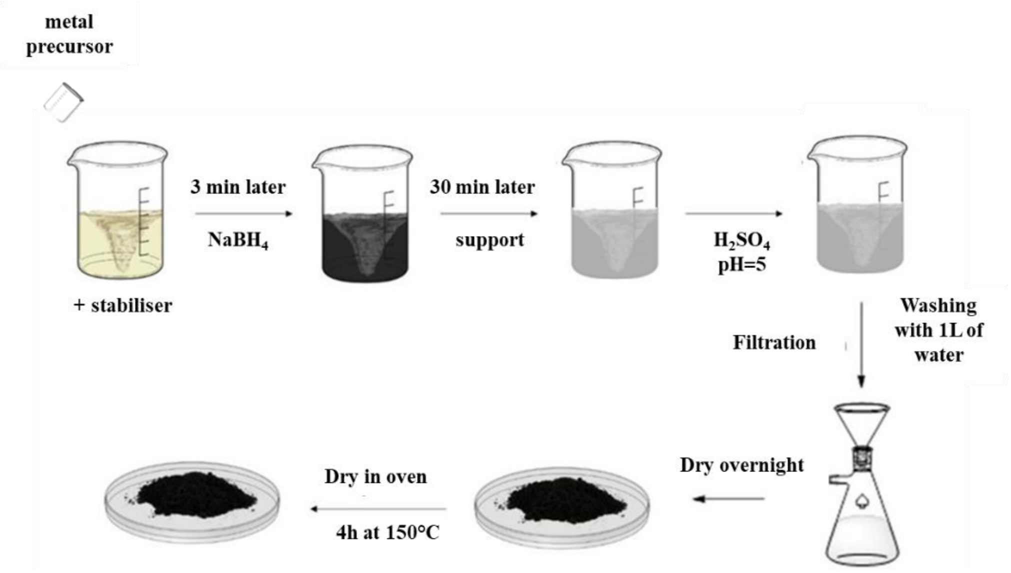

Figure 16. Procedure of synthesis of Pd supported NPs using sol-immobilization technique.

2.3.2 Characterization of catalysts

We proceeded with characterizations of the synthesized catalysts. The purpose of this is to confirm that the synthesis has been carried out correctly, resulting in the desired materials. In particular, for zirconias it is important to evaluate the surface area, the degree of crystallinity and the crystalline phase, the quantity of acidic and basic sites, all fundamental factors for the CTH reaction of methyl levulinate (ML) for which they will be tested. We then proceeded by carrying out XRD analysis to evaluate the crystallinity, a BET analysis to evaluate the specific surface area; TPD analysis to evaluate the quantity and strength of acidic and basic sites.

X-ray powder diffraction (XRD) patterns were collected with a Ni-filtered Cu Kα radiation (λ = 1.54178 Å) on a Philips X'Pert vertical diffractometer equipped with a pulse height analyser and a secondary curved graphite-crystal monochromator (Figure 17). Analysis were performed with acquisition time of 15 s per step with 0.05°2θ distance, in 5 - 80° 2θ range.

Figure 17. Philips X'Pert vertical diffractometer instrument for XRD analysis

Diffraction (XRD) X-ray diffraction is a characterization technique that allows to study crystalline solids. In particular, it allows to give information on their crystalline structure, exploiting X-rays and the phenomenon of diffusion: when X-rays hit a sample, the electrons begin to vibrate spreading the radiation in different directions. When the sum of the scattered radiations is in phase there is a constructive interference, from which a reflection pattern is obtained which represents the atoms present in the corresponding lattice planes, with the corresponding peaks called Bragg peaks; these peaks depend on the incision angle and the crystal lattice. For this phenomenon to occur, Bragg's law, shown below, must be respected:

$$n\,\lambda = 2\,d\,sin\theta$$

Where: n = integer (diffraction order); λ = wavelength of the x-rays; d = distance between adjacent planes in the lattice; θ = incident angle of the x-ray beam.

BET specific surface area of the catalysts was determined by N_2 absorption–desorption at -196 °C using a Sorpty 1750 Fison instrument (Figure 18).

Figure 18. Instrument Sorpty 1750 for BET surface analysis

This technique is based on the physisorption of an inert gas, in this case nitrogen. First of all, 0.1 g of sample was outgassed at 150 °C, to remove any physiosorbed substance. Subsequently, it was inserted in a liquid nitrogen bath and N_2 was pulsed. From the volume of adsorbed N_2 it was possible to calculate the surface area of the sample, using the Bunauer-Eller-Teller (BET) model. According to this model, the adsorption is multilayered and uniform and the exothermicity of the adsorption of the second layer is lower than the first and equal to the liquefaction energy. In this way it is possible to determine the monolayer adsorption, and consequently the surface area.

NH_3-CO_2-temperature-programmed desorption (TPD) analysis were performed to calculate the total acidity and basicity of catalysts. In particular, Acid and Basic Lewis sites are fundamental for CTH reactions, but with TPD analysis is possible to calculate the total amount of acid and basic sites, as Lewis and Brönsted Acid sites. The measurements were collected with a Autochem II TPD/R/O 2920 automated system for analysing the acid/base properties of catalysts (Figure 19). Fresh catalyst was pre-treated to remove water and CO_2 adsorbed with a 30 mL/min flow of 10 vol.% O_2 in He at 500 °C for 1 hour with a ramp of 10 °C/min. The catalyst was then exposed to NH_3 (or CO_2) for study acid sites (or basic sites) for 1 h with a flow of 30 mL/min of 10 vol.% of NH_3 or CO_2 in He. Physisorbed molecules were removed by flushing with He (30 mL/min of He) for 10 min prior to analysis. Finally, the temperature-programmed desorption was performed following the desorption with TCD detector to the temperature of 450°C with a ramp of 10 °C/min with a flow of He (30 mL/min).

Figure 19. Autochem II- Micrometrics. Chemisorption analyzer

In Situ Diffuse Reflectance Infrared Fourier Transform Spectroscopy (DRIFT) analysis was performed using a Bruker Vertex 70 instrument equipped with a Pike DiffusIR cell attachment. Spectra were recorded using an MCT detector after 128 scans and with a 4 cm^{-1} resolution in the region of 4000-450 cm^{-1}. The analysis was carried out by loading a zirconia sample into the cell and pre-treating it at 400°C with a 10 mL/min flow of helium for 60 min, in order to remove possible adsorbates from the surface. Subsequently we proceeded by acquiring the background spectrum using KBr and carrying out the measurement every 50°C in a temperature range from 50 to 400°C. We then proceeded by adsorbing 2 μL of dimethyl pyridine (DMP) at a temperature of 50°C and acquiring the IR spectrum every minute. To desorb the DMP, the sample was heated up to 400°C with a ramp of 5°C/min; the spectrum was acquired in the temperature range from 50 to 400°C. This analysis was carried out to distinguish between the Lewis and Bronsted acid sites, which is not possible to do by the TPD analysis, which highlights the sum of the acid sites.

2.3.3 Gas phase hydrogenation

The CTH of ML was performed in a continuous gas phase fixed bed reactor.

The reactor consists of the following parts (see Figure 20).

-*Injection system*. The reaction mixture composed of alcohol/levulinic ester (molar ratio 10:1 under optimized conditions, flow 0.5 mL/h in a N_2 stream) is injected by a syringe pump (KDScientific Legacy Syringe-infusion Pump) into a line preheated to 230 °C in order to have all the reactants in the gaseous state. An inlet with N_2 also arrives at this line, which acts as a carrier gas.

-*Reactor*. The line that transports the reactive mixture and the carrier is connected to a glass tubular reactor (length 450 mm, inner diameter 19 mm), in which 1 cm^3 of catalyst over a quartz wool pelletized at 30-60 meshes. The reactor is positioned inside an oven and there are two electrical resistances to regulate the inlet and outlet temperature.

-*Accumulation section*. At the end of the reactor a glass junction is connected which branches off in a line leading to the vent and a bubbler with acetonitrile immersed in an ice bath. The latter makes it possible to collect the post-reaction condensable products which will then be analysed by GC off-line. The vented line, on the other hand, carries the non-condensable products and has a sampling point for the gaseous phase which can be analysed by GC-MS. Each accumulation of the condensable phase is taken and replaced every 50-60 min.

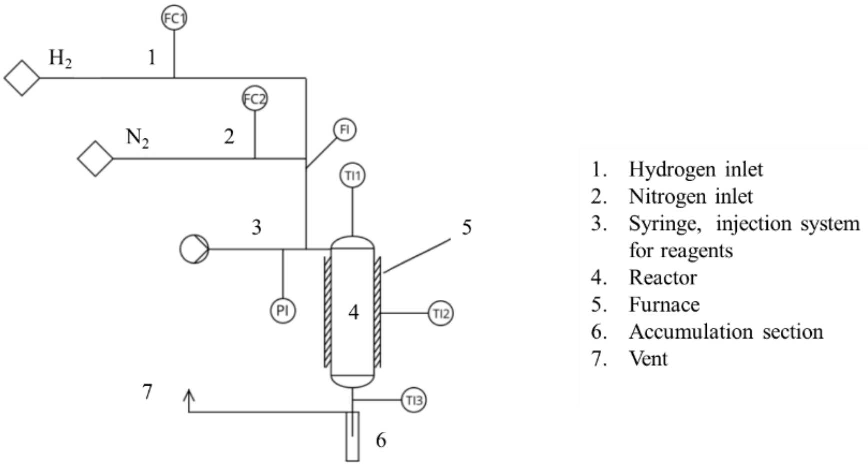

Figure 20. Plant for H-transfer methyl levulinate reduction to GVL.

2.3.4 Analysis of post reactions

The reaction products obtained were analysed by gas chromatography off-line.

Analysis of condensable products

The condensable products recovered from the trap contained in the ice bath were identified by qualitative analysis using a GC-MS, a gas chromatograph to which a mass spectrometer is connected in series. This tool has in fact made it possible to identify known products and also possible unknown by-products. The gas chromatograph column is a HP-5 made up of 95% dimethylsiloxane and 5% phenyl; the carrier gas is helium, the injector is thermostated at 250

°C with injection (0.5 μL) in split mode (50:1). The programmed temperature is shown in Figure 21.

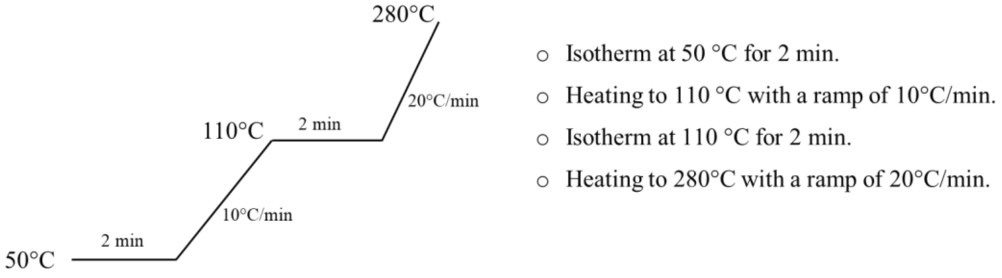

- Isotherm at 50 °C for 2 min.
- Heating to 110 °C with a ramp of 10°C/min.
- Isotherm at 110 °C for 2 min.
- Heating to 280°C with a ramp of 20°C/min.

Figure 21. Programmed temperature of GC-MS analysis.

The mass spectrometer is an inert Agilent Technologies 5793: the mass spectra of the GC separated products are obtained, which, with their respective fragmentations, are compared with the data reported in the database of the National Institute of Standards and Technologies in order to arrive at to product identification.

Once all products have been identified, the post reaction solution is run to another GC in order to perform a quantitative analysis. For each run, 0.5 μL is injected through a glass column.

The gas chromatograph used is the GC2010-Pro Shimadzu. The column is a cross-linked HP-5 column (5 % Phenyl- 95% methylsiloxane; Dimensions: 30 m x 0.32 mm x 0.25 μm). The injector is thermostatically controlled at 280°C and operates in 30:1 split mode. The carrier gas is nitrogen, sent from a capillary column with a flow rate of 1.20 mL/min. the instrument also features a Flame Ionization Detector, FID, which uses hydrogen as fuel and air as comburent and is maintained at a temperature of 280°C. Injection of the reaction mix is the same as for GC-MS, injecting 0.5 μL with a glass syringe. The analysis temperature schedule is the same as for GC-MS.

To calculate the obtained moles of each compound, an internal standard was used: for each accumulation taken, 20 μL of *n*-octane were added approximately every 50 min and subsequently the solution was brought up to volume in a 25 mL flask. In this way, knowing the response factor $F_{product}$ of the product in question, the moles were calculated according to the following equation:

$$\frac{A_{product}}{A_{octane}} = F_{product} * \frac{mol_{product}}{mol_{octane}}$$

Where *A* indicates the area under the peak of the product and the standard (octane) respectively, *mol* indicates the number of moles of the product and the octane.

$$X_{reactant} = \frac{\mathrm{mol}_{reactant}^{in} - mol_{in}^{out}}{\mathrm{mol}_{reactant}^{in}} * 100$$

$$\mathrm{Y}_{product} = \frac{\mathrm{mol}_{product}^{out}}{\mathrm{mol}_{reactant}^{in}} * 100$$

In addition, carbon balance based on alkyl levulinate was considered as follows:

$$\frac{Y}{C} = \frac{\Sigma\text{products yield}}{\text{Reactant conversion}} *100$$

Analysis of incondensable products

The incondensable products were periodically analysed at different times of the reaction, in order to understand if there was the formation of light-products in that phase of the reaction, which could indicate, for example, large shortages in the carbon balance. The incondensable products were qualitatively analysed by GC-MS. To carry out the sampling, a glass syringe with a flow rate of 20 µL equipped with a gas tank was used. The non-condensable phase is taken from a septum present in the line that leads to the vent, immediately after the accumulation section of the condensable products. The syringe is primed at least 3 times with the incondensable phase, finally it is filled completely, the gas tank is closed and the mixture is analysed qualitatively, in order to understand which light products have formed.

2.3.5 Studies of deactivation phenomena: ^{1}H NMR relaxation measurements

In order to have further information on the adsorbate-catalyst interactions accompany for the two crystalline phases in the CTH reaction of ML and to understand the causes at an atomistic level of deactivation phenomena, we proceeded using two main approaches to the experimental study of the reactions: one study of NMR relaxation measurements and a theoretical study. In particular, for the NMR study we focused on the interactions between the two crystalline phases and the main molecules of the reactions, such as reactants, intermediates and products. For the theoretical study we focused on computationally reproducing cluster-type structures representative of the main crystalline sites present for the two catalysts, and then studying the adsorption of CO_2 and NH_3, in order to compare the results obtained with those reported in the TPD analysis; finally, we proceeded by studying the interaction of the catalyst with angelica lactone, the intermediate of the reaction, in order to explain certain deactivation phenomena.

^{1}H NMR relaxation measurements were carried out using a Magritek Spinsolve benchtop NMR spectrometer at the University of Manchester by Professor Carmine D'Agostino's group. In particular, it was operated with a ^{1}H frequency of 43 MHz, temperature of 25°C and at atmospheric pressure. The error of the measurements is around 3%. The two crystalline phases of zirconia were firstly soaked in the following solutions: *n*-octane; in the reaction solvents ethanol and ethanol; with ML and EL reagents; with the intermediate AL and the product GVL. The catalysts were left in the solutions for 24 hours, and subsequently removed from the liquids, dried with special paper filters to remove the remaining liquid but without removing it from the internal pores of the structure. Subsequently, the catalyst was inserted into a 5 mm NMR and the measurement was carried out after stabilizing the system.

The T_1 spin-lattice relaxation time was calculated using an inversion recovery pulse sequence with sixteen recovery delays in the range 1 ms – 5000 ms, performing 8 scans per step. The T_2 spin-spin relaxation time was calculated using the Carr-Purcell-Meiboom-Gill sequence, with an echo time of 120 μs and range of 50 to 500 echoes per step, with 8 scans per step.

2.3.6 Study of deactivation phenomena: computational approach

To study the catalytic systems under examination, a computational study was carried out, with the aim of evaluating the catalyst-adsorbate interactions. In particular, computational chemistry features valid tools for studying catalytic processes and understanding the intrinsic characteristics of a material. In carrying out simulations, all that needs to be taken into consideration is the cost of the machines used, the electricity and above all the cooling systems for the machines. These, compared to an experimental study, are significantly convenient from an economic point of view. In fact, in a work where the central theme is that of sustainability from an environmental point of view, a computational study is a valid alternative to additional laboratory experiments, which imply the consumption of chemical substances, the production of numerous scraps and waste, the use of potentially toxic and polluting substances. Consequently, the idea of pushing the research activity towards theoretical studies is becoming a standard that, besides being highly sustainable from an environmental and economic point of view, allows us to study the catalysts and their properties and interactions with the molecules of the reaction from an atomistic point of view, evaluating chemical interactions with atomistic resolution. In particular, in this work we focused on the study of catalyst-adsorbate interactions, in order to better understand the deactivation phenomena.

2.3.6.1 ***Fundamental of quantum mechanics***

Planck in 1900 proposed that black-body radiation emitted by microscopic particles such as electrons is limited to certain energy levels. To explain this phenomenon, quantum mechanics is necessary: in particular, de Broglie proposed that electrons had a twofold nature, both of matter (i.e. particles) and of waves (i.e. quantized). This introduces the concept of the wave function Ψ, which contains all the information to describe a system. By applying a Hamiltonian operator (H) to the wave function, this returns all the observable properties according to the famous (time-independent, non-relativistic) Schrödinger equation:

$$H\Psi = \mathrm{E}\Psi$$

where E is the scalar value of the observable properties, e.g. the energy.

The wave function is not a physical observable, but a complex-valued function, difficult to interpret according to the rules of classical mechanics, which represents the probability amplitude of a quantum state and its squared modulus ($\psi* \ \psi$, or $\| \ \psi^2 \ \|$) corresponds to a "probability density", e.g. the probability that a particle is found in a certain space.

The Hamiltonian operator for a molecule can be written as:

$$H = -\sum_i \frac{h^2}{4\pi m_e}\nabla_i^2 - \sum_k \frac{h^2}{4\pi m_k}\nabla_k^2 - \sum_k\sum_i \frac{e^2 Z_k}{r_{ik}} + \sum_{i<j}\frac{e^2}{r_{ij}} + \sum_{k<l}\frac{e^2 Z_k Z_l}{r_{kl}}$$

Where:

- *i* and *j* correspond to electrons,
- *k* and *l* to nuclei
- $\hbar$ is the Planck constant divided by 2π
- ∇^2 is the Laplacian operator
- m_e is the mass of the electron and m_k the mass of the nuclei
- *Z* the atomic number, *e* is the charge on the electron
- r_{xy} the distance between particles x and y

This molecular Hamiltonian can be simplified by the Born-Oppenheimer approximation, which considers the nuclei as fixed particles in space: in fact, being much heavier than the electrons, they move much more slowly to the point that they can be considered as fixed with respect to the motion of the electrons. Consequently, since the nuclei are considered fixed, their kinetic energy is zero, while the repulsive potential energy nucleus-nucleus can be considered as a constant (V_N). The equation can therefore be simplified for a given set of nuclei positions, i.e. a given molecular geometry, as follows:

$$H_{el}\,\Psi_{el}\,(q_i) = E_{el}\,\Psi_{el}\,(q_i)$$

where the wave function is reduced to an electronic wave function Ψ_{el}, depending on the coordinates of the electrons q_i, and the energy E_{el} is the energy of a given electronic state.

2.3.6.2 ***Density Functional theory***

The Density Functional Theory (DFT) was introduced in 1927 by Thomas and Fermi. [72-73] This theory introduces the concept of electronic density ρ to which is associated the total number of electrons (N) in the space, according to the equation:

$$N=\int \rho(\boldsymbol{r})dr$$

This is possible because the Hamiltonian depends only on the total number of electrons and the position and atomic numbers of the nuclei. The position of nuclei, approximated by a point charge, corresponds to the local maximum of ρ.

The turning point for the DFT theory occurred with an intuition by Kohn and Sham (KS) in 1965 based on using a Hamiltonian that considers non-interacting electrons; subsequently, the energy can be divided into specific components that are functionals of the density ρ, as following:

$$E[\rho(r)] = T_{ni}[\rho(r)] + V_{ne}[\rho(r)] + V_{ee}[\rho(r)] + \Delta T[\rho(r)] + \Delta V_{ee}[\rho(r)]$$

where, T_{ni} is the kinetic energy of the non-interacting system; V_{ne} is the electron-nuclei attraction and V_{ee} is the electron-electron repulsion defined in a classical Coulomb-like fashion, while the $\Delta T[\rho(r)]$ and $\Delta V_{ee}[\rho(r)]$ terms are corrections that account for interacting electrons and non-classical electron-electron repulsion (due their fermionic nature), which are normally considered as a single term called Exchange-Correlation functional, E_{xc} [ρ(r)].

The DFT theory, consequently, is a theory that can be considered as exact, but which must be solved with approximations since the exact nature of the exchange-correlation term is not known.

The term E_{xc} is normally expressed as a function of the electron density:

$$E_{xc}[\rho(r)] = \int \rho(r)\varepsilon_{xc}[\rho(r)]\ d\boldsymbol{r}$$

where ε_{xc} is the energy density, which depends on the electron density. This, according to the Local Density Approximation (LDA), can be calculated just considering the local electron density considering as a first approximation a uniform cloud of electrons, where the electron density is constant. This approximation is obviously inaccurate, since the electron density is not constant everywhere in space. Consequently, corrections called Generalized Gradient Approximation (GGA) were applied, according to which ε_{xc} is both a function of the electron density and its gradient.

From a mathematical and computational point of view, the DFT theory has similarities with the Hartree-Fock (HF) self-consistent field (SCF) theory based on the variational principle. In particular, the electron density can be initially guessed, which allows to evaluate the terms of the KS-Hamiltonian. Then the Schrödinger equation can be solved in the KS formalism, i.e. solving a secular equation, obtaining molecular orbitals energies from which a new electron density can be obtained, starting a new cycle until convergence is reached.

2.3.6.3 ***Exchange-Correlation Functionals***

The most widely used Exchange-Correlation functionals are of two main types: pure or hybrid. The pure functionals do not include terms from other 'theories', such as the exchange term borrowed from the HF theory. An example of a pure functional is BP86, composed of the Becke [71] exchange functional and the Perdew [72] correlation functional. These functionals have an inherent error, overestimating the energy barriers of chemical reactions. The HF theory tends, in contrast, to underestimate these energy barriers. In hybrid functionals, therefore, HF and DFT exchange terms are included, in order to balance these two types of errors. An example of a hybrid functional, used in this work, is the B3LYP [73-75], where there is a 20% of HF exchange.

2.3.6.4 Density of States (DOS)

Density of states (DOS) represents the number of states in a given energy level that electrons can occupy. In fact, a system cannot assume any energy but is bound to occupy discrete energy levels. DOS allows you to statistically define the states available for a given energy for a given quantum system. The DOS can be represented as curves and through them it is possible to study the electronic structure of a material. The DOS of a given system can be represented by the following equation:

$$DOS(E) = \frac{g_s}{V}\sum_{i}\delta(E - \varepsilon_k)$$

where δ is the delta Dirac function and ε_k is the set of eigenvalues of a single particle; g_s is the degeneration factor connected to the spin. Considering a system with a large number of states, the sum in the previous expression can be extended to an integral.

2.3.6.5 ***Basis sets***

Molecular orbitals can be expressed as the linear combination of atomic orbitals (LCAO), and used to build the initial guess of the density ρ to start the SCF cycle iterations. The atomic orbitals are defined using basis sets of mathematical functions. Slater-type orbitals (STO) reliably reproduce atomic orbitals, but are difficult to handle from a computational point of view. Gaussian-type orbitals (GTO), on the other hand, can be handled in a simpler way but do not represent the radial part of atomic orbitals very well. To solve this problem, basis sets can be constructed by contracting (i.e. by linear combination of) several ‘primitive’ GTOs (i.e. to fit the STO-like functions). The degree of contraction is indicated depending on the number of primitive gaussians used. In this work we used the 6-31G**(d,p) contracted basis set [75] for light atoms. This is a split-valence basis set [76] of Pople and al. From the nomenclature of the basis set it is possible to understand how many primitives have been used: in particular, the number before the "-" indicates the number of primitives used for the core orbitals; the number after the symbol “- “ indicates the number of primitives used for the valence orbitals. For the core orbitals only one contracted basis function is used, consisting of 6 primitives, while for the valence orbitals, there are two numbers, 3 and 1, so this is a valence double-ζ basis set. The “**” indicates that these are “polarization functions”, which include angular momenta higher than those in the valence orbitals of each atom. They "embrace" the flexibility of atoms to form bonds in any direction.

2.3.6.6 Effective core potential (ECP)

Considering heavy atoms and making calculations with a large number of them, it is complex to use complete basis sets for all electrons of each individual atom, since this would imply a high computational cost. Consequently, Effective Core Potentials (ECPs) come into play [77] replacing the core electrons with an effective potential that is added to the Hamiltonian. The core electrons, in fact, being more internal and shielded by the valence electrons, are less reactive and therefore less interesting to study for catalytic reactions. Consequently, they can be expressed through an effective potential which allows obtaining more approximate results but at a lower computational cost. As regards the valence electrons, which come into play in reactivity phenomena, these are expressed with standard basis set functions.

2.3.6.7 ***Cluster Modeling***

To study heterogeneous catalytic systems, a slab or cluster model can be used. In particular, this work focused on the latter.

Clusters can be defined as sets of atoms of finite and reduced number. The advantage of using this type of structure is that, having a limited number of atoms, it allows a considerable reduction in calculation costs and times. Furthermore, it is possible to model the cluster structures by fully representing the main structural characteristics of real catalysts, such as defects, exposed surface atoms, exposed crystalline planes, in order to create realistic models for the study of catalytic processes.

2.4 Results

2.4.1 Comparison between crystalline phases of zirconia

2.4.1.1 Comparison between crystalline phases of zirconia: synthesis and characterisation

The synthesis of the two crystalline phases of zirconia, *t*-ZrO_2 and *m*-ZrO_2, was carried out, according to the procedures described in chapter 2.3.1.1. In particular, a hydrothermal synthesis was carried out for the *m*-ZrO_2, while a synthesis by precipitation was carried out for *t*-ZrO_2: the *m*-ZrO_2, in fact, in conditions of ambient temperature and atmospheric pressure appears to be the thermodynamically stable phase; consequently, to synthesise *t*-ZrO_2, which is not stable under these conditions as reported in chapter 2.1.4, it was necessary to carry out a synthesis by a precipitation method rather than a hydrothermal synthesis, which would favour the formation of the thermally stable phase.

Characterisation of *t*-ZrO_2 and *m*-ZrO_2

The two catalysts, after being pulverised using a mortar, appear in the form of white powders.

To confirm the successful synthesis of the desired crystalline phases and to evaluate their specific surface area, XRD and BET analysis has been performed. As can be seen from Figure 22, a high purity tetragonal and a pure monoclinic phase have been synthesised. The blue *m* indicates the peaks corresponding to the monoclinic phase, while the red *t* indicates those corresponding to the tetragonal phase.

XRD

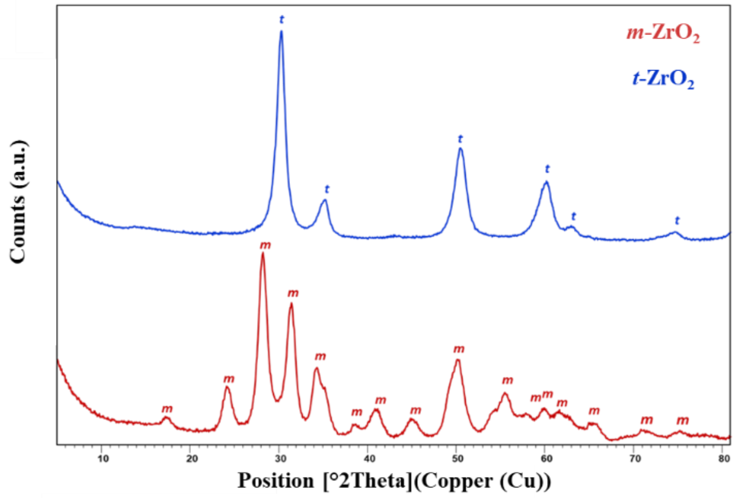

BET

Surface area *m*-**ZrO$_2$:** 117 m^2/g
Surface area *t*-**ZrO$_2$:** 120 m^2/g

Figure 22. XRD and BET analysis of synthesized *t*-ZrO$_2$ (blue) and *m*-ZrO$_2$ (red)

For the heterogeneous catalysts the reactions normally occur on the catalyst surface, because the most exposed reactive sites are present. In CTH-type catalysis the strength of the acidic and basic sites is essential to favour the reaction. To evaluate the specific surface areas and the number and density of the total acid sites (Brønsted and Lewis acid sites), BET and TPD-NH$_3$-CO$_2$ analysis have been performed. BET analysis shows that the two crystalline phases are characterised by a relatively high, yet similar, specific surface areas of 120 and 117 m^2/g for *t*- and *m*-ZrO$_2$ respectively. The fact that the two catalysts have the same surface area allows a comparison of the catalytic activity of the two phases with the same surface area.

The TPD-NH$_3$-CO$_2$ analysis have been performed studying the desorption of ammonia for acidic sites and the desorption of CO$_2$ for basic sites. Figure 23 shows the density of acidic and basic sites for *t*-ZrO$_2$ (in blue) and *m*-ZrO$_2$ (in red).

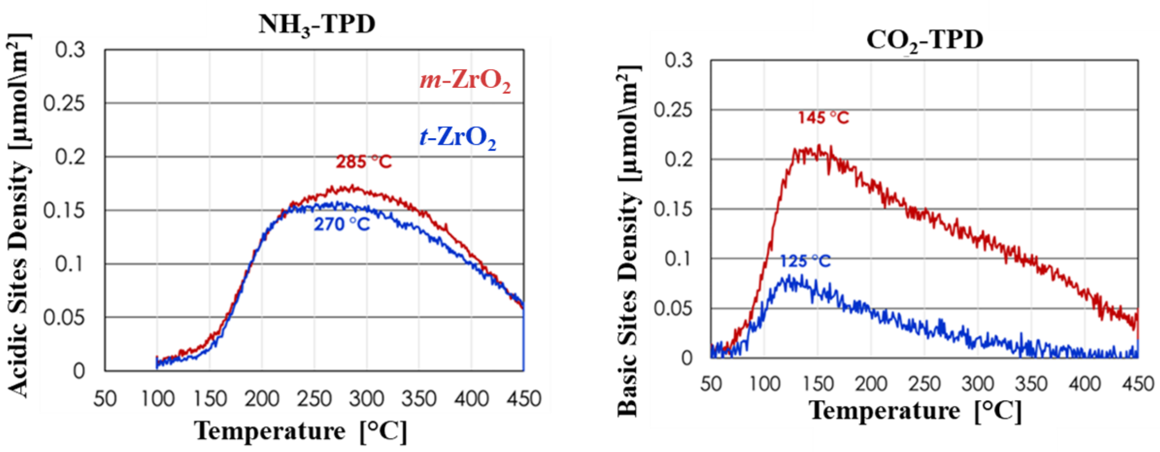

Figure 23. TPD analysis of *t*-ZrO_2 (blue) and *m*-ZrO_2 (red)

As regards the total acid sites both phases of zirconia show a very broad NH_3 desorption band ranging from 150 °C to 450 °C. *m*-ZrO_2 appears to have slightly stronger acid sites than *t*-ZrO_2 (with a maximum desorption temperature at 285 °C compared to the 270 °C of *t*-ZrO_2). However, in general, for the two crystalline phases, the presence of such a broad desorption band in such a wide range of temperatures indicates the presence for both phases of weak, medium and strong acid sites (in general, the higher is the desorption temperature of the target molecule, the greater is the strength of the site under consideration).

For what concern the basic sites, the major desorption of CO_2 for the two phases occurs at low temperatures, indicating the presence for the majority of basic sites with weak strength. For *m*-ZrO_2, the maximum desorption temperature is 145 °C, while for *t*-ZrO_2 it is 125 °C, indicating a greater presence of sites with higher basic strength for monoclinic zirconia compared to tetragonal; moreover, it can be seen from Table 1, the density of the basic sites of *m*-ZrO_2 (4.25 µmol/m^2) is much greater than that of *t*-ZrO_2 (1.18 µmol/m^2).

Table 1. Summary of TPD analysis on tetragonal and monoclinic zirconia

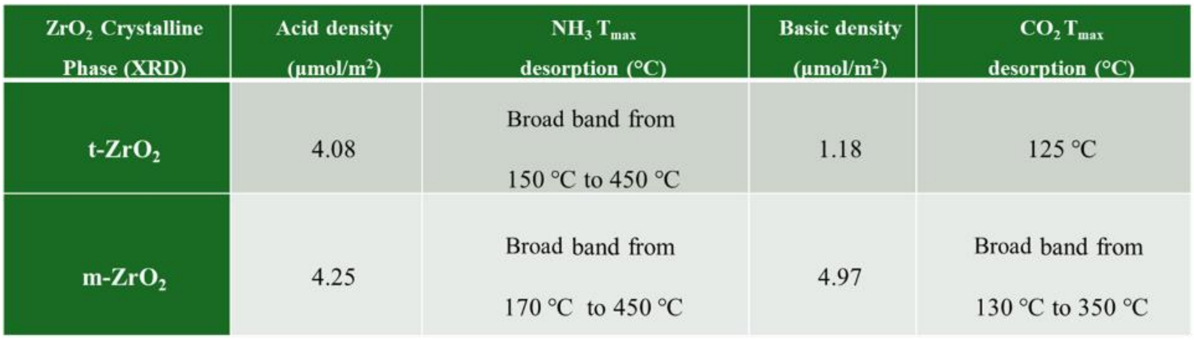

ZrO_2 Crystalline Phase (XRD)	Acid density (µmol/m^2)	NH_3 T_{max} desorption (°C)	Basic density (µmol/m^2)	CO_2 T_{max} desorption (°C)
t-ZrO_2	4.08	Broad band from 150 °C to 450 °C	1.18	125 °C
m-ZrO_2	4.25	Broad band from 170 °C to 450 °C	4.97	Broad band from 130 °C to 350 °C

Finally, DRIFT analysis was performed on the zirconia samples. In particular, the adsorption of Dimethyl pyridine (DMP) was studied. In particular, from the recorded spectrum we saw a predominance of Lewis acid sites compared to Brönsted acid sites in both crystalline phases: this is evident from the bands centered at 1600, 1580 and 1470 cm^{-1}, which correspond to ν8a, ν8b and ν19a DMP vibration modes, respectively (Figure 24).

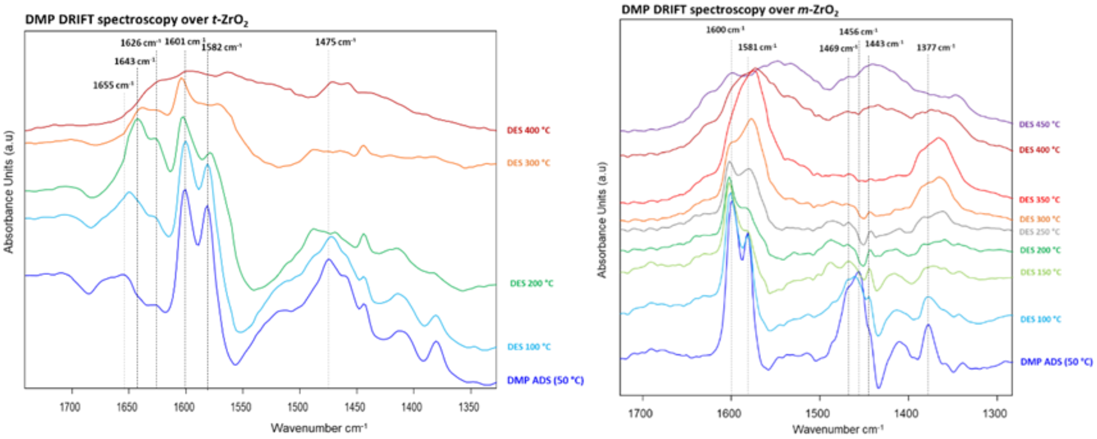

Figure 24. DMP- DRIFT spectra of *t*-ZrO_2 (left) and *m*-ZrO_2 (right)

2.4.1.2 Comparison between crystalline phase of zirconia: Catalytic tests in CTH of ML of GVL

2.4.1.2.1 Catalytic test in optimized conditions

Previous studies carried out by our research group focused on the CTH process of ML and ethanol in a continuous gas-phase reactor on *t*-ZrO_2.

In this work we studied the reaction under the same experimental conditions on *m*-ZrO_2, in order to evaluate the effect of the crystalline phase on the reaction. From the characterisation data of the two crystalline phases reported previously, it can be seen that the two zirconias synthesised have almost the same surface area: this result therefore allows their catalytic performance to be compared under the same reaction conditions with similar surface area. The reaction was carried out under the conditions optimised in the previous work for *t*-ZrO_2. The experimental conditions were the following: temperature of 250 °C, molar ratio ML:EtOH= 1:10 and contact time of 1 s.

The results of the two reactions using the two catalysts are shown below in Figure 25.

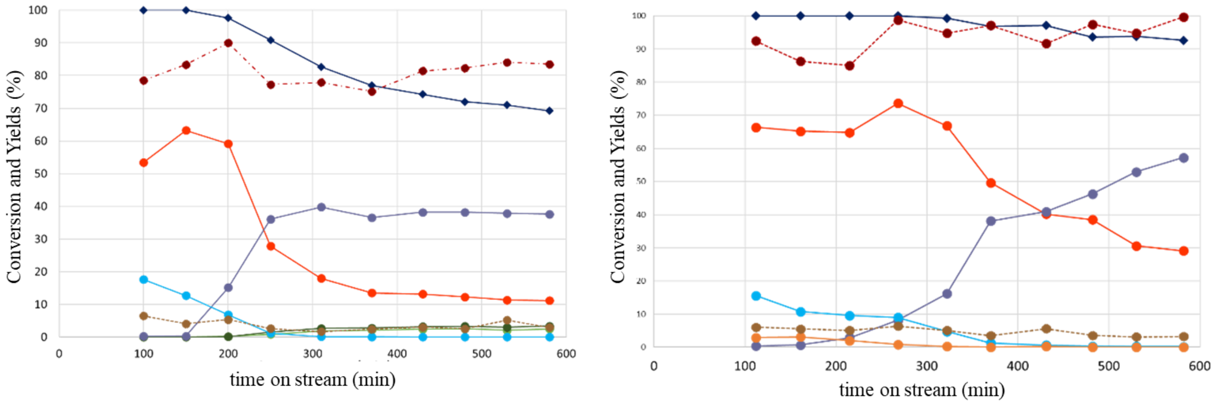

Figure 25. Catalytic results obtained in ML reduction *via* CTH using EtOH as H-donor over *m*-ZrO_2 (left) and *t*-ZrO_2 (right). Reaction conditions: molar ratio ML:EtOH=1:10, T=250 °C, □=1 s, %mol N_2:ML:EtOH=90.1:0.9:9. ML conversion (◆); EL (●); GVL (●); Ethyl GVL (●); □AL (●); □AL (●); Others (●); Yields sum/Conversion (●)

Initially the ML conversion is total for both catalysts. In the case of *m*-ZrO_2 it tends to drop rapidly after the first two hours, reaching 70% after 10 hours of reaction. In the first hours of reaction there is a high selectivity (around 63%) for the GVL, which is the desired product, with a slight formation also of the alkylated product, ethyl-GVL. However, after 200 min, there is a sudden drop in the production of GVL, with a change in chemoselectivity favouring the formation of ethyl levulinate, the transesterification product of ML. This result, in addition to the decrease in conversion observed, indicates a progressive deactivation of the catalyst and it also was confirmed by the carbon balance, which was around 80%, suggesting the possible formation of heavy products adsorbed on the surface of the catalyst, not detectable by GC-MS. The formation of these heavy products was also confirmed by the change in the colour of the catalyst, which went from white to deep brown, as reported in Figure 26.

Figure 26. Tetragonal zirconia catalyst pre (left) and post (right) reaction of CTH of ML to GVL

The catalytic results for *t*-ZrO_2 showed that the conversion remains complete up to 300 min, decreasing slightly up to about 95-92% in the following hours. The selectivity towards the GVL is around 68-73% in the first 5 hours of reaction, with a peak at 73% around 250 min. Subsequently, the yield of GVL begins to decrease together with an increasing in the yield of ethyl levulinate, as it was observed for *m*-ZrO_2, although in a less sudden way.

In conclusion, *t*-ZrO_2 has greater stability and allows to obtain a good yield of GVL in these specific reaction conditions, even if in the last few hours a deactivation of the catalyst has begun to be seen; moreover, from the higher carbon balance (about 90%) it can be seen that it has a lower tendency to form heavy carbon products compared to *m*-ZrO_2,, as confirm form TGA analysis on catalysts post reaction, reported in Table 2.

Table 2. Accumulation of heavy compounds obtained from TGA over spent ZrO2 catalysts

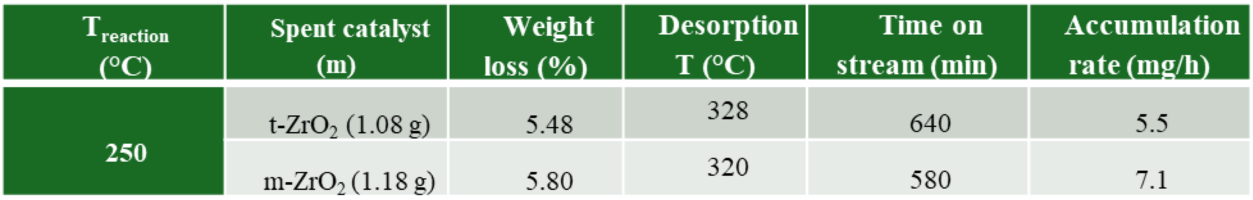

$T_{reaction}$ (°C)	Spent catalyst (m)	Weight loss (%)	Desorption T (°C)	Time on stream (min)	Accumulation rate (mg/h)
250	t-ZrO_2 (1.08 g)	5.48	328	640	5.5
	m-ZrO_2 (1.18 g)	5.80	320	580	7.1

For TGA analysis we can see that there is a smaller accumulation of organic products on *t*-ZrO_2 in comparison with monoclinic. Moreover, *m*-ZrO_2 shows worse catalytic performance for the reaction under examination, with a faster deactivation. The reason for this may be due to the presence of a greater number of basic sites, as reported by the CO_2-TPD analysis, which can favour the formation of ALs and their oligomerisation, leading to the formation of heavy products which block the catalytic sites of the catalyst.

2.4.1.2.2 Effect of reaction temperature in CTH reaction

In order to evaluate the effect of reaction temperature for the two crystalline phases, the CTH reaction of the ML was carried out under the same conditions seen previously at lower and higher temperature (200 and 300 °C).

In Figure 27 the results for T=200 °C are reported.

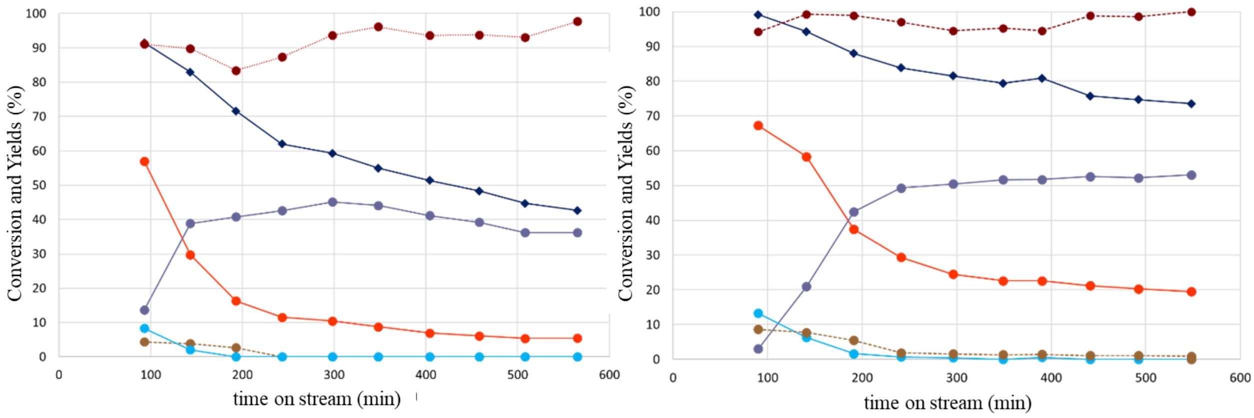

Figure 27. Catalytic results obtained in ML reduction via CTH using EtOH as H-donor over *m*-ZrO$_2$ (left) and *t*-ZrO$_2$. Reaction conditions: ML:EtOH = 1:10 (molar ratio), T = 200 °C, τ = 1 s, % mol N$_2$:ML:EtOH = 90.1:0.9:9. Conversion (◆); EL (●); GVL (●); Ethyl GVL (●);Others (●); Yields sum/ Conversion (●)

For both crystalline phases a rapid deactivation of the catalyst is observed at 200 °C, evidenced by the decrease of the conversion of ML and by the change in chemoselectivity from GVL to EL already at short reaction time (more evident for *m*-ZrO$_2$). This is probably because such a low reaction temperature fails to favour the CTH step of hydrogenation of the ALs. Consequently, the formed ALs tend to oligomerise, leading to a rapid deactivation of the catalyst. At this temperature there are not big difference in the catalytic performance between the two crystalline phases. This indicates that the effect of the crystalline phase is found in the CTH step of hydrogenation of ALs at GVL, which in this case is deprived by using low reaction temperatures for both crystalline phases.

In Figure 28 the results of the CTH of ML at 300 °C are reported.

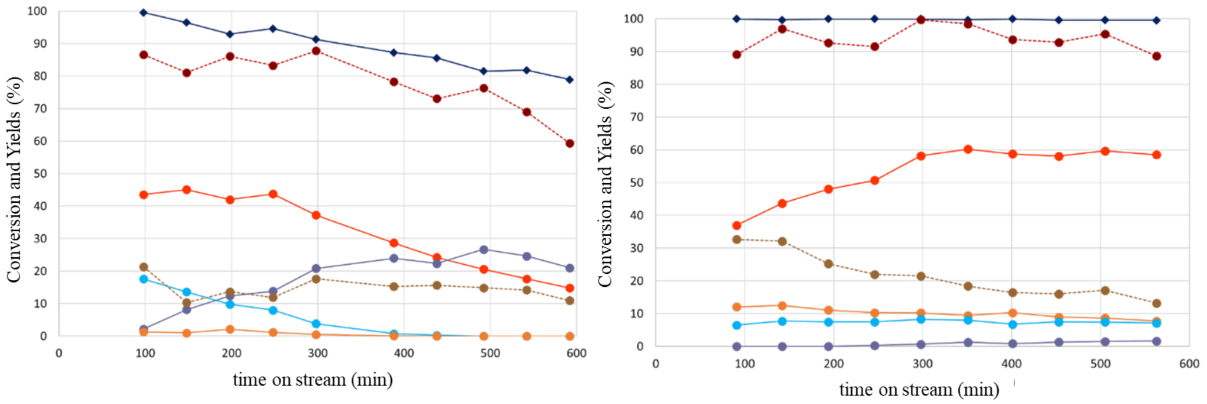

Figure 28. Catalytic results obtained in ML reduction via CTH using EtOH as H-donor over *m*-ZrO$_2$ (left) and *t*-ZrO$_2$ (right). Reaction conditions: ML:EtOH = 1:10 (molar ratio), T = 300 °C, τ = 1 s, % mol N$_2$:ML:EtOH = 90.1:0.9:9. Conversion (◆); EL (●); GVL (●); Ethyl GVL (●); EP (●); Others (●); Yields sum / Conversion (●)

Regarding *m*-ZrO_2, the conversion of ML is initially total, but tends to decrease over time until it reaches 80% after 10 hours of reaction. The yield of GVL in the first hours of reaction up to 280 min settles around 42-45%, but subsequently decreases due to a variation in chemioselectivity towards the formation of EL, where in the last hours the yield exceeds that of GVL. This result, as explained previously and in addition to the low carbon balance observed, indicates a deactivation of the catalyst due to the formation of heavy products as it has been observed in the previous reported cases. Already from the first hours of reaction, a high formation of by-products (Others) is noted, with yields ranging from 10 to 18%, and a moderate formation of Ethyl GVL: the catalyst, at 300 °C, therefore tends to favour consecutive reactions, leading to the formation of by-products. Regarding *t*-ZrO_2, however, a different result was observed. The ML conversion remains total for the entire reaction time. The selectivity towards the formation of GVL increases as the reaction time increases, going from 38% at 100 min of reaction to approximately 60% towards the last hours of reaction (from 300 to 580 min). The formation of EL in this case is minimal. Only after 300 min there is a small formation of EL (around 2-3% yield). Also in this case, as for *m*-ZrO_2, there is a notable formation of Others, which however decreases during the reaction, and of Ethyl GVL, which remains almost constant over time. These consecutive reactions favoured by high temperatures tend to decrease selectivity towards the GVL. It is also important to note the formation of a reasonable quantity of Ethyl Pentenoates (EP), with a selectivity of around 8-12% for tetragonal zirconia, which appear to be consecutive products of the GVL, obtained from its ring-opening and subsequent dehydration.

Figure 29 shows summary of the catalytic results for tetragonal and monoclinic zirconia at 200-250-300 °C, focusing on the Conversion and Yields at 2 and 6 hours of reaction.

	Temperature (°C)	Time of reaction (h)	Conversion ML (%)	Yield GVL (%)	Yield EP (%)	Yield EL (%)	Yield Ethyl GVL (%)	Yield Others (%)
t-ZrO_2	200	2	98	63	0	17	8	9
		6	79	23	0	52	0	1
	250	2	100	66	3	0	12	7
		6	97	58	0	28	6	6
	300	2	100	42	13	0	7	32
		6	100	60	10	1	8	18
	Temperature (°C)	Time of reaction (h)	Conversion ML (%)	Yield GVL (%)	Yield EP (%)	Yield EL (%)	Yield Ethyl GVL (%)	Yield Others (%)
m-ZrO_2	200	2	82	32	0	39	0	4
		6	56	9	0	46	0	0
	250	2	100	63	0	0	14	6
		6	79	12	0	38	0	2
	300	2	100	44	0	8	18	12
		6	87	32	0	17	1	24

Figure 29. Summary of CTH of ML at different temperature (200-250-300 °C) on tetragonal and monoclinic zirconia

In conclusion, from the results obtained we can conclude that at lower reaction temperature, for example at 200 °C, the CTH reaction is not favoured: CTH of ML tends to block at the ALs cyclization step, which leads to the formation of oligomers that deactivate the catalyst. At higher reaction temperature, for example at 300 °C, due to the high reaction temperature there is a greater formation of by-products and consecutive reactions to the formation of the GVL, decreasing the selectivity towards the latter. In comparison, at 250 °C the selectivity towards the GVL is favoured, remaining quite stable over time for tetragonal zirconia, with nevertheless a deactivation of the catalyst in the last hours of the reaction. For monoclinic zirconia, the selectivity towards the GVL is high in the first hours of the reaction but drops quickly. the cause of this result can be found in the strength and density of the basic Lewis sites, which favour the oligomerisation of the ALs, leading to a sudden deactivation of the catalyst, with a significant change in selectivity towards the formation of EL as it has been observed.

Comparing the two crystalline phases we see that at 250 °C and 300 °C, after two hours of reaction the selectivity towards the formation of GVL is almost the same for the two crystalline phases. However, a significant change is observed at longer reaction times (6h) with a greater deactivation of the monoclinic compared to the tetragonal and with a change in chemoselectivity. Instead at 200 °C, monoclinic zirconia is much less active than tetragonal zirconia, probably due to the low reaction temperature, which disfavours the CTH reaction and favours the formation of oligomers from ALs, which are already more favoured in the monoclinic phase.

2.4.1.2.3 Effect of H-donors in CTH reaction

In CTH reactions, alcohol plays a fundamental role since it acts as a donor of H, therefore it is another critical parameter to investigate for the reaction. As explained previously, the more stable the carbocation that is formed after the donation of hydrides is, the more the donation of H will be favoured and consequently the CTH reaction.

This study compared the effect of three alcohols as the desired model molecules, two primary (methanol and ethanol) and a secondary one (isopropanol) in the CTH reaction of ML on the two crystalline phases of zirconia, tetragonal and monoclinic. The results using methanol are shown below in Figure 30.

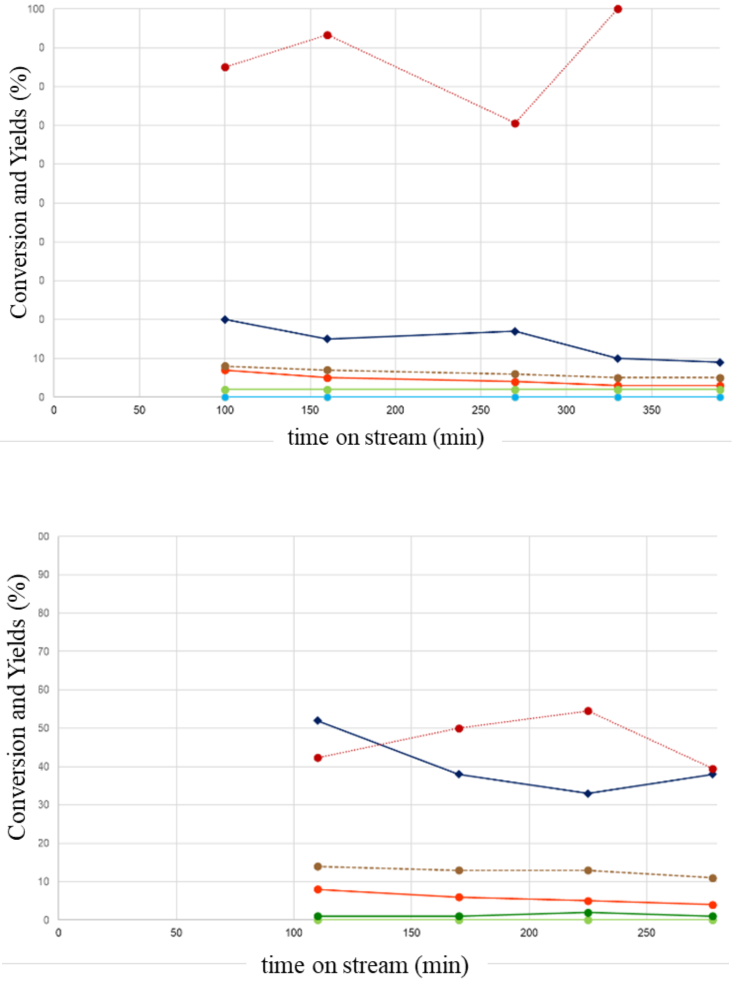

Figure 30. Catalytic results obtained in ML reduction via CTH using MeOH as H-donor over *m*-ZrO_2 (up) and *t*-ZrO_2 (down). Reaction conditions: ML:MeOH = 1:10 (molar ratio), T = 250 °C, τ = 1 s, % mol N_2:ML:MeOH = 90.1:0.9:9. Conversion (◆); EL (●); GVL (●); Ethyl GVL (●); EP (●); Others (●); Yields sum / Conversion (●)

In both cases the conversion of ML is low, from 20 to 10% for *m*-ZrO_2 from 32 to 52% for *t*-ZrO_2. The yield of GVL is very sufficient for both phases, around 5-8%; a slight formation of ALs is noted for both phases. These results make it clear that methanol, under these reaction conditions, does not function as good H-donor, since the hydrogenation reaction of the ALs is deprived. Instead, we see that there is a discrete formation of by-products (Others), due to the favouring of side unfavoured reactions to the formation of GVL. The decrease in the conversion of ML, more evident for *m*-ZrO_2, may also indicate a poisoning of the catalyst following the oligomerisation of the ALs, since the hydrogenation to GVL is not favoured, as can also be seen from the brownish colour of the catalysts after the reaction.

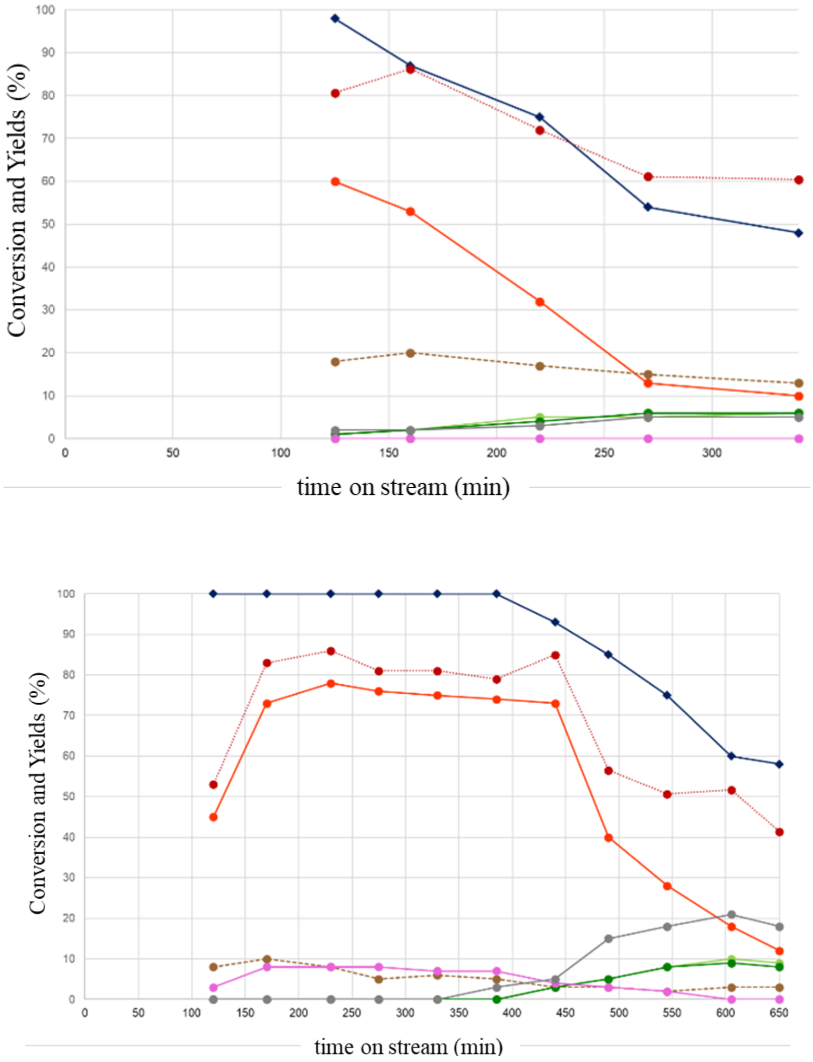

Figure 31. Catalytic results obtained in ML reduction via CTH using Isopropanol as H-donor over *m*-ZrO_2 (up) and *t*-ZrO_2 (down). Reaction conditions: ML:i-PrOH = 1:10 (molar ratio), T = 250 °C, τ = 1 s, % mol N_2:ML:i-PrOH = 90.1:0.9:9. Conversion (◆); EL (●); GVL (●); Ethyl GVL (●); PropylPentenoate(●); Propyl Levulinate(●); Others (●); Yields sum / Conversion (●)

Using isopropanol as H-donor, it can be seen from Figure 31 that initially there is a good selectivity for the GVL and yield for both catalysts. Using *m*-ZrO_2 there is a yield of 60% at 125 min of reaction, with an almost total ML conversion. Immediately afterwards, the conversion drops drastically, decreasing in parallel the yield of GVL and increasing the yield of propyl levulinate, which is the transesterification product of ML, which is formed in the presence of isopropanol. For *t*-ZrO_2, the GVL conversion remains total up to about 380 min, with a constant selectivity towards the GVL of around 72-78%, which then drops rapidly in parallel with the decrease in conversion (to 58% at 650 min) and the increase in the yield of propyl levulinate (around 18-20% at 600-650 min). Also in this case, over a long period of time there is a progressive deactivation of the catalyst. This observation is also confirmed by the increase in the yield of the ALs and by the poor carbon balance (around 40- 56% after 480 min of reaction), which indicates a possible formation of heavy products in agreement with previous observations. The deactivation of the catalyst is even more sudden than when ethanol as H-donor is used, where after 10 hours of reaction the yield of GVL is around 30% and the conversion is around 92%, while in this case after 10 hours the yield of GVL is around 10% and the conversion is reduced to 58%. For both crystalline phases there is a greater production of Others compared to the use of ethanol, which thus favouring side-undesired reactions and therefore leads to a faster deactivation of the catalyst.

Summarizing the results obtained, it can be concluded that in general, regardless of the type of alcohol used as H-donor, under the specific experimental reaction conditions reported, tetragonal zirconia works better than monoclinic zirconia in the H-transfer reaction of ML to GVL. Furthermore, ethanol seems to be the most suitable alcohol as H-donor under these experimental conditions, due to the fact that with the use of tetragonal zirconia slower deactivation of the catalyst is observed.

2.4.1.3 ^{1}H NMR relaxation results: study of catalysts deactivation

The research group of Professor Carmine D’Agostino of University of Manchester, Oxford Road (Department of Chemical Engineering) has been involved in carrying out ^{1}H NMR relaxation studies in order to evaluate the adsorption forces of different target molecules on the surface of the catalysts, to better understand the deactivation phenomena. In particular, the adsorption of ML, α-AL (reaction intermediate), GVL (reaction product, EL (by-product formed that indicates the deactivation of the catalyst) and alcohols, such as ethanol and methanol were studied. These studies were performed using the target molecules in the liquid phase, even if in normal reaction conditions they are present in gas phase for the high temperature. In fact, the purpose of this study was not to reproduce the specific reaction conditions, but to provide general information on the interaction between the adsorbate molecule and the catalytic surface of the catalyst, which can give important insights into the results obtained in the gas phase. [78-80].

The pores of ZrO_2 catalysts were filled with the probe liquid of interest and the spin-lattice (T_1) and spin-spin (T_2) relaxation time constants were determined using the inversion recovery and CPMG pulse sequence.

The relaxation time T_1 and T_2 are calculated as follows:

$$\frac{1}{T_{1,pore}} = \frac{1}{T_{1B}} + \rho_1 \frac{S}{V}$$

$$\frac{1}{T_{2,pore}} = \frac{1}{T_{2B}} + \rho_2 \frac{S}{V}$$

$T_{i,pore}$ (where i=1,2) indicates the relaxation time of the solvent bulk; T_{iB} (where i=1,2) indicates the relaxation time of the liquid in the pores; ρ_i is the surface relaxivity parameter, factor that indicates how effectively a molecule interacts with a surface; S\V is the surface of volume ratio. Considering that the term T_{iB} is generally smaller than $T_{i,pore}$, the equation can be approximated as follows:

$$\frac{1}{T_{i,pore}} \approx \rho_i \frac{S}{V}$$

If T_1 and T_2 are determined for the same target molecule in the same porous medium (catalyst in this case), the S/V factor is constant, consequently the equation can be further simplified in this way:

$$\frac{T_1}{T_2} \approx \frac{\rho_2}{\rho_1}$$

In this way the interactions between the target molecule and the catalyst surface can be measured by this ratio.

In particular, higher is T_1/T_2, stronger is the interaction between the molecule and the surface of the catalyst [81,82].

In table 3 the T_1 and T_2 values for all the molecules in consideration are reported.

Table 3. T_1, T_2 and T_1/T_2 values of various probe molecules imbibed within the pores of the different phase ZrO_2 catalysts. The approximate error of all values is ±3 %

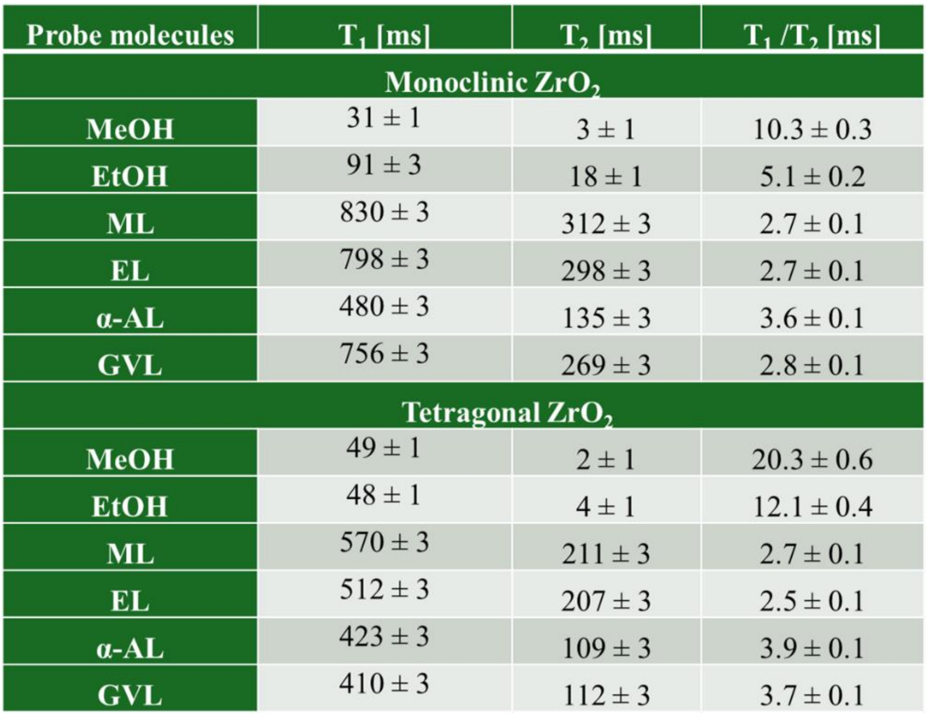

Probe molecules	T_1 [ms]	T_2 [ms]	T_1/T_2 [ms]
Monoclinic ZrO_2			
MeOH	31 ± 1	3 ± 1	10.3 ± 0.3
EtOH	91 ± 3	18 ± 1	5.1 ± 0.2
ML	830 ± 3	312 ± 3	2.7 ± 0.1
EL	798 ± 3	298 ± 3	2.7 ± 0.1
α-AL	480 ± 3	135 ± 3	3.6 ± 0.1
GVL	756 ± 3	269 ± 3	2.8 ± 0.1
Tetragonal ZrO_2			
MeOH	49 ± 1	2 ± 1	20.3 ± 0.6
EtOH	48 ± 1	4 ± 1	12.1 ± 0.4
ML	570 ± 3	211 ± 3	2.7 ± 0.1
EL	512 ± 3	207 ± 3	2.5 ± 0.1
α-AL	423 ± 3	109 ± 3	3.9 ± 0.1
GVL	410 ± 3	112 ± 3	3.7 ± 0.1

In general, as can be seen from Table 3, alcohols interact much more strongly with the catalytic surface than with other molecules, and, in particularly, more strongly on *t*-ZrO_2 than on *m*-ZrO_2. Probably the alcohols interact with the hydroxyl groups present on the two zirconia and especially with the Lewis acid groups present. The greater interaction of alcohols with *t*-ZrO_2 is probably due to the presence of a complex H-bonding network, which geometrically can favour the adsorption of alcohols on this crystalline phase compared to the other. Since alcohol is the H-donor molecule, having a time of residence on the surface of *t*-ZrO_2 greater than *m*-ZrO_2, the CTH reaction is favoured more on *t*-ZrO_2, in agreement with the catalytic results obtained. Furthermore, a greater interaction of the alcohol with the catalyst surface can be competitive to the adsorption of carbonaceous products which poison the catalyst, increasing its stability and therefore its activity.

As far as ML, EL and AL are concerned, the interaction between the two crystalline phases of zirconia is almost the same for both molecules. Also in the case of the GVL it can be seen that the interaction is very similar, slightly stronger for the tetragonal.

2.4.1.4 Computational results: study of catalysts deactivation

In order to obtain information on the catalytic mechanism at the atomistic level and understand better the difference of the catalytic activity we have observed, we performed a computational study based on DFT and atomistic cluster modelling of the two ZrO_2 crystalline phases under study. Upon optimization of the ground-state structures of the ZrO_2 clusters, we proceeded to study the adsorption of target molecules.

For the representation of the zirconia catalysts, it was decided to model cluster-type structures because we aimed at adsorption of the target molecules on specific, Lewis acidic and basic adsorption sites.

In particular, all the calculations have been performed at DFT level using the set of programs *Gaussian 16* [83]. Geometric optimizations were carried out using hybrid and non-hybrid functionals, i.e. B3LYP, PBE0 and PBE [71-75]. Stuttgart effective core potential has been employed for the Zr atoms [77], while 6-31G** basis set [75-76] was used for light atoms (H, C, N and O). A larger basis set for light atoms (i.e. 6-311++G**) was used to calculate the adsorption geometries. The counterpoise correction was applied to take into account the basis set superposition error (BSSE).

The adsorption energy (AE) of the adsorbate (ads) on the nanoparticles (NP) was calculated according to the following equation:

$$AE = E_{NP+ads} - (E_{NP} + E_{ads})$$

2.4.1.4.1 Modelling of clusters

The developed cluster models of the two crystalline phases of zirconia were inspired by the structure modelled by Puigdollers et al [58] for *t*-ZrO_2. The procedure followed is reported in detail below:

- The coordinates of the unit cells of the two crystalline phases have been downloaded from the Materials Project program [84] in (x,y,z) format.

- The unit cells were reproduced three-dimensionally in space using the VESTA program, in order to increase the number of atoms of the material obtaining a bulk-like structure.

- The obtained structures were cut along the thermodynamically most stable surface planes in all directions, obtaining a nanoparticle type structure, as shown in Figure 32. For *t*-ZrO_2 we cut along the plane (101) and those crystallographically equivalent, for *m*-ZrO_2 along the plane (-111) and crystallographically equivalents.

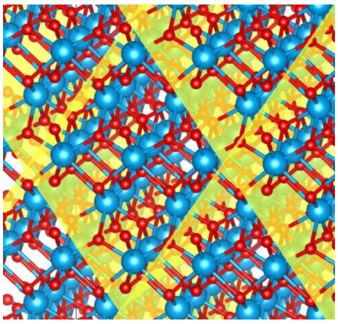

Figure 32. Most stable exposed surface planes (in yellow) for *t*-ZrO_2

Tetragonal cluster

The obtained *t*-ZrO_2 cluster is highly symmetrical and shows only exposed surfaces of the (101) family. The obtained structure has a $Zr_{19}O_{32}$ stoichiometry, therefore with an excess of Zirconium atoms.

We proceeded by cutting some terminal oxygen atoms of the cluster, with the aim of obtaining a stoichiometric structure $Zr_{16}O_{32}$, cutting 3 oxygen atoms, and a structure with excess oxygen $Zr_{13}O_{32}$, cutting 6 oxygen atoms, specifically the ones in vertex position. The three structures thus obtained were optimised at the DFT level (Figure 33).

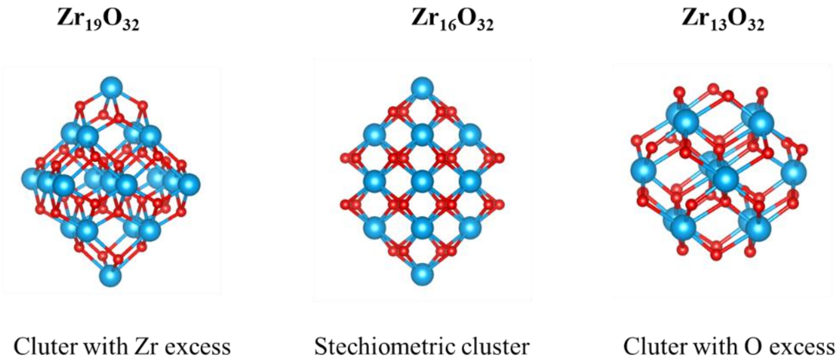

$Zr_{19}O_{32}$ $Zr_{16}O_{32}$ $Zr_{13}O_{32}$

Cluter with Zr excess Stechiometric cluster Cluter with O excess

Figure 33. Optimized *t*-ZrO_2 clusters at the DFT level

Monoclinic cluster

To model the *m*-ZrO_2 cluster, the same procedure reported previously for the tetragonal zirconia was followed, although the crystalline phase is less symmetrical than the tetragonal one. In this case we proceeded by cutting along the thermodynamically more stable surfaces (-111), trying to reach a stoichiometry as close as possible to that of the *t*-ZrO_2 clusters. The structure obtained, with $Zr_{18}O_{33}$ stoichiometry, was finally optimised to the same level of theory as *t*-ZrO_2 (shown in Figure 34).

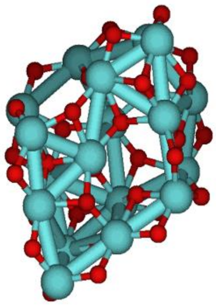

Figure 34. The $Zr_{18}O_{33}$ DFT cluster model of *m*-ZrO_2

2.4.1.4.2 Exchange-Correlation functional benchmark

The choice of the E_{XC} functional to use for DFT computations of the ZrO_2 systems is not trivial, due to the absence of an extended benchmark study in literature. This choice is important since it can significantly affect the geometry of the ground-state minimum and its electronic structure, including the DOS and the energy gap between the valence and conduction bands. We proceeded by testing different types of E_{XC} functional and comparing the results obtained with those reported by Puigdollers and co-workers and with experimental data obtained using the UV-Vis diffuse reflectance technique. In particular, we focused on three functionals: one of the GGA type, the PBE, and two hybrid functionals, PBE0 and B3LYP (see 2.3.6.3 section).

First, it was analysed the effect of different functionals on the ground-state minimum geometry on the $Zr_{19}O_{32}$ *t*-ZrO_2 cluster, measuring the average Zr-Zr distance and the average Zr-O distance (see Table 4) and comparing the results obtained with those reported by Puigdollers (using the PBE+U functional) and with the experimental average distances of the bulk structure.

Table 4. Zr-Zr and Zr-O distances in bulk structure (experimental) and nanoparticles structure (calculated) using different functionals for $Zr_{19}O_{32}$ *t*-ZrO_2 cluster.

	$\langle d\rangle_{Zr-Zr}$/(Å)	$\langle d\rangle_{Zr-O}$/(Å)
Bulk	3.68	2.27
B3LYP	3.34	2.16
PBE0	3.30	2.14
PBE	3.33	2.16
PBE+U[50]	3.18	2.18

There is not a particular difference in the Zr-Zr and Zr-O distances using the different functionals. The choice of functional therefore does not seem to affect much the cluster structure. In general, during the geometry optimisation, the structure in the clusters tends to contract compared to the bulk.

Therefore, we proceeded by evaluating the effect of the E_{XC} functional on the electronic structure and the band gap. To do this, Partial-DOS (PDOS) for Zirconium atoms (in blue) and Oxygen atoms (in red) using the different functionals were computed, as reported in Figure 35. Table 5 shows the band gap values (in eV) calculated from the results obtained by comparing them with the references reported in the work of Puigdollers et al. [58] and with the experimental UV-Vis diffuse reflectance.

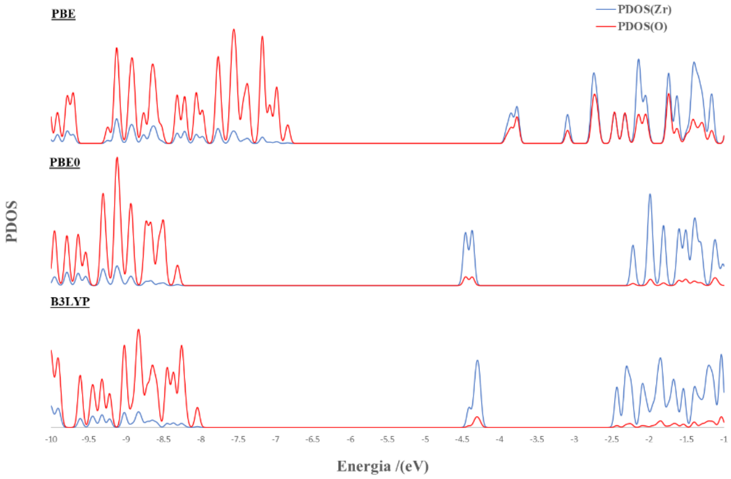

Figure 35. Projected Density of states computed using different E_{XC} functionals for $Zr_{19}O_{32}$ *t*-ZrO_2 cluster.

Table 5. Experimental and calculated band gaps using different functionals for $Zr_{19}O_{32}$ *t*-ZrO_2 cluster. The reported PBE+U has been reported from Puigdollers at al.'s work [58].

	Band gap (eV)	
	Results	Reference [50]
PBE	3.8	4.0
PBE0	6.1	6.3
B3LYP	5.6	/
PBE+U	/	4.3
	Experimental Band gap (eV)	
UV-Vis diffuse reflectance	5.5	

From the values obtained it can be seen that the PBE functional tends to underestimate the band gap comparing to the experimental one, while PBE0 tends to overestimate it. The results agree with those reported by Puigdoller [58], with a difference of about 0.2 eV. The E_{XC} functional that features the closest band gap to experiments is B3LYP, being then used in the rest of the work also for other ZrO_2 cluster structures and for the study of adsorption. In fact, B3LYP is widely used for organic molecules and it is expected to work properly for the adsorbates as well.

2.4.1.4.3 Coordination of cluster atoms

In the study of catalyst-adsorbate interactions it is important to identify all catalytic sites, in order to evaluate the reasons for possible different adsorption energies and geometries. Furthermore, it is important to understand, which are the possible catalytic sites present in the bulk catalyst, and which sites they correspond to in the cluster models.

By studying the obtained structures, it can be seen that there are mainly two types of sites: the edges and the vertexes. The edges have an average coordination of 5.1 and 6.0 for *m*-ZrO_2 and *t*-ZrO_2, respectively. These are the sites present with coordination closest to those (5 and 7 respectively) of the exposed surfaces (-111) and (101) of *m*-ZrO_2 and *t*-ZrO_2, respectively. These sites therefore appear to be the most representative of the exposed surfaces in nanoparticles, as they are the most widespread. As regards the vertex sites, they are those with the lowest coordination, and appear to have an average coordination of 4.1 and 4.0 for monoclinic and tetragonal, respectively. These sites represent possible defects present on the catalytic surfaces, with deficiencies of zirconium atoms, which can correspond to the most reactive because of their undercoordination.

2.3.1.4.4 Study of Lewis sites

On the DFT optimised ground-state structures it was decided to study first, by adsorption of target molecules, the strength of the Lewis acidic and basic sites. This study was carried out with the aim of validating the models created, evaluating the agreement of the data obtained with the experimental ones obtained through TPD analysis. NH_3 and CO_2 were chosen as target molecules, respectively to study the acid sites and the basic sites, because they are the same gases used for the TPD analysis. As explained in previous chapters, the strength of Lewis basic and acidic sites is fundamental in CTH mechanism.

Study of Lewis acid sites: adsorption of NH_3

For the study of acid sites we proceeded by studying the adsorption of the ammonia focusing on the Lewis acid sites. In particular, for the initial structures NH_3 was positioned with the Ionepair of nitrogen facing the Zr atom, with a Zr-N distance corresponding to that reported in the literature. Two vertex sites and two edge sites were studied. The adsorption energy was calculated according to the following equation:

$$Ads\ energy = E_{ZrO_2+NH_3} - E_{ZrO_2} + E_{NH_3}$$

The same equation was used to calculate the adsorption energies for all the adsorbates under study. The calculated adsorption energies for ammonia adsorption on $Zr_{19}O_{32}$ *t*-ZrO_2 and $Zr_{18}O_{33}$ *m*-ZrO_2 cluster are reported in Table 6.

Table 6. Adsorption energy of NH_3 on m-ZrO_2 and t-ZrO_2 on the main sites studied, both vertex and edges.

NH_3 adsorption	Monoclinic (kcal/mol)	Tetragonal (kcal/mol)
Vertex (1)	-28.9	-21.4
Vertex (2)	-29.2	-22.2
Edge (1)	-28.5	-28.9
Edge (2)	-25.4	-28.7

Figure 37 shows the most stable energy-optimised structures of NH_3 adsorption on the two crystalline phases of zirconia, $Zr_{19}O_{32}$ *t*-ZrO_2 and $Zr_{18}O_{33}$ *m*-ZrO_2 clusters. From the adsorption energies we note that, as regards the edge sites, which are more representative of the sites present in the real catalyst, the adsorption energy between the two phases is almost the same for the most stable sites (-28.5 kcal/mol and -28.9 kcal /mol for *m*-ZrO_2 and *t*-ZrO_2 respectively). This suggests that the two crystalline phases generally exhibit a comparable Lewis acid site strength, in agreement with the results of the TPD analysis.

As far as the vertex is concerned, we notice a substantially higher adsorption energy for monoclinic zirconia (-29.2 kcal/mol for the site with the highest adsorption energy) compared to the tetragonal one (-22.2 kcal/mol for the site with the highest adsorption energy). This may explain the main difference observed in temperature in NH_3 desorption peak in the TPD analysis, i.e. the presence of a minimal part of higher energy Lewis acid sites for *m*-ZrO_2 compared to *t*-ZrO_2 (see chapter 2.4.1.1).

In general, however, comparing the two sites with stronger adsorption energy, a vertex for the *m*-ZrO_2 (-29.2 kcal/mol) and an edge for *t*-ZrO_2 (-28.9 kcal/mol), it can be concluded that the acidic sites of Lewis have a comparable energy for the two phases, as also confirmed by the almost equal Zr-N distance for the two phases, 2.42 Å and 2.40 Å for *m*-ZrO_2 and *t*-ZrO_2 respectively.

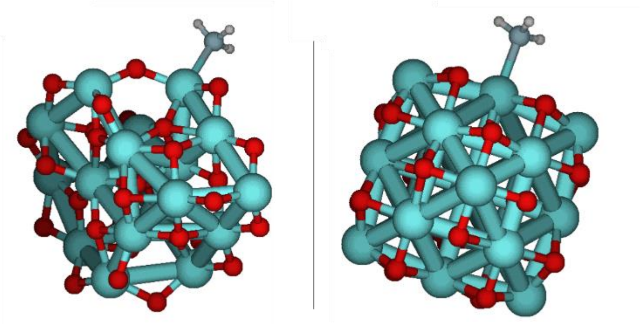

Figure 37. Adsorption of NH_3 on $Zr_{18}O_{33}$ *m*-ZrO_2 (left) and $Zr_{19}O_{32}$ *t*-ZrO_2 (right) on the site with the largest adsorption energies.

Study of Lewis basic sites: CO_2 adsorption

To study the basic Lewis sites, we proceeded according to the same logic as the acidic sites, but this time by adsorbing a molecule of CO_2. The initial structure was created by placing the C of CO_2 on an oxygen (basic site) of the zirconia. During the optimisation for all the CO_2-cluster structures studied, one of the oxygens of CO_2 tends to bind to a nearby Zr atom, forming a carbonate-like surface species (see Figure 38). Since the interaction with basic sites implies a donation to the CO_2 anti-bonding π^* orbital and a consequent elongation of the C-O bond, with deviation from the linearity of the free CO_2 molecule. Consequently, this deviation can be an indicator of the basicity of the sites: the more stretched the C-O bond and the more the OCO angle moves away from planarity, the more it means that the backdonation is strong and therefore the basic sites are strong. [85-87]

The change of geometry of the CO_2 molecule after adsorption is the most effective method to evaluate the strength of the basic sites if carbonate-like surface species are formed; indeed, the adsorption energy of CO_2 not only considers the interaction between the basic site and CO_2, but also depends on the interaction of CO_2 with other nearby atoms; therefore, it is not an optimal parameter to evaluate the strength of basic sites.

As in the case of the study of the acid sites, the adsorption of CO_2 on two vertexes and two edges was studied for both crystalline phases of zirconia. Figure 37 shows the structures with the strongest basic sites and Table 7 shows the values of the geometric parameters of CO_2 adsorption.

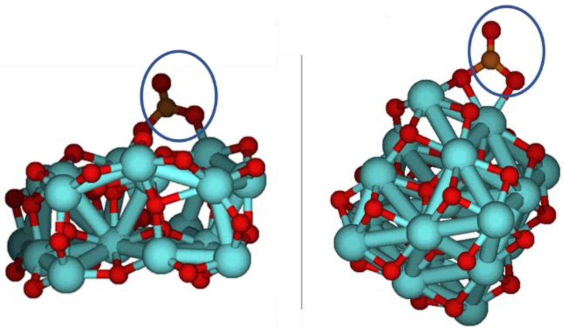

Figure 38. Adsorption of CO_2 on *m*-ZrO_2 (left) $Zr_{18}O_{33}$ and *t*-ZrO_2 $Zr_{19}O_{32}$ (right) clusters.

Table 7. CO_2 angle and bonds on monoclinic and tetragonal $Zr_{19}O_{32}$ sites on monoclinic $Zr_{18}O_{33}$ and tetragonal clusters after optimization.

Model	Type site	O-C-O angle(°)	C-O bond (1) (Å)	C-O bond (2) (Å)
Monoclinic	vertex	129	1.33	1.20
	edge	127	1.34	1.20
	edge	122	1.38	1.22
Tetragonal	vertex	143	1.25	1.18
	vertex	137	1.27	1.19
	vertex	132	1.30	1.20

In particular, from the results obtained, it was observed that in the case of *t*-ZrO_2 the carbonates tend to form preferentially on vertex-type sites, while for *m*-ZrO_2 they form both on vertex and edge sites. In general, it can be seen that CO_2 tends to bend more on the sites of the *m*-ZrO_2, in particular the edges, compared to *t*-ZrO_2, with angles ranging from 122 to 129° and from 132 to 143° for the monoclinic and the tetragonal respectively. Furthermore, the length of the C-O bond (1) appears to be greater in the case of CO_2 adsorbed on the monoclinic, with a length closer to that of the single bond, with values from 1.33 to 1.38 Å, compared to 1.25 to 1.30 Å in the case of tetragonal. In particular, we see that for *m*-ZrO_2 the strongest site is an edge, where CO_2 adsorbs with an OCO angle of 122° and where a C-O bond stretches up to 1.38 Å.

These results agree with the TPD-CO_2 experimental data, since they confirm a greater strength of the basic sites in the case of *m*-ZrO_2 compared to *t*-ZrO_2.

2.4.1.4.5 Study of AL adsorption and catalyst deactivation

In order to better understand the causes of the faster deactivation of *m*-ZrO_2 in the CTH reaction of ML to GVL compared to *t*-ZrO_2, we focused on the study of α-AL adsorption. From the literature it is known that AL tends to oligomerize easily, both in the presence of strong basic sites and strong acids.[89-90].

In the study of AL adsorption, adsorption via the oxygen of the carbonyl group was found to be the favoured one. According to the mechanism proposed by Chen and coworkers [88], thanks to the activation of the carbonyl on the Lewis acid sites, AL can polymerize in the presence of a nucleophile (such as an alkoxide) according to a ring-opening polymerization mechanism. For these reasons, we focused on the study of this molecule to better understand the causes of the faster deactivation of *m*-ZrO_2 in the reaction under examination.

The calculated adsorption energies are shown in Table 8, while Figure 39 shows the most stable structures respectively on edge and vertex sites of the two crystalline phases.

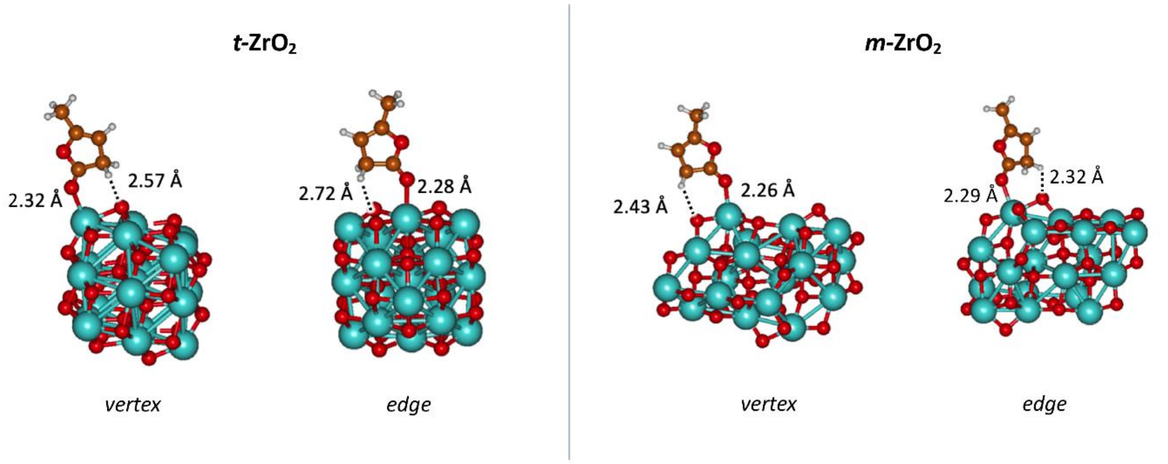

Figure 39. Adsorption of α-AL on $Zr_{19}O_{32}$ *t*-ZrO_2 (left) and $Zr_{18}O_{33}$ *m*-ZrO_2 (right) on the most stable adsorption sites for both the vertex- and edge-type sites. Zr-O(α-AL) distance (red stick) and H_α-O(ZrO_2) distance (black dotted lines) are reported in Å.

Table 8. Energy of adsorption of AL of different sites of monoclinic $Zr_{18}O_{33}$ and tetragonal O-terminated $Zr_{19}O_{32}$ clusters after optimization at DFT level.

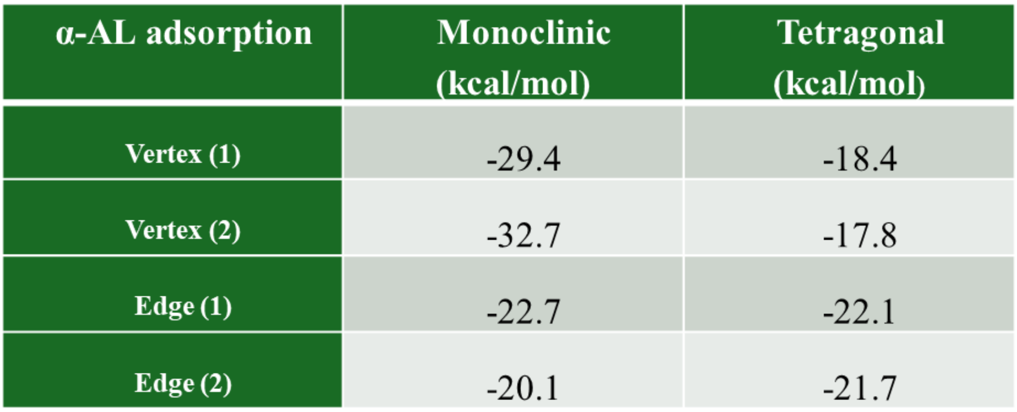

α-AL adsorption	Monoclinic (kcal/mol)	Tetragonal (kcal/mol)
Vertex (1)	-29.4	-18.4
Vertex (2)	-32.7	-17.8
Edge (1)	-22.7	-22.1
Edge (2)	-20.1	-21.7

In the case of *m*-ZrO_2, the adsorption energy includes a wide range, from -20.1 kcal/mol to -32.7 kcal/mol. In the case of *t*-ZrO_2 energy range goes from -17.8 kcal/mol to -22.1 kcal/mol. However, comparing the adsorption energies for the edge sites, which as it has been said previously appear to be the most representative of the real synthesized materials, the adsorption for the two phases is almost equal, with a value of -22.7 kcal/mol and -22.1 kcal/mol for monoclinic and tetragonal, respectively, for the most stable structures. This result appears to agree with the NMR study, where a similar interaction of AL with the surface of the two catalysts was observed. In fact, since these are the most representative sites of the sites present in real structures, and therefore present in greater numbers, they appear to be those highlighted by the NMR experimental analysis. As regards the vertex sites, representative of the possible defects present on the surfaces of the catalysts and the sites considered more reactive, a great difference can be seen in the adsorption energies, with -32.7 kcal/mol and -18.4 kcal/mol for *m*-ZrO_2 and *t*-ZrO_2, respectively, for the most stable structures. On the vertex, and therefore on the most reactive sites, AL tends to adsorb much more strongly on *m*-ZrO_2 than on *t*-ZrO_2, with a difference of -14.3 kcal/mol. Since the number of these sites is smaller, the average adsorption energy value of the AL on the two phases should not be affected significantly considerably by these sites. However, the Zr vertex, although in smaller numbers, being undercoordinated, are the most reactive and can trigger the deactivation mechanism. The greater interaction between the Zr and the O of the AL in the case of *m*-ZrO_2 leads to a longer residence time of the AL on the catalyst surface, and consequently to a greater probability that polymerization reactions take place, thus leading to a faster deactivation of the catalyst.

For this mechanism to occur, the geometry of adsorption is fundamental: in fact, it is necessary that an acid site close to the Zirconium vertex in question, an oxygen in this case, is able to remove an acid hydrogen from the AL, probably the one in alpha at the carbonyl (Hα), following a base-assisted dimerization/polymerization process [88-90]. For this reaction to take place, the distance between the acidic Hα and the O of the zirconia in question is therefore fundamental: the smaller the distance, the easier it will be for oxygen to deprotonate the AL, which will thus undergo a possible ring-opening polymerization. From Figure 38, one can see that the Hα-O distance is much shorter in monoclinic zirconia (with values of 2.32 and 2.43 Å) than in tetragonal (values of 2.57 and 2.72 Å).This has to be mainly ascribed to the different exposition of surface oxygens on the two phases and to the adsorption mode of α-AL via the carbonyl oxygen, which directs the C-Hα bonds towards the surface basic sites. Notably, the difference in H_α-*O(Zr*O_2*)* distance between the two phases is more evident for the (more numerous) edge surface sites (ca. 0.40 Å) than for the vertices (ca. 0.14 Å). This outcome strongly suggests that the acidic H_α are closer to the basic surface sites on the *m*-ZrO_2 than on the *t*-ZrO_2. These results, combined with the different strength of the basic sites described above, clearly indicate that the formation of oligomers and consequent deactivation of the catalyst is more likely on *m*-ZrO_2 than *t*-ZrO_2.

2.4.2 Effect of surface area in the CTH of ML: tetragonal zirconia

2.4.2.1 High surface tetragonal zirconia: synthesis and characterization

The evaluate the effect of surface area on the CTH of ML, a tetragonal zirconia with higher surface area have been synthesized. The procedure is the same reported for 120 m^2/g t-ZrO_2, but in this case the digestion time was increased from 24 h to 48h. The obtained zirconia was characterized with BET and XRD analysis.

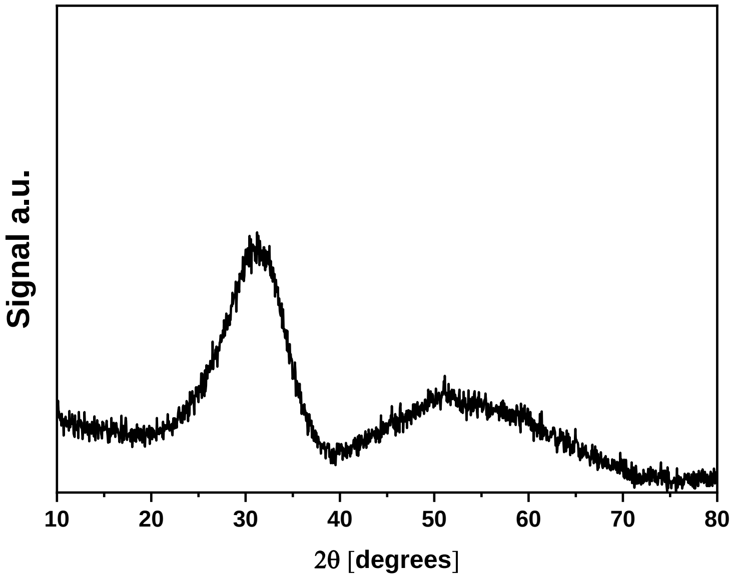

Figure 40. XRD pattern on *t*-ZrO_2 with high surface area

As can be seen from the spectrum obtained in Figure 40, it is not possible to trace a specific crystalline pattern, unlike that of zirconia 120 m^2/g, which is highly crystalline.

2.4.2.2 High surface tetragonal zirconia: catalytic tests

This zirconia has been tested for the CTH in optimized conditions. The catalytic results, in comparison with those using 120 m^2/g *t*-ZrO_2, are reported in the previous paragraph.

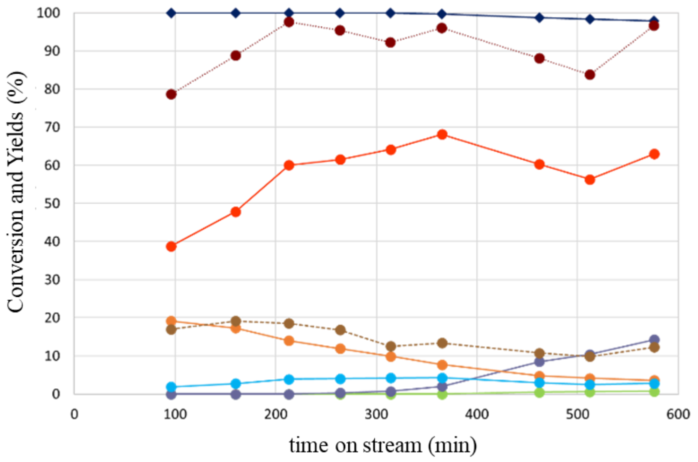

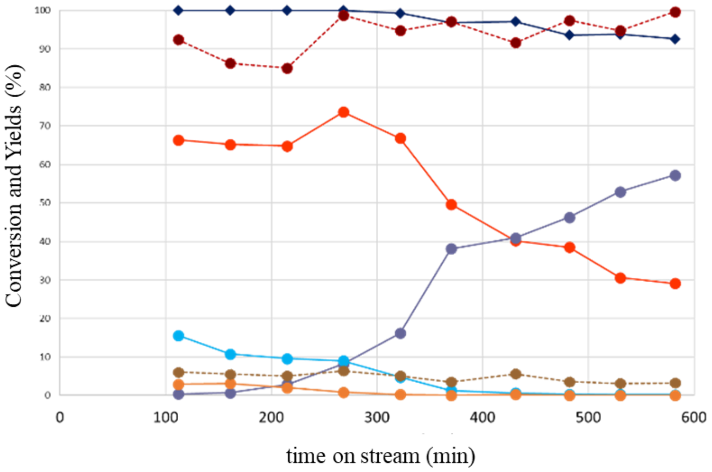

Figure 41. Catalytic results obtained in ML reduction via CTH using EtOH as H-donor over *t*-ZrO_2 with high surface area of 250 m^2/g (up) and 120 m^2/g *t*-ZrO_2 (down). Reaction conditions: ML:EtOH = 1:10 (molar ratio), T = 250 °C, τ = 1 s, % mol N_2:ML:EtOH = 90.1:0.9:9. Conversion (◆); EL (●); GVL (●); Ethyl GVL (●); aAL (●); bAL (●) EP (●);Others (●); Yield sum/Conversion (●)

As we can see from Figure 41, higher surface zirconia shows better catalytic performance for the CTH of ML, in comparison with the same catalyst but with a lower surface area. Indeed, we can see that the conversion remains total until 350 min, decreasing slightly in the next hours but still remaining over the 98%. The yield of GVL remain at high values (around the 57-69%) between the 200 and the 600 min of reaction, with a maximum of 69% at 350 min. In particular, in comparison with the lower surface area *t*-ZrO_2 (where we manage to reach a yield of GVL of 73%, we see that the selectivity to the production of GVL is slightly lower, but it remains more constant in the time, thanks to a less evident disactivation of the catalyst. Indeed, as said before, the conversion decreases just slightly; moreover, we can see a production of EL in the last hours of reaction, but it is much lower than lower area zirconia. This makes us understand that the catalyst tends to deactivate more slowly, probably thanks to the presence of a greater number of catalytic sites, which consequently become poisoned more slowly. Furthermore, it is important to note that using a catalyst with a higher surface area results in a greater production of Ethyl Pentenoates and byproducts, probably due to the greater number of catalytic sites which tend to push the process towards reactions consecutive to the production of GVL.

2.4.3 Zirconia materials for the CTH of ML to consecutive products of GVL: Pentenoate and Pentanoate

In addition to GVL, other industrially interesting products can be obtained from the CTH of ML process. In fact, by pushing the reaction towards consecutive reactions to the formation of GVL, Pentenoates can be obtained, through a ring-opening process and subsequent dehydration (as previously reported in the reaction mechanism). Through a subsequent reduction of the double bond it is possible to obtain Pentanoates: the latter, in particular, are very interesting products because they are used in the food and cosmetic flavouring industry. For this reason, we decided to study new catalytic systems, focusing on some parameters, such as the surface area and strength of Lewis acid and basic sites, in order to promote the CTH reaction further.

2.4.3.1 Synthesis and characterization of materials

A screening of different materials, both commercial and not, in the CTH reaction of methyl levulinate (ML) in a continuous gas phase system has been carried out. In particular, the commercial ones were provided by MelChemicals and are an amorphous zirconia, ZrO_2 Melcat XZ01521, and a Zirconia with the addition of WO_3 at 16 wt%, the W-ZrO_2 Melcat XZ01251. A mixed oxide, $ZrSi_{30}$ synthesized by the research group of Milan in the SCITEC-CNR Unit was also provided.

Synthesis of $ZrSi_{30}$

The zirconia–silica supports were prepared by a sol–gel procedure by the SCITEC-CNR group of Nicola Scotti. First, zirconyl chloride ($ZrOCl_2$), 30% solution in HCl (13 mL), was diluted to 100 mL with deionized water; such solution was then added dropwise at room temperature to 200 mL of an aqueous solution of ammonia at pH of 12 to obtain hydrous zirconia. A solution of tetraethyl orthosilicate : 2-propanol : water (1 : 6 : 2 molar ratio, respectively) was added to hydrous zirconia and the suspension was vigorously stirred for 3 days at 75 °C. The so obtained solid was thoroughly washed with deionized water until pH neutral, followed by drying overnight at 110 °C in air. Finally, the solid was calcined at 350 °C for 4 h in air.

Characterization of samples

First of all, we proceeded with a characterization of the materials. In particular, as for the study of the two crystalline phases of zirconia, the focus was on the surface area and strength of the acidic and basic sites. We then proceeded by carrying out a BET type analysis and a TPD-NH_3 and TPD-CO_2 study. The results obtained are reported in Table 9 (where they are also compared to the results for tetragonal and monoclinic zirconia).

Table 9. Summary of TPD analysis of different zirconia catalysts, both commercial and synthesized.

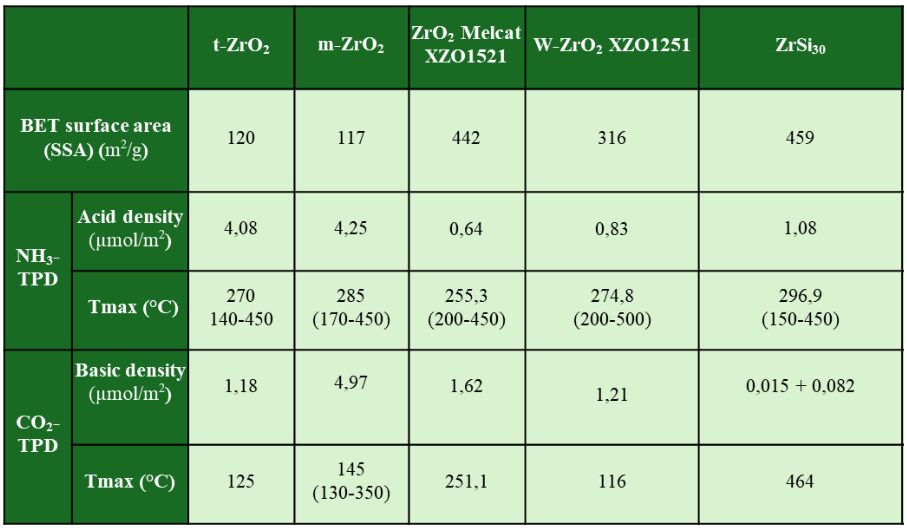

		t-ZrO_2	m-ZrO_2	ZrO_2 Melcat XZO1521	W-ZrO_2 XZO1251	$ZrSi_{30}$
BET surface area (SSA) (m^2/g)		120	117	442	316	459
NH_3-TPD	**Acid density ($\mu mol/m^2$)**	4,08	4,25	0,64	0,83	1,08
	Tmax (°C)	270 140-450	285 (170-450)	255,3 (200-450)	274,8 (200-500)	296,9 (150-450)
CO_2-TPD	**Basic density ($\mu mol/m^2$)**	1,18	4,97	1,62	1,21	0,015 + 0,082
	Tmax (°C)	125	145 (130-350)	251,1	116	464

As can be seen from the table 9, the commercial samples of zirconia had a much higher surface area than the crystalline ones synthesized in the laboratory. In particular, the mixed oxide $ZrSi_{30}$ had the highest surface area. Regarding the acid sites, all the samples of zirconia had a much lower density of acid sites (over 4 times) than the tetragonal and monoclinic crystalline ZrO_2. In particular, Melcat ZrO_2 XZ01521 was the one with the lowest density of acid sites, followed by W-ZrO_2 XZ01251 zirconia and finally by the mixed oxide $ZrSi_{30}$. The presence of silicium, in fact, makes the zirconia more acidic.

As regards the basic sites, we see that the mixed oxide $ZrSi_{30}$ was the one with the lowest density of basic sites, followed by W-ZrO_2 (with a value similar to tetragonal zirconia) and finally by Melcat.

XRD analysis have been performed on the three zirconia supports. The results are reported in Figure 42. The three materials have an amorphous crystalline structure.

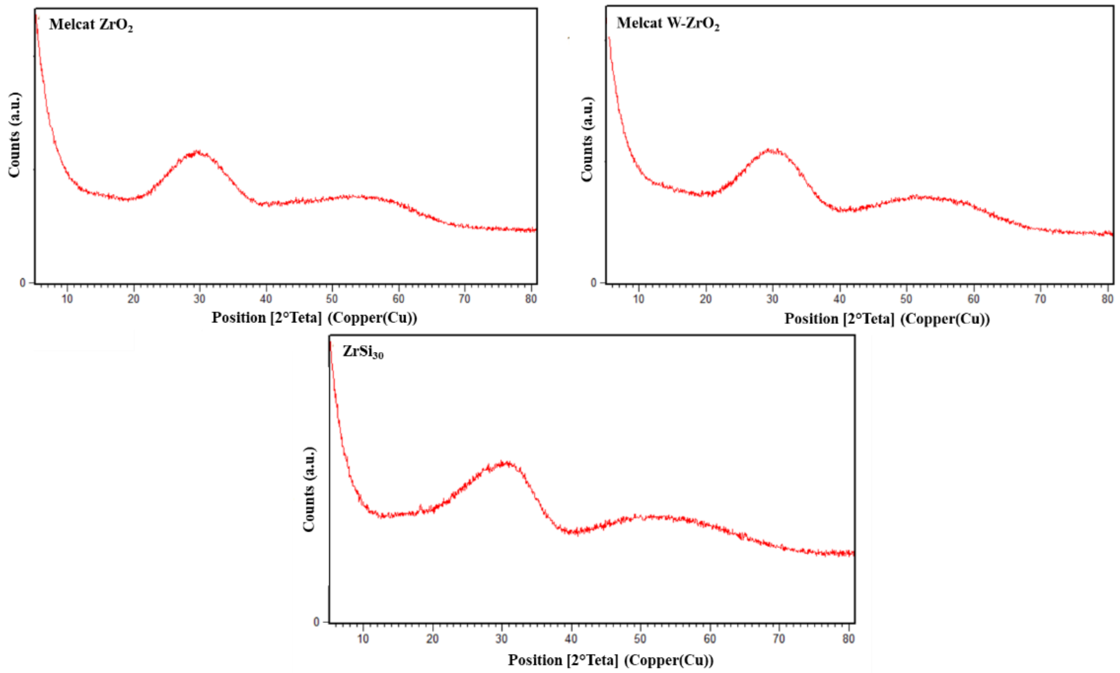

Figure 42. XRD patterns of Melcat ZrO_2, W-ZrO_2 and $ZrSi_{30}$.

2.4.3.2 Catalytic tests in CTH of ML

A screening of different materials, both commercial and not, in the CTH reaction of methyl levulinate (ML) in a continuous gas phase system has been carried out. The materials and reaction conditions are reported in the Table 10. The results have been compared with the catalytic results obtained previously using *t*-ZrO_2 and *m*-ZrO_2 in the same reaction conditions.

Table 10. Summary of catalytic tests using different materials for CTH of ML.

Catalyst	Alcohol	T(°C)	Contact time (sec)	% mol N_2:ML:EtOH	ML:EtOH (molar ratio)
ZrO_2 Melcat XZ01521*	Ethanol	250	1	90.1:0.9:9	1:10
W-ZrO_2 Melcat XZ01251*	Ethanol	250	1	90.1:0.9:9	1:10
$ZrSi_{30}$	Ethanol	250	1	90.1:0.9:9	1:10
ZrO_2 Melcat XZ01521*	Ethanol	250	1	89.5:0.5:10	1:20
W-ZrO_2 Melcat XZ01251*	Ethanol	250	1	89.5:0.5:10	1:20
$ZrSi_{30}$	Ethanol	250	1	89.5:0.5:10	1:20

***Commercial catalysts provided by MelChemicals.**
W-ZrO_2 Melcat XZ01251 contains 16%wt of WO_3
$ZrSi_{30}$ prepared by sol-gel

2.4.3.2.1 Catalytic test in standard conditions

ZrO_2 Melcat XZ01521

The catalytic results of the reaction using the amorphous commercial ZrO_2 Melcat XZ01521 are shown in Figure 43.

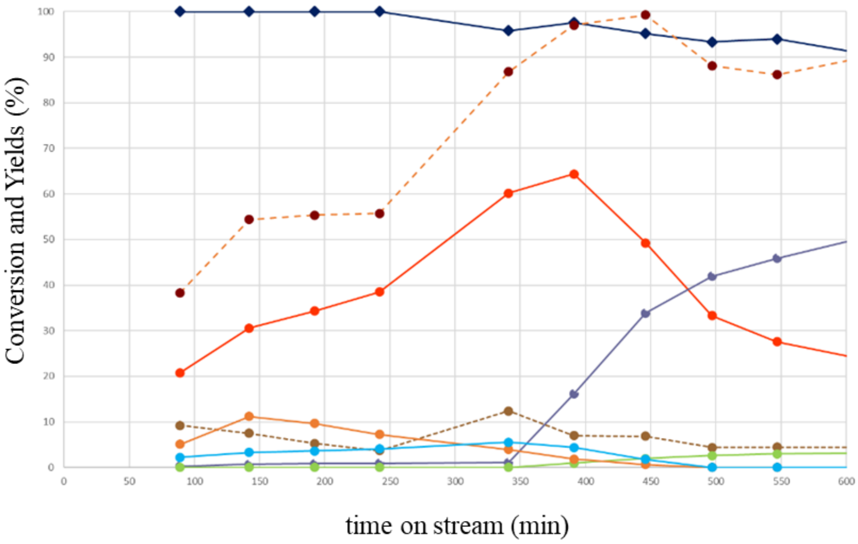

Figure 43. Catalytic results obtained in ML reduction via CTH using EtOH as H-donor over ZrO_2 Melcat XZ01521. Reaction conditions: ML:EtOH = 1:10 (molar ratio), T = 250 °C, τ = 1 s, % mol N_2:ML:EtOH = 90.1:0.9:9. Conversion (◆); EL (●); GVL (●); Ethyl GVL (●); aAL (●); bAL (●) EP (●); Methyl Pentenoate (●); Others (●); Yield sum/Conversion (●).

In the first hours of reaction, up to about 250 minutes of reaction, the conversion of ML was almost total. However, we have observed that the carbon balance of the reactants, Yields sum/Conversion, was very low. It tended to stabilize only after about 6 hours of reaction, stabilizing in the second day of reaction, after having switched off the flow of reactants and the heating and having left only an inert flow of N_2 all night long. The cause of this may be due to the high area of the catalyst (442 m^2/g), which could lead to a strong adsorption of the reaction reactants, saturating some catalytic sites. A good ɣ-Valerolactone (GVL) yield (64%) was achieved, however lower than *t*-ZrO_2. However, at 400 min of stream, the chemoselectivity in GVL rapidly decreased, increasing that in Ethyl Levulinate (EL), indicating that the catalyst was deactivating as seen in the case of crystalline zirconia. In the first hours of the reaction, there was a selectivity towards the production of EP of around 7-10%, which however decreased over the course of the reaction.

W-ZrO_2 Melcat XZ01251

In Figure 44 the catalytic results using W-ZrO_2 Melcat XZ01251 are reported.

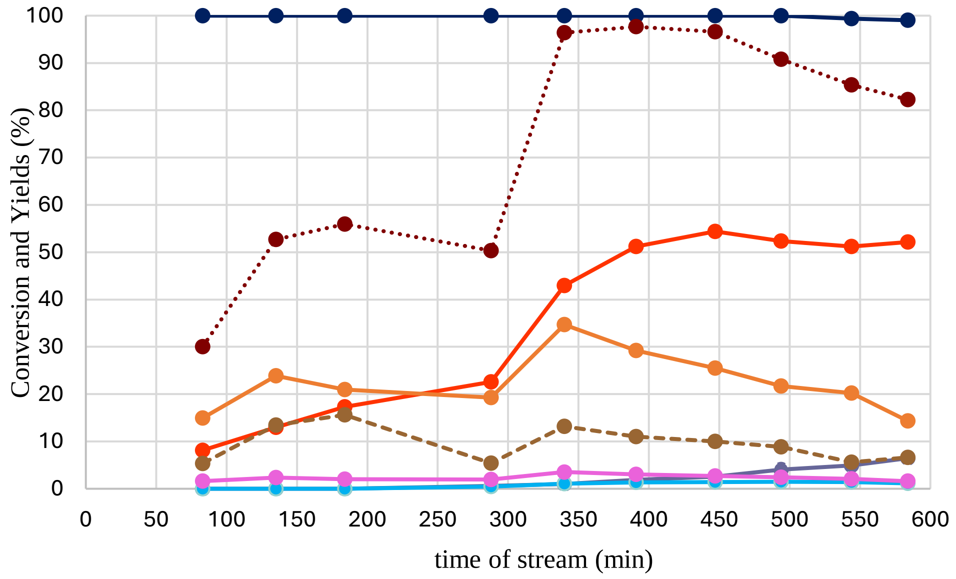

Figure 44. Catalytic results obtained in ML reduction via CTH using EtOH as H-donor over W-ZrO_2 Melcat XZ01251. Reaction conditions: ML:EtOH = 1:10 (molar ratio), T = 250 °C, τ = 1 s, % mol N_2:ML:EtOH = 90.1:0.9:9. Conversion (◆); EL (●); GVL (●); Ethyl GVL (●); aAL (●); bAL (●) EP (●); Methyl Pentenoate (●); Others (●); Yield sum/Conversion (●).

Once more, we see a low carbon balance for the first few hours of reaction, which improved on the second day of reaction. The reasons could be the same as previously discussed for the amorphous ZrO_2. For W-ZrO_2, from 400 to 600 min there was a stable yield in GVL around 51-54%; moreover, there was a good selectivity in Ethyl Pentenoates (EP), with a yield that reached 35% around 340 min. However, in the last hours of reaction the selectivity in EP decreased and the begin of a variation in chemoselectivity towards the EL can be observed, an indication that the catalyst was deactivating.

$ZrSi_{30}$

The catalytic results using $ZrSi_{30}$ under standard conditions are shown in Figure 45.

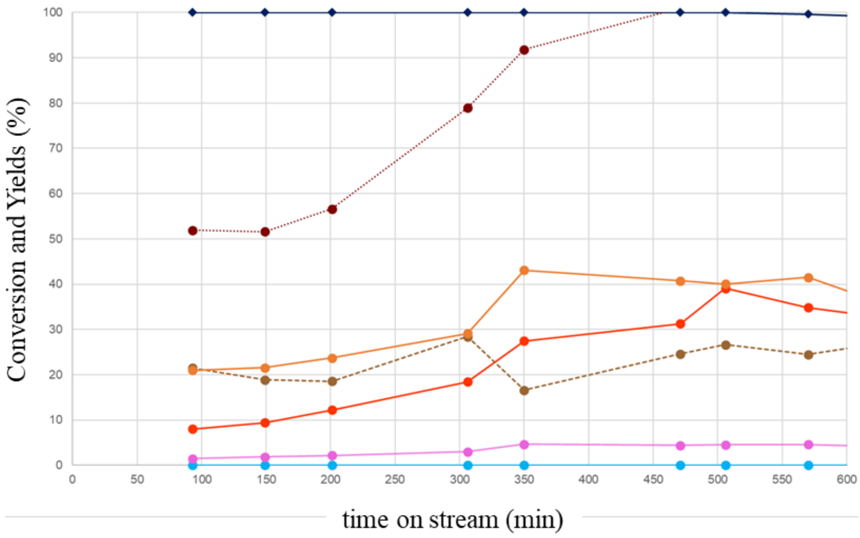

Figure 45. Catalytic results obtained in ML reduction via CTH using EtOH as H-donor over $ZrSi_{30}$. Reaction conditions: ML:EtOH = 1:20 (molar ratio), T = 250 °C, τ = 1 s, % mol N_2:ML:EtOH = 90.1:0.45:9. Conversion (◆); EL (●); GVL (●); Ethyl GVL (●); aAL (●); bAL (●) EP (●); ML (●); Others (●); Yield sum/Conversion (●).

Also in this case we see a low carbon balance in the first hours of the reaction, which improved on the second day of the reaction. In this case we have observed a good selectivity towards the formation of EP, higher than that of GVL, with selectivity reaching about 40-42% in the last hours of the reaction (between 350 and 600 min). The yield of GVL increased over reaction time in parallel with the yield of EP. The mixed zirconia silica oxide appears to favour reactions consecutive to the GVL, such as the formation of EP.

This material can be very interesting to favour the production of Pentenoates or be exploited to promote the reaction to the formation of Pentanoates. However, the formation of pentanoates was not seen, probably due to the fact that the double bond of the Pentenoates is too far from the catalytic surface, and therefore fails to be further hydrogenated with these types of catalyst.

2.4.3.2.2 Catalytic test in dilute conditions

For these catalysts it was decided to carry out a study in more diluted reaction conditions, in order to keep the surface of the catalyst cleaner to push it to consecutive products. In particular, we focused on a ratio ML:EtOH=1:20 compared to the classical conditions 1:10. The results obtained are reported below.

ZrO_2 Melcat XZ01521

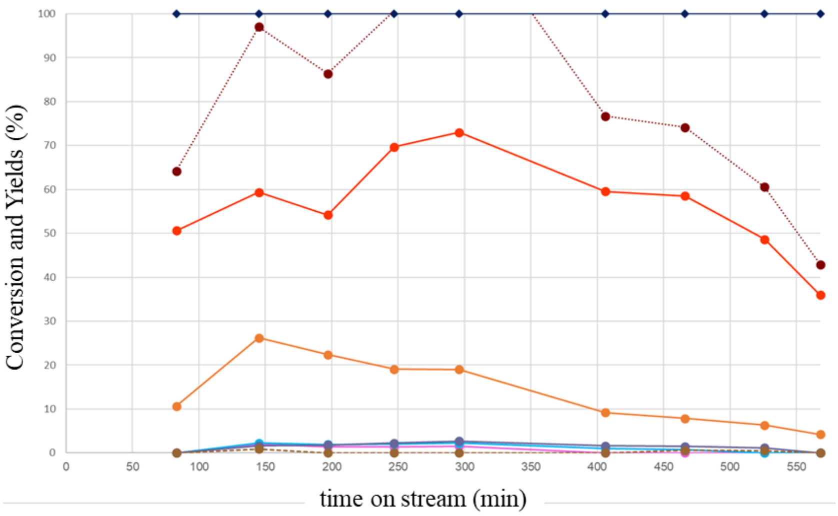

Figure 46. Catalytic results obtained in ML reduction via CTH using EtOH as H-donor over ZrO_2 Melcat XZ01521. Reaction conditions: ML:EtOH = 1:20 (molar ratio), T = 250 °C, τ = 1 s, % mol N_2:ML:EtOH = 90.1:0.45:9. Conversion (◆); EL (●); GVL (●); Ethyl GVL (●); aAL (●); bAL (●) EP (●); Methyl Pentenoate (●); Ethyl Eptenoate (●); Others (●); Yield sum/Conversion (●).

Looking at the results of the reaction using Melcat zirconia XZ01521 in dilute conditions (ML:EtOH=1:20 molar ratio), we see (Figure 46) that the reaction was able to reach full speed in much shorter times: in fact, the carbon balance was already good after 150 min of reaction. The conversion of ML remained total throughout the reaction. The reaction was very selective, with minimal yields of by-products and with GVL and EP as main products: in particular, in dilute conditions the selectivity towards the formation of GVL increased, reaching a maximum of 73%, then subsequently decreasing in the following hours of reaction. The selectivity towards the EPs reached a maximum of 27% at 145 min, then decreasing in the following hours of reaction. From this trend it can be deduced that the catalyst was deactivating during the last hours of the reaction, as can also be deduced from the low carbon balance, indicating the possible formation of light or heavy products adsorbed on the surface of the catalyst, which can block the reactive sites and therefore decrease the catalytic activity.

W-ZrO$_2$ Melcat XZ01251

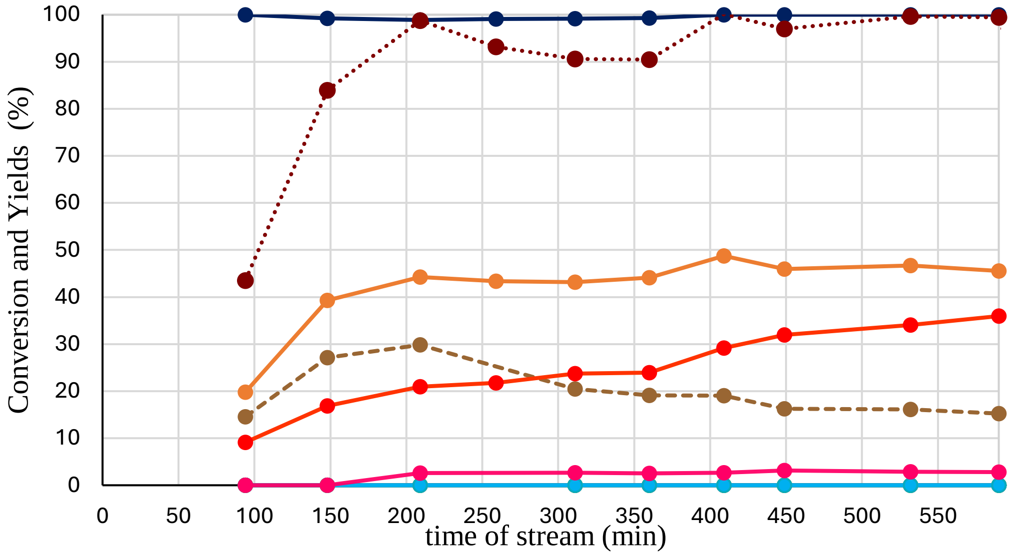

Figure 47. Catalytic results obtained in ML reduction via CTH using EtOH as H-donor over W-ZrO$_2$ Melcat XZ01251. Reaction conditions: ML:EtOH = 1:20 (molar ratio), T = 250 °C, τ = 1 s, % mol N$_2$:ML:EtOH = 90.1:0.45:9. Conversion (◆); EL (●); GVL (●); Ethyl GVL (●); aAL (●); bAL (●) EP (●); ML (●); Others (●); Yield sum/Conversion (●).

Figure 47 shows the results for the CTH reaction in diluted conditions using W-ZrO$_2$ XZ01251 as catalyst. Also in this case the diluted conditions allowed to reach better carbon balances already at short reaction times. Furthermore, we see that in diluted conditions the selectivity is shifted towards the formation of EPs, with a selectivity of around 40-48% from 150 min to 590 min of reaction. The selectivity towards the formation of GVL increased during the reaction, reaching values around 36% at 590 min of reaction.

ZrSi$_{30}$

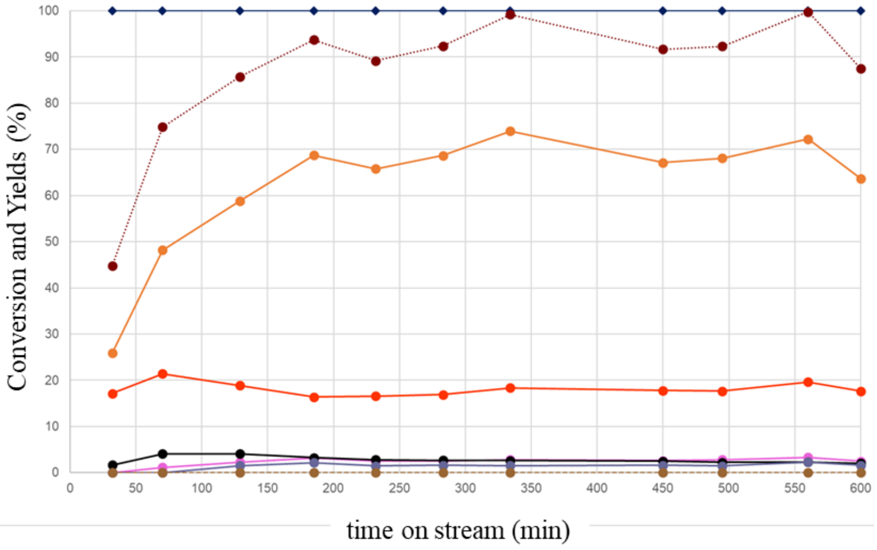

Figure 48. Catalytic results obtained in ML reduction via CTH using EtOH as H-donor over ZrSi$_{30}$. Reaction conditions: ML:EtOH = 1:20 (molar ratio), T = 250 °C, τ = 1 s, % mol N_2:ML:EtOH = 90.1:0.45:9. Conversion (◆); EL (●); GVL (●); Ethyl GVL (●); aAL (●); bAL (●) EP (●); ML (●); Others (●); Ethyl Pentanoate (●); Ethyl Eptenoate (●); Yield sum/Conversion (●)

Also in this case, in diluted conditions, as can be seen from Figure 48, the conversion of ML was total throughout the reaction, which was very selective, with GVL and EP as the main products. In particular we see the selectivity of the reaction profoundly shifted towards the formation of EP, with yields reaching 73% around 335 min, and still maintaining yield values between 68 and 73% from 185 min to 600 min; consequently, the yield of GVL was lower, with yield values around 18-21% throughout the reaction. The yield of both GVL and EP remained almost constant throughout the reaction; in fact, no deactivation phenomena were seen after ten hours of reaction: the catalyst continued to maintain the same catalytic performance. Among the various by-products it is important to note a minimal formation of ethyl pentanoates, the hydrogenated products of EP, but in any case with yields always lower than 5%, probably due to the fact that the double bond to be hydrogenated was too far from the surface of the catalyst to be hydrogenated. However, since this material is particularly interesting both for its stability and good selectivity towards the formation of EP, subsequent studies depositing small percentages of palladium were carried out, in order to promote the reaction towards the formation of Ethyl pentanoates.

In conclusion, from this screening of materials in two different conditions, normal and diluted, it was concluded that ZrSi$_{30}$ zirconia is the most interesting catalyst to obtain EP: in fact, it is particularly selective towards the formation of these products. Furthermore, since these materials had very high surface areas, in the first hours of the reaction the system struggled to reach full speed, since due to the high surface area the reaction reagents tended to adsorb strongly on the surface of the catalyst, blocking the catalytic sites and lowering the carbon budget. To obtain a stable system already from the first hours of reaction with a good carbon balance it was necessary to work in more diluted reaction conditions, in this case with a ratio ML:EtOH=1:20, which also seems to drive the selectivity of reaction even further towards the formation of EP.

2.5 Conclusions and future work

Several zirconia-based catalysts, both commercial and synthesized, have been tested in the CTH reaction of methyl levulinate to GVL or consecutive products (pentenoates) using alcohols as H-donor. In particular, the reaction was carried out in a continuous gas phase reactor at atmospheric pressure.

Two crystalline zirconias with similar surface areas, tetragonal and monoclinic zirconia, have been successfully synthesized and characterized for the GVL hydrogenation reaction. These were tested in the reaction under investigation, optimizing the reaction parameters. In particular, a general greater activity of *t*-ZrO_2 was seen in the reaction in question compared to *m*-ZrO_2. In order to better understand the causes of the different activity of the two crystalline phases, different methodologies were combined: study of the reaction through time-on-line analysis; characterization of the pre- and post-reaction catalysts; study of deactivation phenomena using NMR spectroscopy and computational calculations. In particular, for these studies we focused on the reaction using ethanol as H-donor.

The results obtained show a better efficiency of *t*-ZrO_2 in adsorbing and activating ethanol, favoring the CTH reactive mechanism and at the same time limiting the adsorption of the AL reaction intermediate on the catalytic surface, which tends to polymerize forming carbonaceous products heavy particles that adsorb on the catalytic surface, deactivating the catalyst. At the same time, *m*-ZrO_2, resulting from having stronger basic sites both from TPD experimental and computational studies, has a greater interaction with AL, therefore favoring AL polymerization reactions in shorter times and therefore deactivating earlier.

A high surface area *t*-ZrO_2 was synthesized to compare with the low surface area one: it showed better catalytic performance compared to low area zirconia, maintaining an almost total

conversion up to 350 min of reaction, decreasing slightly in the following hours to values around 98% conversion. However, the yield in GVL results to be slightly lower, with values from 57 to 69%, compared to low-area tetragonal zirconia (maximum yield 73%), due to a lower selectivity towards the formation of GVL for high area *t*-ZrO_2, probably due to a greater number of reactive sites which favor the consecutive reactions of formation of Ethyl Pentenoates and ByProducts.
Starting from these last results, we decided to test other zirconia-based materials, both commercial and not, for the reaction of CTH of ML. In particular, we decided to push the reduction to consecutive reaction in order to obtain Pentenoates products through a ring-opening process of GVL and subsequent dehydration. All the catalysts result to have high surface area, with values form 316 m^2/g to 459 m^2/g. The catalysts were tested in CTH reaction of ML with two ML:EtOH molar ratio, 1:10 and 1:20. $ZrSi_{30}$ results to be the best catalysts to obtain Ethyl Pentenoates (EP). In particular, with molar ratio ML:EtOH 1:20, in the conditions studied the conversion of ML was total throughout the reaction, which the catalyst was very selective, with a yield in EP that reached 73% around 335 min, and still remained between 68 and 73% from 185 min to 600 min; consequently, the yield of GVL was lower (18-21%) throughout the reaction. The catalysts remain active for all the ten hours of reaction, with the same catalytic activity.

Future work: deposition of small % of Pd on Zirconia catalysts: effect in CTH of ML

As seen in the previous paragraphs, $ZrSi_{30}$ appeared to be an excellent catalyst to obtain EP from ML with CTH mechanism in diluted experimental conditions (1:20 molar ration ML: EtOH). In particular, the catalyst remained stable over time (over the 10 hours of reaction) and the selectivity in EP remained constant. In order to drive the reaction to the next step, *i.e.* the formation of Ethyl Pentanoates by hydrogenating the double bond of the EPs, it was decided to proceed by depositing a small quantity of Pd using the sol-immobilization technique, according to the synthetic method reported in Chapter 2.3.1.3. In particular, $ZrSi_{30}$ was loaded with 0.5% wt of Pd. In order to reduce completely Pd in the metallic state, the catalyst was pretreated before the reaction with a flow of H_2 in N_2 (10 mol% H_2) for 2 h at 350 °C. The reaction was subsequently proceeded under classical conditions, with a ratio ML:EtOH=1:20. The catalytic results obtained are shown in Figure 49.

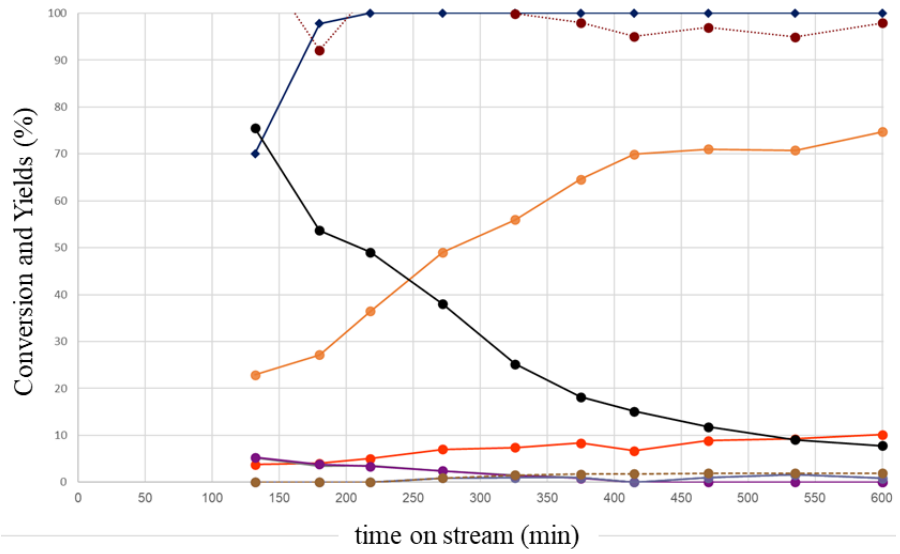

Figure 49. Catalytic results obtained in ML reduction via CTH using EtOH as H-donor over Pd-ZrSi$_{30}$, Pd 0.5 % wt with H2 prepratment. Reaction conditions: ML:EtOH = 1:20 (molar ratio), T = 250 °C, τ = 1 s, % mol N$_2$:ML:EtOH = 90.1:0.45:9. Conversion (◆); EL (●); GVL (●); Ethyl GVL (●); aAL (●); bAL (●) EP (●); ML (●); Others (●); Ethyl Pentanoate (●); Ethyl Heptenoate (●); Ethyl Heptanoate (●); Methyl Pentanoate (●); Yield sum/Conversion (●).

As can be seen from 170 minutes onwards the system was fully operational, with complete conversion of the ML for the entire duration of the reaction and good carbon balance. In the first hours of the reaction there was good selectivity in the formation of Ethyl Pentanoates, with a selectivity of 76% at 170 min, which however decreased drastically immediately afterwards, reaching a minimum value of 8% at 600 min. In parallel with the decrease in selectivity for the Ethyl Pentanoates, there was an increase in the selectivity in the formation of the Ethyl Pentenoates, which increased from 23% at 170 min of reaction to 75% at 600 min of reaction. These two trends are complementary to each other and suggest that the deactivation of the catalyst is selective at the Pd sites, which acts on the hydrogenation of the double bond of the Ethyl Pentenates. Regardingthe activity of the ZrSi$_{30}$ support, this did not appear to decrease during the reaction, as confirmed by the increase in the yield of Ethyl pentenoates. This phenomenon may be due to the fact that during the reaction the Pd tends to reoxidize partially to PdO and therefore to deactivate. Consequently, a simple pretreatment with H_2 did not appear to be sufficient to keep Pd active for the production of Ethyl Pentanoates.

It was therefore decided to test the reaction in the same experimental conditions, but this time using a 20% H_2 flow for the entire duration of the reaction which allows the Pd to be kept in the metallic state during reaction and cleaned. The catalytic results obtained are shown in Figure 50.

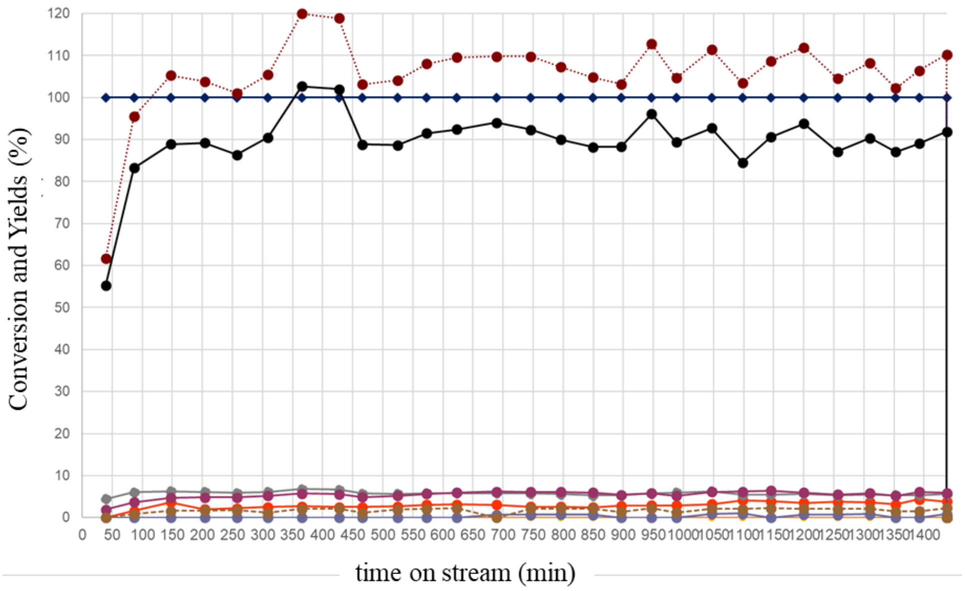

Figure 50. Catalytic results obtained in ML reduction via CTH using EtOH as H-donor over Pd-ZrSi$_{30}$, Pd 0.5 % wt with H$_2$ prepratment. Reaction conditions: ML:EtOH = 1:20 (molar ratio), T = 250 °C, τ = 1 s, % mol N$_2$:ML:EtOH = 90.1:0.45:9, 20% H2. Conversion (◆); EL (●); GVL (●); Ethyl GVL (●); aAL (●); bAL (●) EP (●); ML (●); Others (●); Ethyl Pentanoate (●); Ethyl Heptenoate (●); Ethyl Heptanoate (●); Methyl Pentanoate (●); Yield sum/Conversion (●)

The reaction was continued for 24h, in order to see if the catalytic activity remained stable even for a whole day.

As can be seen from the results obtained, there was a selectivity ranging from 87 to 99% in Ethyl Pentanoates for the entire duration of the reaction. There was a small yield of Methyl Pentanoates with values around 6-7% for the entire duration of the reaction and 5-6% of Ethyl Heptanoates. The system was therefore very selective towards the desired product. Furthermore, it was stable even after 24 hours of reaction, without altering its catalytic performance.

The results obtained appear particularly promising and interesting for the formation of Ethyl Pentanoates.

In order to better understand the structure of the synthesized catalyst, characterizations such as TEM analysis to study the dispersion of the nanoparticles and their distribution are necessary; furthermore, both a pre- and post-reaction XPS analysis is necessary in order to understand the oxidation state of Palladium, whether in a metallic state or in the form of an oxide. Starting from these results it is possible to further optimize the synthesis of the catalyst, varying the quantity of palladium, the ratio between the stabilizing agent and the metal and the type of the stabilizing agent, evaluating the effects of these parameters on the structure of the catalyst and its reactivity for the reaction in question. Furthermore, the optimization of reaction parameters, such as temperature, contact time, alcohol/substrate ratio etc. are necessary in order to increase the selectivity of the reaction. Studies of the reaction mechanism of hydrogenation of the double bond by Palladium can be carried out both through experimental tests and theoretical studies.

3. Liquid phase hydrogenation of furfural

3.1 Introduction

3.1.1 Furfural

Furfural (furan-2-carboxaldehyde) is a colourless viscous liquid with a pleasant almond smell, which tends to darken when exposed to air, with boiling point of 160 °C. It can be produced by dehydration of pentoses, and, thanks to his versatility, it has been included among the top value-added chemicals obtainable starting from lignocellulosic biomass [15,91]. This process can happen in one- or two-step process: in the one-step process, pentose sugars are hydrolysed to xylose and dehydrated to furfural at the same time; in the two-step process, on the other hand, due to the milder conditions, the hydrolysis to xylose takes place first, which is then subsequently dehydrated to furfural, obtaining a greater quantity of furfural than in the one-step process [92]. In these processes methanol and acetic acid can be obtained as by-products. At an industrial level, a process of acid hydrolysis of pentose polysaccharides takes place, which are obtained from the fraction of fibrous residues of wood waste from food crops or from non-food crops.

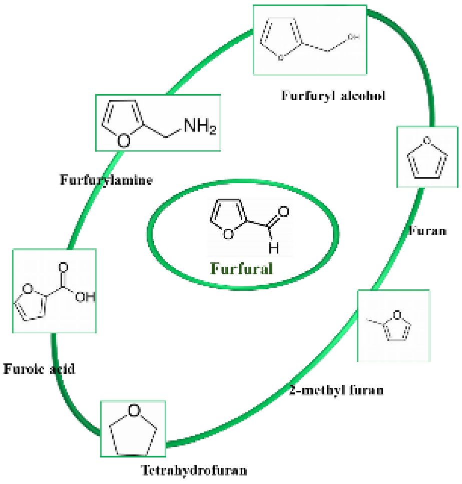

Figure 51. Furfural and its derivatives.

Furfural and its derivatives (Figure 51) are interesting from an industrial point of view thanks to their countless applications, for example in the field of plastics, agrochemistry and pharmaceuticals [93]. Due to the presence of the aldehyde group and the furan ring, furfural is an interesting selective and reactive solvent [94-96]. It is used for the extraction of aromatics from lubricating oils and to produce phenolic resins. It is also soluble in ethanol, ethers and water.

Furfural is used for the synthesis of biopolymers [97], allowing to obtain polymers starting from biological raw materials. In particular, it allows to obtain polyesters and polyethylene furanoate (PEF), which is a green alternative to polyethylene tereftalate (PET) that can be used to make bottles. Furthermore, the polymeric derivatives of furfural are used to produce electronic products, in the packaging and automotive sectors.

3.1.2 Hydrogenation of furfural: furfuryl alcohol and its applications

Among its derivatives of particular interest is furfuryl alcohol (FA). Indeed, it can be used for the production of resins [97,98] to produce abrasive wheels, automotive products and for some aircraft components; it is also used to toughen and harden soft woods, making them suitable for indoor and outdoor applications. In the aerospace field, FA is used to protect some parts of the shuttles, in particular the nose and the attachment of the wings, from the extreme temperatures (both low and high) found in space, improving their mechanical properties [99].

The hydrogenation mechanism of furfural is complex as it leads to a large variety of possible products; consequently, having a good selectivity towards the desired product and a high catalytic activity has always been the central point in the search for a catalyst for this reaction. In particular, several transition metals have been tested, such as Ru [100] , Pt [101], Co [102], Cu [103] etc. in both monometallic and bimetallic form. In particular, it has been seen that both the type of metal and the size of the nanoparticles influence the selectivity [104] and the activity of the catalyst. This is because a different nanoparticle size leads to a different number of available active sites and therefore can affect activity and selectivity of products. Medlin et Al. [105] studied in a tubular bed flow reactor the effect of particle size and controlling the nature and number of active sites on Pd/Al_2O_3 catalysts by covering the reactive sites with different blocking agents, in particular: thiolate self-assembled monolayers (SAMs), i.e., 1-octadecanethiol (C18), benzene-1 ,2-dithiol (BDT); the reactions were performed at 190°C with a H_2:furfural= 25:1 molar ratio and a quantity of catalyst varied every time to have a conversion around 13±2% for every reaction. It has been seen that BDT favors selectivity towards the products FA and 2-methylfurfural (total selectivity greater than 70%), unlike C-18 where the total selectivity of the two is 35%.

3.1.3 Hydrogenation of furfural using MPV mechanism

The reduction of furfural, as already highlighted for the reduction of levulinic acid derivatives, can be performed both using molecular hydrogen or and H-donor molecule, as an alcohol. MPV reduction has been reported as an efficient method for the reduction of carbonyl compounds under mild conditions using heterogeneous catalysts with Lewis acid and basic sites and secondary alcohols as reducing agents [106]. Among these, zirconia works as an excellent catalyst for this type of reaction for the same reasons seen previously for the reduction of levulinic acid [107]. Shen and coworkers [108] hypothesized a reaction mechanism for the MPV reduction of furfural.

Following the MPV mechanism (Figure 52), the carbonyl group of furfural is reduced to alcoholic group, obtaining furfuryl alcohol (FA); from the reaction of FA with a large excess of isopropanol, catalysed by Brönsted and Lewis acid sites, there is the formation of 2-(isopropoxy)methyl furan (IPF). From the alcoholysis of IPF, catalysed by Brönsted acid sites, isopropyl levulinate is formed. Acetalization of the furfural can take place as competitive reaction to the reduction of furfural to FA, leading to the formation of furfural diisopropyl acetal (FDIA).

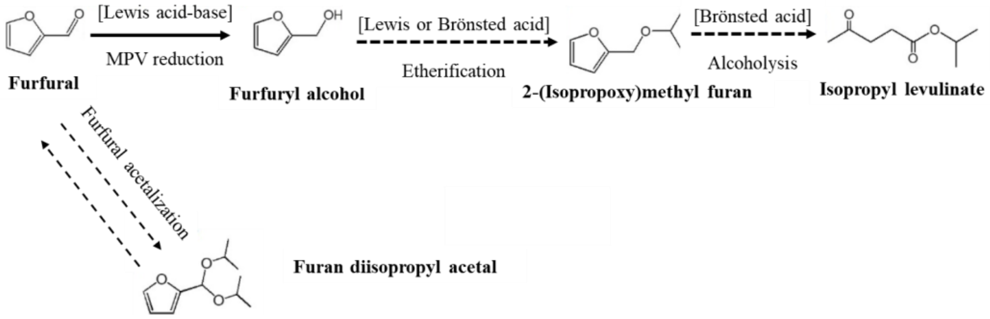

Figure 52. MPV mechanism of hydrogenation of furfural.

In particular, Shen and coworkers [108] reported the CTH of furfural to furfuryl alcohol using a Mesoporous Zr-Containing Hybrids as catalyst using isopropanol as alcohol in an autoclave reactor of 30 mL of capacity. They manage to reach excellent result at 110°C with a yield of FA up to 97.8% for 4 h of reaction. Instead, at higher temperature (130 and 150°C), they saw a reduction in FA selectivity, which was mainly attributed to the occurrence of side reactions.

3.1.4 Bimetallic nanoparticles: structure and synthesis

In the last few years, particular interest in the world of nanostructured catalytic material synthesis has been taken by bimetallic catalysts. [109]. In fact, compared to their monometallic counterparts, they appear to have improved chemical and physical properties in the catalytic field, thanks to the presence of different functionalities and properties focusing on electronic and geometrical properties and therefore greater activity, stability and ability to tune the selectivity in a range of reactions. Furthermore, bimetallic catalysts show good stability [110-114].

According to the synthesis conditions and the types of metals, different structures of bimetallic NP catalysts can be obtained, consequently showing different catalytic activity.

In Liu's work [115] the main structures are reported for bimetallic catalysts (see Figure 53).

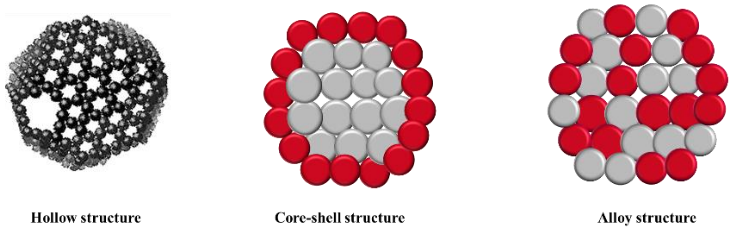

Figure 53. Principal bimetallic nanoparticles structures.

Crown-jewel

In this method the atoms of one metal, generally the most precious, are individually positioned in specific positions of another metal. With this method it is therefore possible to use a small quantity of the more expensive metal, which however being on the surface of the cheaper one will be able to interact with the substrate favouring the reaction and will lower the cost of the catalyst; moreover, since the single atoms are surrounded by atoms of the less expensive metal, the latter will modify the electronic structure of the more expensive metal, giving it new catalytic properties. The synthesis of these types of catalysts is very complex, and the mainly used technique is chemical vapor deposition (CVD), as carried out by Sykes [116].

Hollow nanostructures

This type of structure consists of a hollow structure that can contain other multifunctional materials or acts as a real "reactor", encapsulating the reaction substrates inside. In general, this method has the advantage of reducing costs due to lower quantity of the used materials. One of the synthetic approaches to obtain this type of bimetallic materials is the sacrificial approach, where a metal in nanoparticle form is used as a sacrificial model, generating hollow bimetallic structures thanks to galvanic substitution: this substitution occurs when a metal in the form of nanoparticle is in contact with ions of another metal which have a higher reduction potential

[117-119]. However, these synthetic methods are very complex and expensive, lowering their scale-up possibilities, which is one of the most important challenges to overcome.

Core-shell

Core-shell structures are among those that have shown the greatest interest in the catalytic field. In this structure, one of the two metals, generally the cheaper and less reactive, is positioned in the whole part of the nanoparticle, acting as a core, while the other forms an external shell, which will therefore be the exposed one that will interact with the substrate. The advantage of this method is that it allows to reduce costs by using a cheaper metal for the internal core, which is generally not always the reactive one. Furthermore, the interaction between the two different metals can greatly influence their catalytic capacities. The synthesis of this type of catalyst can take place by first reducing the metal that will have to act as a "core" in the form of nanoparticles and, subsequently, reducing the more expensive metal that will be deposited on the core metal, which will have had the function of seed for the reduction. It is also possible to obtain a core-shell catalyst with a one pot synthesis, by adding the two metal precursors simultaneously. In this case, the metal with the lowest reduction potential will reduce first, thus acting as a reduction seed for the other metal, which will reduce around the first, forming the core-shell structure [120-123].

Alloy structure

Alloy-like structures are made up of two types of metals that are distributed homogeneously in nanoparticle form, forming alloys. In general, two metals with different reduction potentials tend to distribute themselves homogeneously, leading to the formation of a core-shell structure. To obtain an alloy-like structure it is necessary to strictly control the synthetic process. One method is to use firstly a strong reducing agent, such as $NaBH_4$, which allows the two metals to be reduced at the same time, although they have different reduction potentials, and consequently to form alloy structures. A good reducing agent for this purpose is $NaBH_4$, which was used by Xu and coworkers to reduce nanoparticles of Ni and Fe into an alloy structure [124]. Surfactants and counterions also affect synthesis. In fact, through a specific adsorption, it is possible to regulate the reduction potentials of the two metals, leading to their reduction at the same time, as was done by Han et Al., who obtained an Au-Pd alloy starting from $HAuCl_4$ and K_2PdCl_4 with ascorbic acid using cetyltrimethylammonium chloride as surfactant [125].

Sharma and coworkers [126] focused on Pd-Au bimetallic catalysts. In particular, it has been found that the formation of the bimetallic catalyst of Pd and Au can take place in three main ways: one of the two metals tends to migrate superficially forming an external monolayer; the formation of a bimetallic surface due to the mix of the two metals on the surface of the support; the migration of one of the two metals into the substrate forming an internal monolayer adjacent to the support.

It should be noted that the use of weaker reducing agents for Pd and Au precursors results in the formation of Au-core-Pd-shell structures because Au has a greater tendency to reduce following the Pd metal, whereas the use of strong reducing agents leads to an almost random distribution of Pd-Au bimetallic NPs. In the case of sequential reduction, firstly, the monometallic core is developed, and, in the second step, another metal shell has been mounted on that surface of the core; however, at higher temperatures, intrusion of the core metal into the shell metal occurs, leading to alloy formation. Thus, the method of synthesis, the choice of the stabilizing agents and of the reducing agents influence the formation of bimetallic NPs. Furthermore, the selection of the support and the choice of the heat-treatment method also plays a key role and it is sometimes the deciding factor for the entire catalyst preparation procedure.

3.2 Scope

The aim of this work was to synthesize catalytic systems based on both mono and bimetallic nanoparticles supported on a commercial zirconia using the sol-immobilization technique. The catalysts were tested in the CTH hydrogenation reaction of furfural to FA. In particular, the effect of the type of metal and the quantity of metal was evaluated in the case of monometallic catalysts, while for bimetallic catalysts the effect of the presence of the two metals and their molar ratio was evaluated. Among the various synthesized catalysts, the one with the best catalytic performance was selected, in order to characterize it and test it in an autoclave reactor optimizing the reaction parameters.

3.3 Experimental part

3.3.1 Furfural hydrogenation: synthesis of supported nanoparticles on different zirconia support

Catalysts based on metal nanoparticles supported on different types of commercial zirconia were synthesized and tested for the liquid phase hydrogenation of furfural.

3.3.2 Synthesis of supported nanoparticles on zirconia: sol-immobilization technique

The synthesis of monometallic catalysts supported on zirconia follows the same procedure as the sol-immobilization reported in paragraph 2.3.1.3. The list of catalysts obtained and tested is shown in Table 11.

Table 11. List of catalysts synthetized for furfural hydrogenation

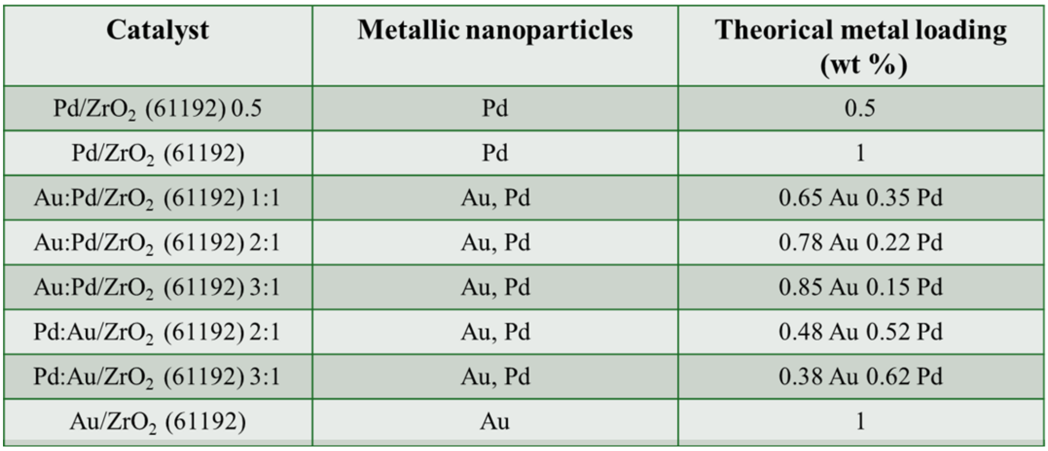

Catalyst	Metallic nanoparticles	Theorical metal loading (wt %)
Pd/ZrO_2 (61192) 0.5	Pd	0.5
Pd/ZrO_2 (61192)	Pd	1
Au:Pd/ZrO_2 (61192) 1:1	Au, Pd	0.65 Au 0.35 Pd
Au:Pd/ZrO_2 (61192) 2:1	Au, Pd	0.78 Au 0.22 Pd
Au:Pd/ZrO_2 (61192) 3:1	Au, Pd	0.85 Au 0.15 Pd
Pd:Au/ZrO_2 (61192) 2:1	Au, Pd	0.48 Au 0.52 Pd
Pd:Au/ZrO_2 (61192) 3:1	Au, Pd	0.38 Au 0.62 Pd
Au/ZrO_2 (61192)	Au	1

3.3.3 Synthesis of bimetallic supported nanoparticles

The same procedure of the synthesis of monometallic supported nanoparticles have been used to prepared bimetallic catalysts. In particular, the precursor of the two metals were mixed in about 400 mL of distilled water and stirred. The following steps turn out to be the same as for the synthesis of monometallic catalysts: 1.188 mL of a PVA aqueous solution previously prepared was added, keeping the solution stirred (PVA: metal = 1.2:1 weight ratio). After three minutes, the reducing agent $NaBH_4$ was added ($NaBH_4$: metal = 5:1 molar ratio); after 30 minutes, the support was added (0.99 g) and the solution was acidified with sulphuric acid under the isoelectric point of the support (pH=5). The solution was left under stirring overnight, then it was filtered and the catalyst was washed with distilled water (about 1 L) in order to remove the impurities, until the washing water had reached neutral pH. The catalyst was left to dry overnight at room temperature and subsequently dried in an oven for 4 hours at 150 ° C. The procedure is reported in Figure 54.

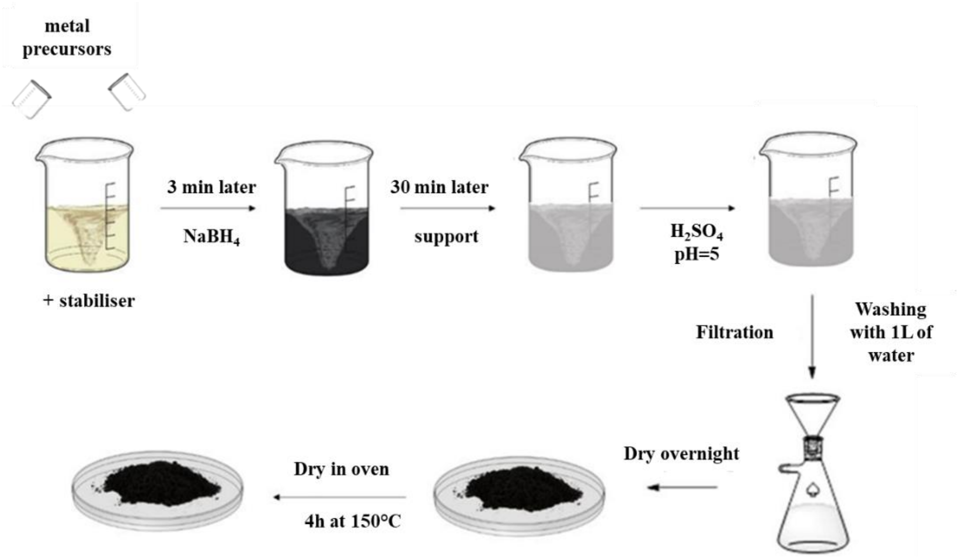

Figure 54. Synthesis of bimetallic nanoparticles using sol-immobilization technique.

3.3.4 Catalysts characterization

3.3.4.1 Characterization of supports

The supports, being different types of zirconia, were characterized in order to compare their properties according to the same techniques reported in chapter 2.3.2 for the characterization of monoclinic and tetragonal zirconia. In particular: BET analysis, XRD analysis, NH_3-CO_2-TPD analysis.

3.3.4.2 Characterization of supported nanoparticles

The supported nanoparticles have been characterized with different techniques, reported below, in order to understand: the effective loading of the metal on the support (%); the degree of dispersion and the size of the nanoparticles; the structure of bimetallic nanoparticles. All these factors, in fact, greatly influence the catalytic activity of a material.

X-ray fluorescence spectroscopy (XRF) is a non-destructive analysis technique that allows to know the elemental composition of a sample using X-ray fluorescence radiation, which is emitted by the atoms of the sample following an excitation, which can occur by irradiating the sample with X-rays and high-energy range. Measures were performed with the use of an energy dispersive micro-Xray Fluorescence spectrometer M4 TORNADO (Bruker). This instrument is equipped with 2 anodes a Rhodium X-ray tube 50 kV/600 mA (30 W) and a Tungsten X-Ray tube 50 kV/700 mA (35 W). For sample characterization, the X-rays Rhodium with a polycapillary lens enabling excitation of an area of 200 μm was used. The detector used was a Silicon-Drift-Detector Si(Li) with <145 eV resolution at 100000 cps (Mn Kα) and cooled with a Peltier cooling (253°K). The measurement was done under vacuum (20 mbar). The elements, that can be measured by this instrument unit range from sodium (Na) to uranium (U). Quantitative analysis was done using fundamental parameter (FP) (standardless). As elements are present in stoichiometric compounds, its formula was used for quantification of the weight percent of each element.

Transmission electron microscopy (TEM) analysis is an analytical technique that allows characterization with high resolution. In particular, in this work it has been used to evaluate the average size of the metal nanoparticles, particle size distribution and their dispersion on the support. In this technique, a beam of electrons generated by a tungsten filament is accelerated by an electrical potential (100-300 keV) and passed through a vacuum section and impinges on the sample. A part of these electrons is transmitted without undergoing interactions from the sample; this part is captured by a fluorescent screen which returns a real and magnified image of the sample. To have an accurate result, 300 to over 400 particles for sample have to be analysed.

Analysis was performed using a TEM / STEM FEI TECNAI F20 microscope at 200 keV. Samples were suspended in ethanol and treated by ultrasound for 15 min. A drop of the suspension was deposited on "quantifoil-carbon film" supported by a grid of Cu. The preparation was dried at 120 °C.

X-ray photoelectron spectroscopy (XPS) is an analytical technique that allows to obtain information on the surface composition of a sample, surface exposure of metals, oxidation state of the elements, contamination issues ad leaching of metal after reaction due to the high surface sensitivity. A beam of high energy photons irradiates the surface of the sample under analysis: the irradiation energy is greater than the binding energy of the electrons to the sample; as a result, the electrons leap off the sample with a kinetic energy equal to the photon's excess energy over the binding energy. From this kinetic energy it is possible to identify the atoms.

The XPS spectra were recorded with Axis ultra DLD Kratos spectrometer (Figure 55), fitted with an Electronics 80-365B multi-channel hemispherical electron analyser and an X-ray excitation source of Al Kα 1486.6 eV.

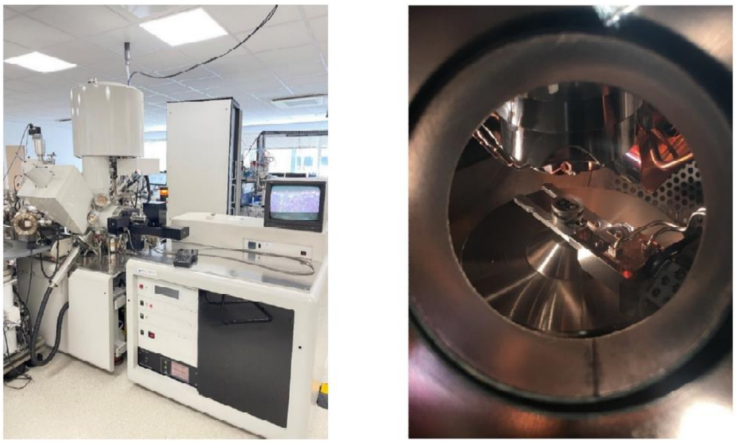

Figure 55. Axis ultra DLD Kratos spectrometer of University of Lille.

3.3.5 Hydrogenation of furfural in liquid phase

The H-transfer hydrogenation of furfural was carried out at the university of Lille, France, during a six-month period abroad during the PhD course. In particular, the screening of different catalysts was carried out in a Screening Pressure Reactor (SPR) (Figure 56): it is a multi-reactor composed of 24 mini batch reactors with a total capacity of 6mL where it is therefore possible to carry out 24 reactions in parallel while maintaining constant the reaction conditions such as temperature, agitation, pressure and time.

For each reactor, 10 mg of catalyst and 2 mL of solution of Furfural in isopropanol (Furfural:metal=250/ 500 molar ratio) were added. The reaction was carried out for two hours at T=130°C, stirring at 600 rpm and 20 bars of nitrogen. At the end of the reaction, the reactor was cooled to room temperature, the system was left to vent and finally the various post reactions were filtered with nylon filters with porosity 0.45 μm.

Figure 56. SPR pressure reactor from RealCat Lab and 24 reactor plate

After that, for the best catalysts, the time on line was performed in a stainless-steel Asynt autoclave (Figure 57). A solution of 10 mL of furfural in isopropanol was added into the reactor with 50 mg of catalyst (Furfural:metal=500 molar ratio). The reaction was performed at 130°C for 2 h, stirring 600 rpm and with a pressure of nitrogen of 20 bar. After two hours, the reactor was cooled down, the pressure was released and the post reaction was filtered with Teflon filters of 0.45 μm.

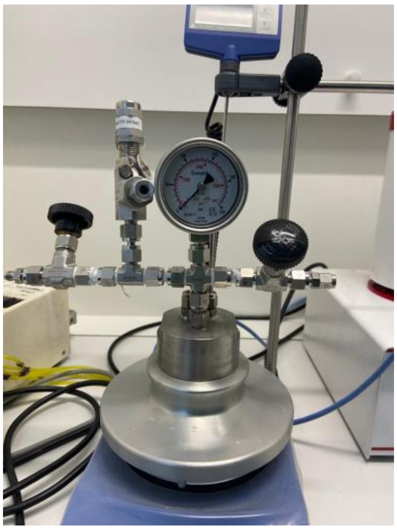

Figure 57. Asynt autoclave reactor

3.3.6 Analysis of post reactions

The post reaction was analysed using a gas chromatograph (equipped with a FID, flame ionization detector) coupled with a mass spectrometer (GC-MS) of the Agilent Technologies 7890B type. The column used is a CP-Wax 52 CB column. The response factors, $F_{product}$, were determined experimentally for the commercial compounds. The moles of each product were calculated according to the following equation:

$$mol_{product} = A_{product} * \ F_{product} * V_{final}(L)$$

Where *mol* indicates the moles of the product obtained; *A* is the area under the peak of the compound under investigation; *F* is the response factor of the compound; *V* is the final volume of the post reaction solution reported in litres. It was therefore possible to calculate the conversion (Y) of the starting reagent and the yield (X) and selectivity (S) of each product:

$$Y_{reagent} = \frac{mol_{initial\ reagent} - mol_{final\ reagent}}{mol_{initial\ reagent}} * 100$$

$$X_{product} = \frac{mol_{finalreagent}}{mol_{initial\ reagent}} * 100$$

$$S_{product} = \frac{X_{product}}{Y_{reagent}} * 100$$

3.4 Results

3.4.1 Catalytic transfer hydrogenation of Furfural, following the MPV mechanism

In this chapter the mainresults for the CTH of furfural are reported, following the MPV mehanism reported in paragrafh 3.1.3. In particular, the focus of this work was to screen different materials of supported nanoparticles, both mono and bimetallic using Au, Pd as metals, prepared using the sol-immobilization tecnique, testing them in the reaction in question. After that, the catalysts with the best catalytic performance have been selected for other test in an autoclave reactor, with the porpouse of optimizing various reaction parameters and to establish the relationship between the chemical and physical properties of the materials and catalytic activity.

3.4.2 Screening of materials in CTH of Furfural in liquid phase

Various materials have been synthesized using the sol-immobilization technique. They were tested in the CTH of Furfural. In particular, the materials tested are:

- The commercial ZrO_2 support (61192), in order to evaluate its catalytic performance as such and compare the results with those of the same support with deposited nanoparticles
- Palladium monometallic catalysts supported on ZrO_2(61192), with 0.5 wt.% and wt.1% palladium loading.
- Bimetallic catalysts on ZrO_2 (61192) with different atomic ratios, in particular Au-Pd and Pd-Pt.

The obtained catalysts were characterized by XRF analysis. The results obtained are reported in the Table 12:

Table 12: XRF analysis of synthesized mono and bimetallic catalysts

Catalyst	Au (% wt)	Pd (% wt)
Pd 0.5 wt /ZrO_2 (92)	-	0.58 ± 0.10
Au-Pd (1:1)/ ZrO_2 (92)	0.64 ± 0.10	0.33 ± 0.18
Au-Pd (2:1)/ ZrO_2 (92)	0.79 ± 0.18	0.20 ± 0.19
Au-Pd (3:1)/ ZrO_2 (92)	0.85 ± 0.12	0.14 ± 0.10
Au-Pd (1:2)/ ZrO_2 (92)	0.52 ± 0.18	0.57 ± 0.30
Au-Pd (1:3)/ ZrO_2 (92)	0.40 ± 0.20	0.64 ± 0.15
Pd/ ZrO_2 (92)	-	0.96 ± 0.15

In particular, the materials were tested in two reaction conditions by varying the furfural metal molar ratio at low and high molar ratio and using the following parameters:

- Furfural: Metal ratio=500 molar ratio
- Furfural: Metal ratio = 250 molar ratio

In particular, referring to the work of Shen and coworkers [118], we decided to remain in the temperature range between 80 and 150 °C, and in particular for the screening tests from a temperature of 130 °C. The reaction was carried out for two hours, in order to study the selectivities and yields at incomplete conversion. The results obtained are reported below in Figures 58 and 59.

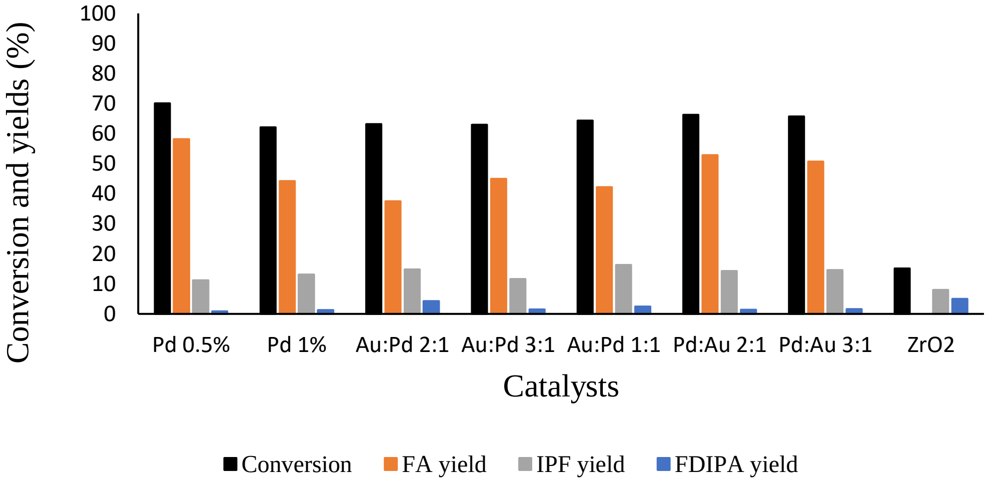

Figure 58. screening of catalyst in CTH reaction of furfural in SPR reactor. Conditions of reaction: PN_2: 20 bar; stirring: 600 rpm; T=130°C; t=2h; Furfural:metal=500 molar ratio; H-donor:isopropanol; Vtot: 2 mL for reactor; 0.010 gr of catalyst.

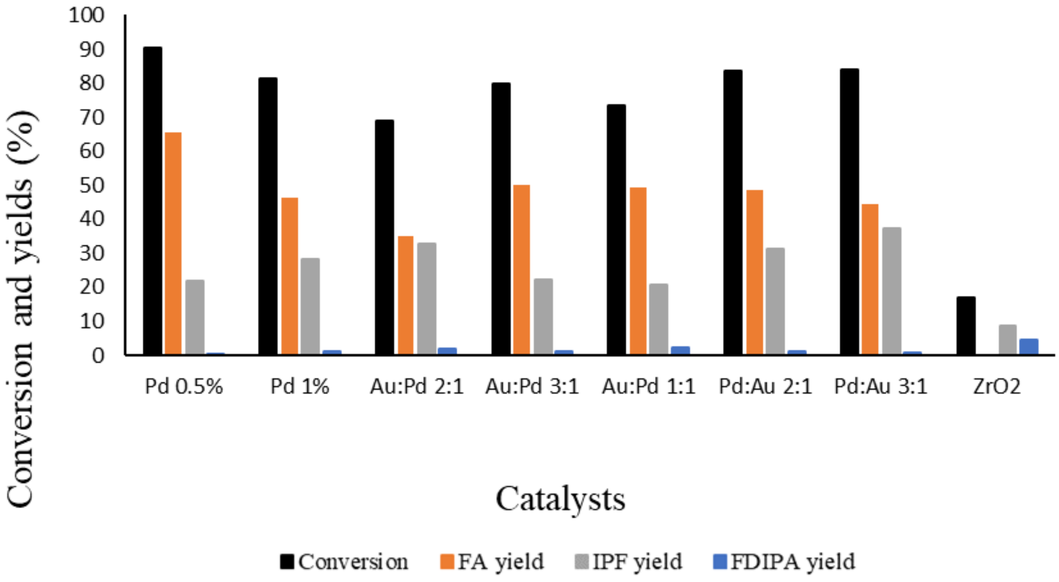

Figure 59. screening of catalyst in CTH reaction of furfural in SPR reactor. Conditions of reaction: PN_2: 20 bar; stirring: 600 rpm; T=130°C; t=2h; Furfural:metal=250 molar ratio; H-donor:isopropanol; Vtot: 2 mL for reactor; 0.010 gr of catalyst.

From the results obtained it can be deduced that zirconia alone was not active in the H-transfer reaction of furfural (FF) to Furfuryl alcohol (FA) at these mild reaction conditions. In fact, in both reaction conditions there was no formation of FA using only the support as a heterogeneous catalyst.

Focusing on the monometallic catalyst, the most selective for the formation of FA appears to be 0.5% Pd, with a yield of 58.1% for 500 molar ratio conditions and 65.1% for 250 molar ratio conditions; as the content of Pd increase we observed a decrease in conversion and a decrease in yield of FA. The bimetallic catalysts showed almost similar catalytic performances, with yields in FA ranging from 30.1 to 52.8% for furfural:metal=500 molar ratio and from 25.8 to 50.1% for furfural:metal=250 molar ratio.

In general, we can conclude that catalyst with the best catalytic performance is the 0.5% Pd, and in particular with a molar ratio FF:metal molar ratio of 250 the conversion (90%) and the yield of FA (%) is higher than for 500 molar ratio.

From the results obtained it can be deduced that the presence of Pd is fundamental for hydrogenating FF to FA, since Pd is well-known that it is a metal that facilitates hydrogenation reactions. However, a lower Pd loading leads to better catalytic results, with a higher selectivity in Furfuryl alcohol and with a higher conversion of Furfural. The causes of this can be attributed to the fact that, with a higher loading of Pd, the nanoparticles, being too close to each other, tend to sinter, leading to the formation of larger and therefore less active nanoparticles.

From the results obtained it was decided to optimize the reaction conditions in an autoclave reactor for the materials with the best catalytic performance, Pd 0.5% wt /ZrO_2 (61192).

3.4.3 CTH of Furfural in liquid phase: Pd 0.5 % wt as catalyst

3.4.3.1 Autoclave test: comparison between SPR reactor and autoclave reactor in catalytic activity

For the autoclave tests, we proceeded by testing the materials that gave the best catalytic performance in the SPR reactor, optimizing various reaction parameters. Since the autoclave is larger than the SPR reactors, in this scale up phase we proceeded by comparing the catalytic performances in the two reactors with the same reaction conditions (P_{N2}: 20 bar; stirring: 600 rpm; T=130°C; t=2h) using Pd 0.5 % wt /ZrO_2 (61192) as catalyst.

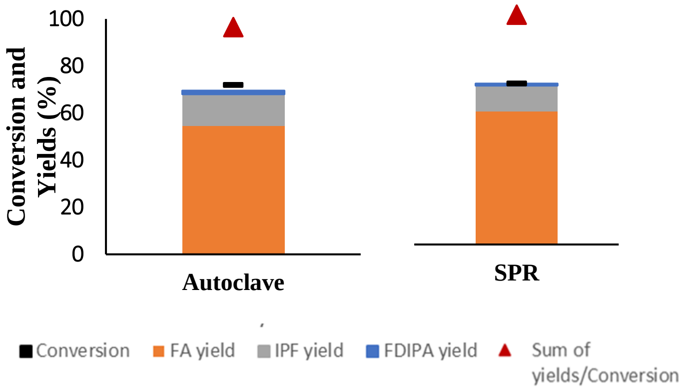

Figure 60. Comparison between catalytic tests in autoclave reactor and SPR reactor using Pd 0.5% wt /ZrO_2 (61192) as catalyst. Conditions of reaction: PN_2: 20 bar; stirring: 600 rpm; T=130°C; t=2h; Furfural:metal=500 molar ratio; H-donor:isopropanol; Vtot: 2 mL for SPR reactor, 10 mL for autoclave reactor; 0.05 gr of catalyst for autoclave reactor, 0.010 gr for SPR reactor.

As can be seen from Figure 60, the catalytic performances were very similar, with a FF conversion of around 72% for the autoclave test and 70% for the SPR reactor test and a FA yield of 55% in the autoclave and 58% in the SPR reactor. The error, within the experimental error range, confirms the possibility of using the SPR reactor as a starting point for screening tests, using the results obtained to then carry out further tests in the autoclave.

3.4.3.2 Optimization of reaction parameters

Different reaction parameters have been optimized to increase the activity of the catalyst at the selectivity to the desired product (Furfuryl alcohol). Optimization of the quantity of catalyst and stirring rate have been performed to evaluate to be in a kinetic regime. After that, other parameters have been optimized, as time, temperature and temperature of catalyst pretreatment.

Optimization of reaction parameters: Quantity of catalyst

We proceeded first by evaluating the effect of the catalyst mass while maintaining the same reaction conditions (130°C, PN_2= 20 bar, stirring rate 600 r.p.m., 2 h reaction time). The catalytic results are shown in Figure 61.

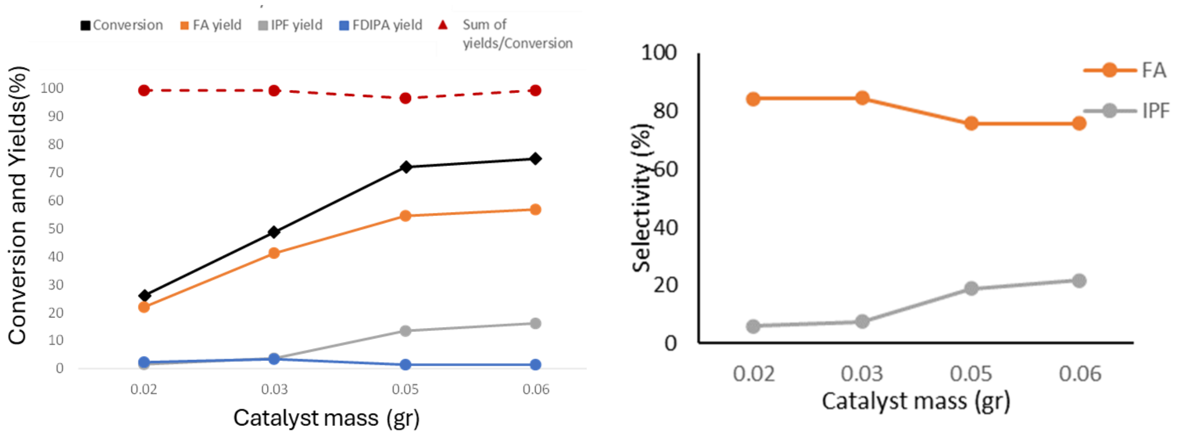

Figure 61. Effect of quantity of catalyst in CTH reaction of furfural using Pd 0.5% wt /ZrO_2 (61192). Conditions of reaction: PN_2: 20 bar; stirring: 600 rpm; T=130°C; t=2h; Furfural:metal=500 molar ratio; H-donor:isopropanol; Vtot: 10 mL; 0.02/0.02/0.05/0.06 gr of catalyst.

Increasing the mass of the catalyst up to 0.05 g resulted in a linear increase in FF conversion, indicating that there were no apparent diffusion limitations. By further increasing the catalyst mass up to 0.06 g, it is seen that the conversion tended to increase linearly no longer, indicating that limitations due to external diffusion phenomena were present, however a much lower conversion level could be used to verify these results. The main products were FA and 2-isopropoxymethylfuran (IPF). We see that for catalyst masses of 0.02 and 0.03 g the selectivity for FA was around 85%, while that in IPF was around 6-8%. As the mass of the catalyst increased, the selectivity for FA decreased as the selectivity towards IPF increased. It can be deduced that with a mass of 0.05 g of catalyst we are in a kinetic regime; consequently, since at this value there is also the highest conversion and the highest yield in FA, for subsequent experiments 0.05 g was used as the standard mass of the catalyst.

Optimization of reaction parameters: stirring rate

Subsequently, the effect of the stirring rate was investigated under the same reaction conditions (T=130°C, PN_2=20 bar). This parameter is fundamental as the reaction is carried out in an autoclave-type reactor in a three-phase system, where the catalyst is solid, the reagents are liquid and the inert gas N_2 has the task of maintaining the reagents in the liquid state. In order to maximize the interactions between the reagents and the catalytic surface, stirring plays a fundamental role. It is in fact fundamental to make sure you are in a kinetic regime. To do this it is necessary to evaluate whether there are any weaknesses to mass transfer (external diffusion). The results of the different stirrings are shown in Figure 62.

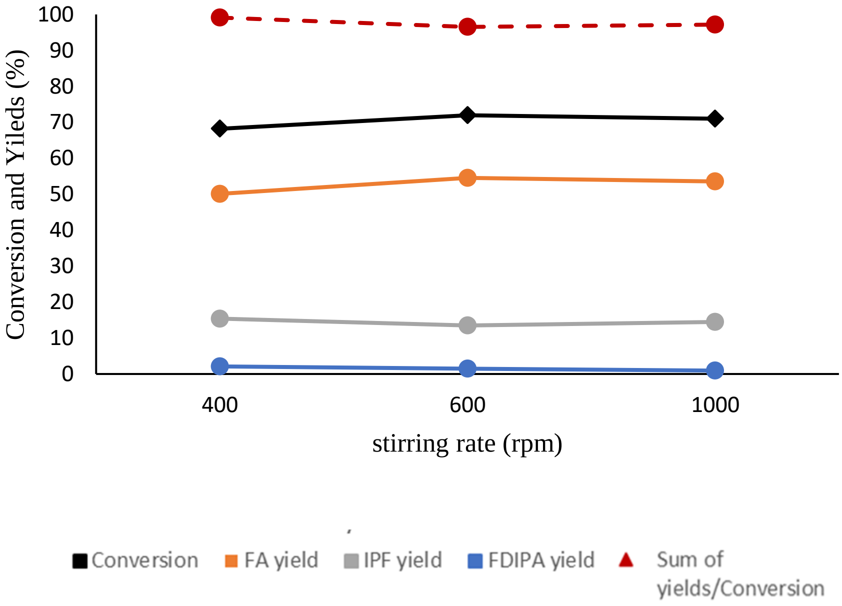

Figure 62. Effect of stirring in CTH reaction of furfural using Pd 0.5% wt /ZrO_2 (61192). Conditions of reaction: PN_2: 20 bar; stirring: 400-600-1000 rpm; T=130°C; t=2h; Furfural:metal=500 molar ratio; H-donor:isopropanol; Vtot: 10 mL; 0.05 gr of catalyst.

From the results obtained it can be seen that at 400 rpm there was the lowest FF conversion, with a value of 68% and a FA yield of 50%. At higher stirrings the conversion increases slightly, with a maximum at 600 rpm (72%) and a maximum FA yield of 55%. At 1000 rpm FF conversion is 71% with a FA yield of 53%. It can be concluded that an agitation of 600 rpm is the optimal one in the conditions of reactions reported to obtain FA, since in addition to being the most selective for the desired product it is also the one that leads to the least formation of by-products, such as IPF with a yield of 13% at 600 rpm compared to 15% at 400 and 1000 rpm. The results obtained also confirm that we are working in a kinetic regime, since yield and conversion do not increase further with increasing stirring.

Optimization of reaction parameters: Reaction Time effect

We proceed optimizing other reaction parameters, as time, studying the catalytic activity as a function of it. Specifically, 30 min, 60 min and 120 min reactions were conducted. The results obtained are shown in Figure 63.

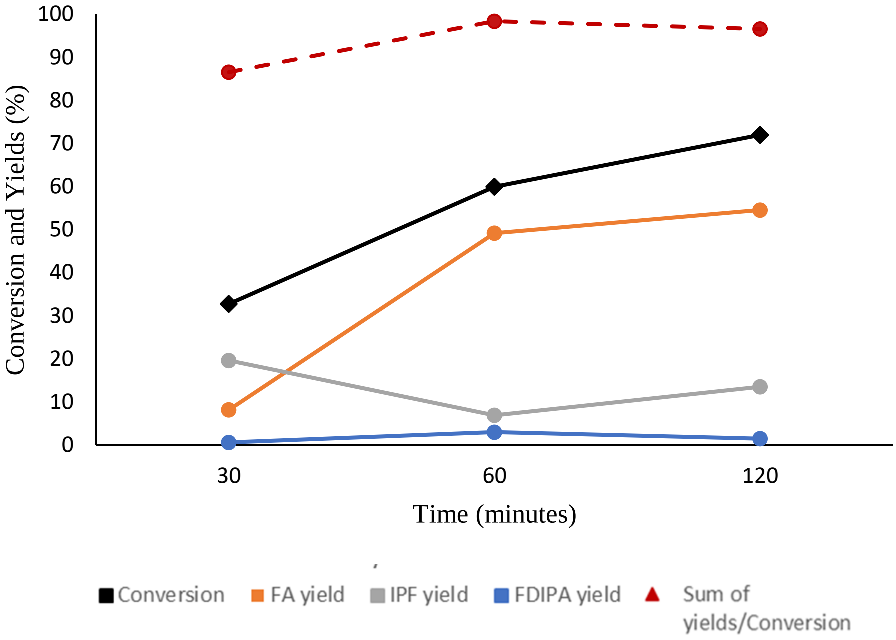

Figure 63. Effect of time in CTH reaction of furfural using Pd 0.5% wt /ZrO_2 (61192). Conditions of reaction: PN_2: 20 bar; stirring: 600 rpm; T=130°C; t=30 min/60min/120min; Furfural:metal=500 molar ratio; H-donor:isopropanol; Vtot: 10 mL; 0.05 gr of catalyst.

As time increased the conversion of furfural increased, reaching 72% at 120 min of reactions; in the mean time, the FA yield increased to 55% at 2 hours of reaction, to the detriment of that in IPF and FDIPA, which decreased, with values of 13% and 1 % respectively.

It was decided to focus on low reaction times, up to 2 hours, in order to have a low FF conversion and better evaluate the effect of the kinetics on the reaction under examination.

Optimization of reaction parameters: Effect of reaction temperature

Another parameter that plays a fundamental role in catalysis is the reaction temperature. Figure 64 shows the results of catalytic tests at different reaction temperatures, keeping other reaction parameters unchanged. For these tests we proceeded using the quantity of catalyst (0.05 g) and stirring (600 rpm) based on our previous optimization.

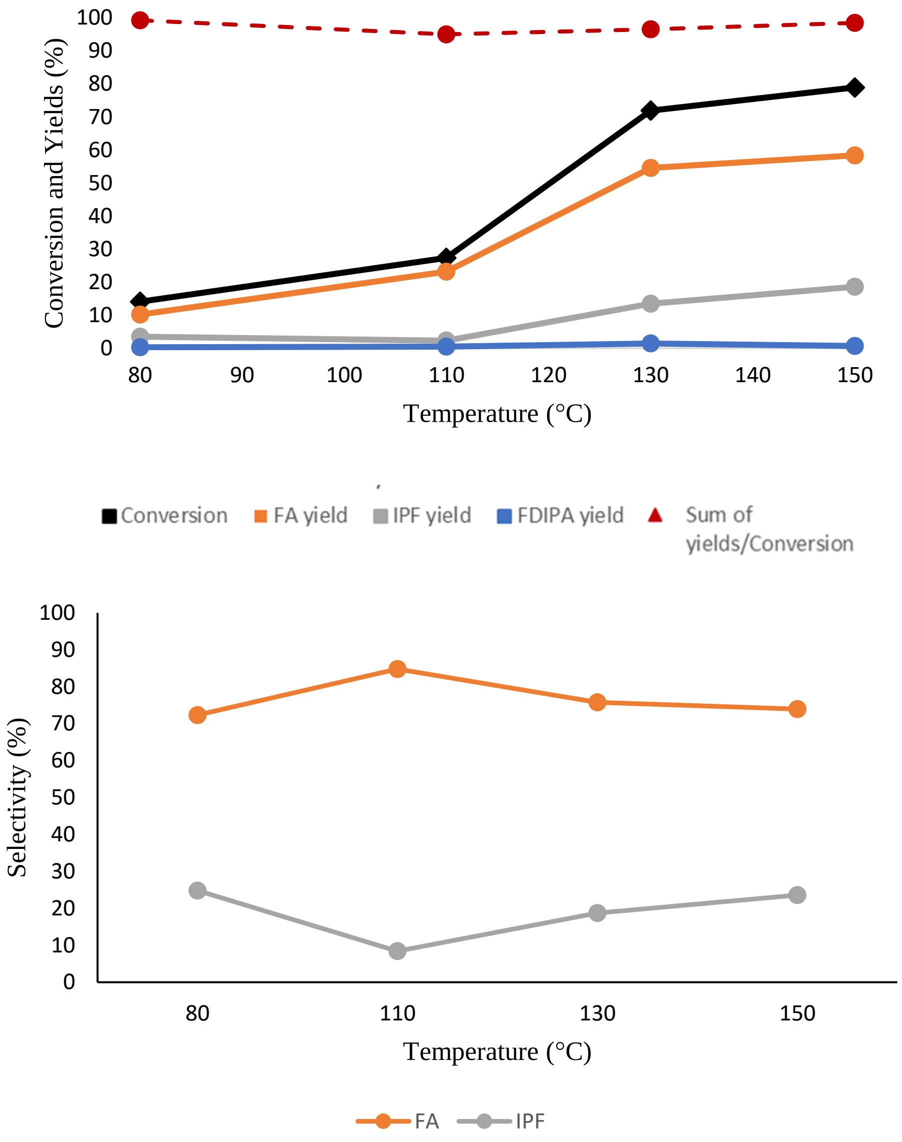

Figure 64. Effect of temperature in CTH reaction of furfural using Pd 0.5% wt /ZrO_2 (61192). Conditions of reaction: PN_2: 20 bar; stirring: 600 rpm; T=80-110-130-150°C; t=2h; Furfural:metal=500 molar ratio; H-donor:isopropanol; Vtot: 10 mL; 0.05 gr of catalyst. Conversion and yields (up) and selectivity (down) as functions of Temperature

At low reaction temperatures, 80 and 110 °C, the CTH reaction occurs in a limited manner: the FA yield and the FF conversion were low, in particular at 80 °C where there was a conversion of 14%. Increasing the temperature (130 °C) resulted in a clear improvement in catalytic performance, reaching a conversion of around 72% and a FA yield around 54.5%. By increasing the temperature to 150 °C a conversion of 79% and a FA yield of 58% were achieved. Comparing the selectivities in FA at 130 °C and 150 °C, this was higher at lower temperatures, with a selectivity equal to 76 and 74% at 130 °C and 150 °C respectively. The selectivity in IPF is 19% and 26% at 130°C and 150°C respectively. At 130°C the reaction was therefore more shifted towards the formation of FA and there was lower selectivity for the formation of by-products. Consequently, from the results obtained, for the optimization of the other reaction parameters it was decided to focus on the temperature of 130 °C, since it has the advantage of being lower and leading to greater selectivity in furfuryl alcohol.

Optimization of reaction parameters: Effect of catalyst pretreatment temperature

The catalyst used was pre-treated in an oven at 150 °C for 4 hours. The purpose of this is to remove physisorbed water during the reaction, but also to pre-treat the catalyst at a temperature that was equal to or higher than the reaction temperature, so that the different activity of the catalyst does not depend from the structure of the catalyst that can change at different temperature of the reaction, but just from the temperature of the reaction, starting from the assumption that by calcining them at the same temperature they have the same structure. Since the reaction was carried out at temperatures ranging from 80 °C to 150 °C, the catalyst was pretreated at 150 °C. To evaluate the effect of the pretreatment, we consequently went to higher temperatures, of 200 °C and 250 °C, 150 °C being the minimum possible to cover the entire reaction temperature range. The results obtained are shown in Figure 65.

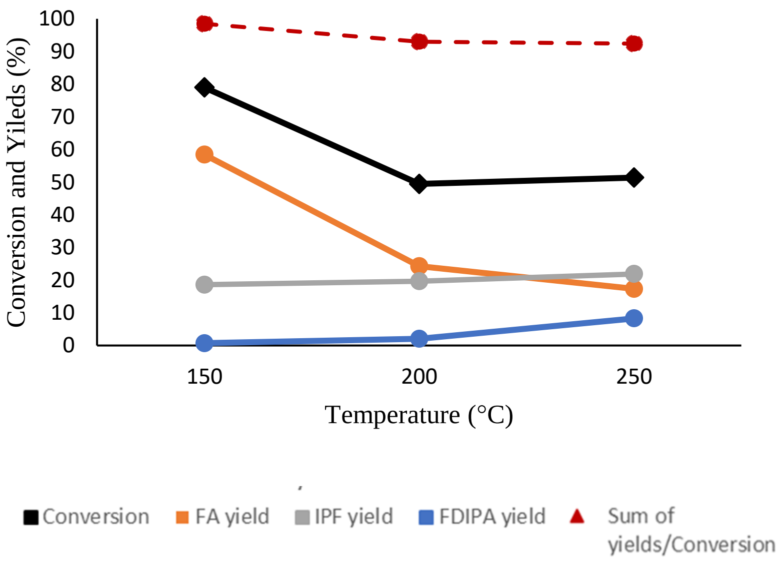

Figure 65. Effect of pretreatment temperature of the catalyst in CTH reaction of furfural using Pd 0.5% wt /ZrO_2 (61192). Conditions of reaction: PN_2: 20 bar; stirring: 600 rpm; T=130°C; t=2h; Furfural:metal=500 molar ratio; H-donor:isopropanol; Vtot: 10 mL; 0.05 gr of catalyst.

From the results obtained it can be seen that by pre-treating the catalyst at temperatures higher than 150 °C the catalytic performance tends to decrease. The conversion, in fact, decreased from 79% at 150 °C pretreatment to values of 49% and 51% at 200 °C and 250 °C pretreatment respectively. The FA yield also tended to decrease, with values of 24% and 17% at 200 and 250

°C pretreatment respectively. At the same time, we see an increase in the yield of by-products, especially FDA.

The lower catalytic performance of the catalyst at higher temperatures may be due to different reasons:

- sintering of the nanoparticles, favored by high temperatures, which tends to form larger and consequently less active nanoparticles
- increasing of the formation of PdO, as the samples are heat treated under air.
- Higher formations of light or heavy products adsorbed on the surface of the catalyst, that could explain the lower carbon balance at higher pretreatment temperatures

To better understand the causes of the different catalytic activity with different catalyst pretreatment temperatures, it would be necessary to carry out some characterizations, such as TGA analysis in order to understand the fraction of organic compounds adsorbed on the catalytic surface; BET and XRD analysis to evaluate a possible change in surface area and crystalline structure; TEM analysis to evaluate whether there has been a change in the distribution of the metal nanoparticles, their average size and to evaluate possible sintering phenomena; XPS analysis to evaluate the oxidation state of Pd.

3.4.3.3 Reusability studies

Following the optimization of other reaction parameters, the reusability of the tested catalyst under optimized conditions was assessed. In particular, at the end of the reaction this was separated from the reaction solution, left to air dry and then dried in oven at 80 °C for 4h, in order to remove the physisorbed solvent but at the same time not burn the deposited organic part thanks to using a low temperature. It was then tested for two subsequent reaction cycles. The results are reported in Figure 66.

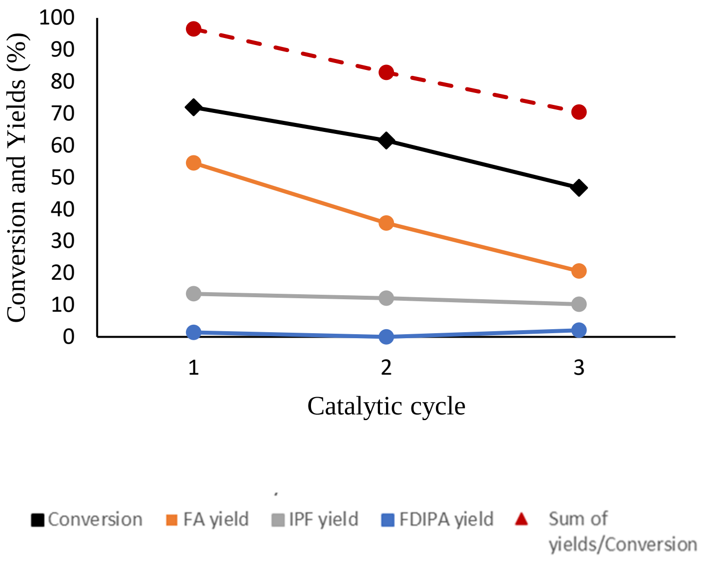

Figure 66. Recycling tests for Pd 0.5% wt /ZrO_2 (61192) catalyst is CTH of furfural. Conditions of reaction: PN_2: 20 bar; stirring: 600 rpm; T=130°C; t=2h; Furfural:metal=500 molar ratio; H-donor:isopropanol; Vtot: 10 mL; 0.05 gr of catalyst.

In the second and third reaction cycles we see that the conversion progressively decreased with a drastic drop also in the FA yield and IPF yield, which decreased to 21 and 10% respectively. A low sum of yields/conversion was also seen, indicating the adsorption of thought products on the catalyst surface or the formation of light products, which were not identified by the GC analysis. A treatment to regenerate the catalyst by burning the organic product fraction could help restore the initial catalytic properties. Specific tests should be carried out to exclude leaching phenomena, for example through ICP analysis of the post-reaction solution.

Catalyst characterization

For the characterization of the catalysts we focused on Pd 0.5% wt/ZrO_2 (61192), since it is the one for which the reaction parameters were optimized. In particular, we performed on the support a BET analysis to evaluate the specific surface and an XRD to evaluate the crystalline structure. Then, a TPD-NH_3 study was carried out to evaluate the strength and density of the acidic and basic sites and compare the results obtained with the ZrO_2 support (61192) and the 1%wt Pd /ZrO_2 catalyst. We then proceeded with TEM and XPS analysis to evaluate the particle size and dispersion of the nanoparticles and the oxidation state of Pd on the surface.

BET and XRD analysis on the support

The support ZrO_2 61192 have been characterized with BET and XRD analysis. The composition of the support was already known and given by the supplier company but reconfirmed by an

ICP analysis. In particular, the support consists of: ZrO_2 (90%), SO_3 (4.7%), SiO_2 (3.3%), HfO_2(1.9%).

The specific surface area has been calculated with BET analysis: it results to be 176 m^2/g.

To evaluate the crystalline structure of the support, an XRD analysis was carried out. The XRD pattern is shown in Figure 67. The blue *m* indicates the peaks corresponding to the monoclinic phase, while the red *t* indicates those corresponding to the tetragonal phase.

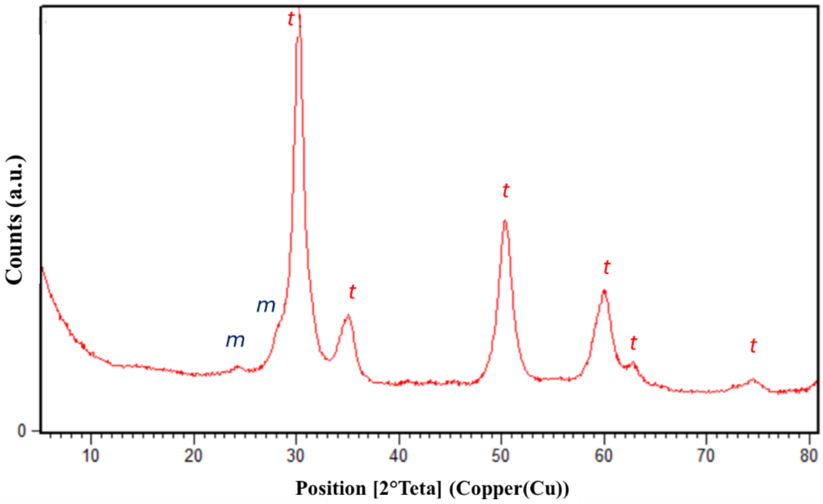

Figure 67. XRD pattern of ZrO_2 (61192).

Zirconia 61192 is highly crystalline, mainly of tetragonal crystalline phase (*t*), with some small ones of lower intensity corresponding to the spectrum of monoclinic zirconia (*m*).

TPD analysis

As explained in previous chapters, Lewis acidic and basic sites appear to have a fundamental role in the MPV mechanism. Consequently, the strength and number of total acidic and basic sites were studied by NH_3-CO_2-TPD analysis for the zirconia support and for the two catalysts Pd 0.5wt% and Pd 1wt% supported on ZrO_2. Figure 68 and Figure 69 show the TCD profiles of desorption of NH_3 and CO_2 respectively for the three samples.

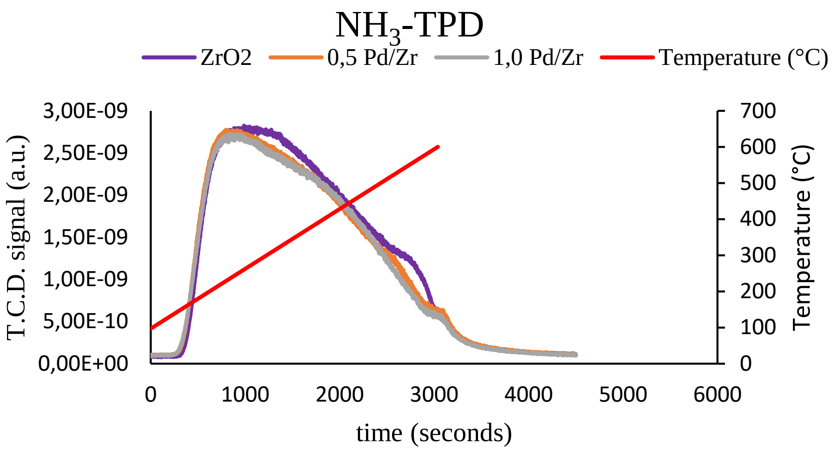

Figure 68. NH_3 desorption profile in TPD analysis of ZrO_2 (61192); Pd 0.5% wt/ZrO_2 (61192); Pd 1% wt /ZrO_2 (61192).

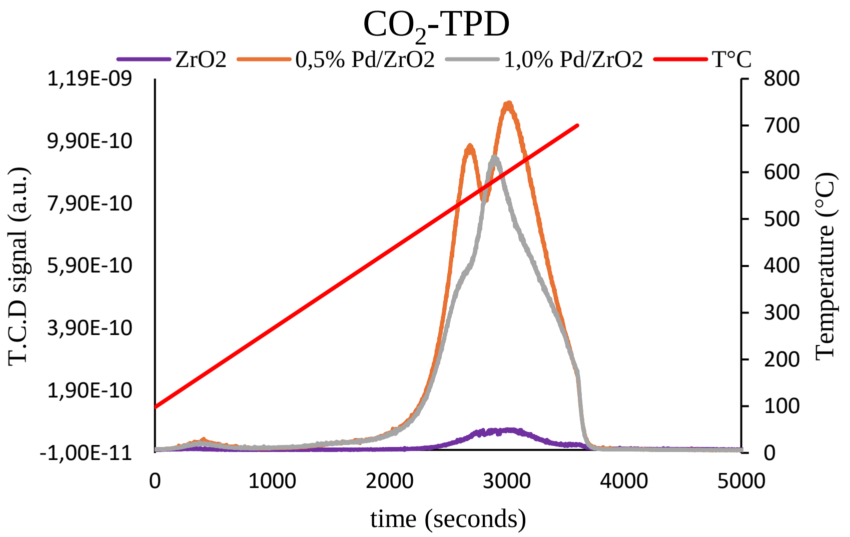

Figure 69. CO_2 desorption profile in TPD analysis of ZrO_2 (61192); Pd 0.5% wt/ZrO_2 (61192); Pd 1%wt /ZrO_2 (61192).

Table 13. Acid and basic sites density and T max of desorption of NH_3 and CO_2 for ZrO2, 0.5%wt Pd/ZrO_2 and 1% wt Pd/ZrO_2.

Catalyst	Acid Site NH_3 desorption (mmol/g)	NH_3 T max desorption (°C)	Basic Site CO_2 desorption(mmol/g)	CO_2 T max desorption (°C)
ZrO_2	0.618	260	0.008	550-600
0.5 Pd /Zr	0.574	240	0.187	600
1.0 Pd / Zr	0.547	240	0.163	577

From the data obtained we can see that as the amount of Pd increased, the density of the acidic sites tends to decrease. Furthermore, by loading palladium, the maximum ammonia desorption temperature drops from 260 °C for pure zirconia to 240 °C for the two samples with palladium, indicating that the acid sites in the presence of palladium were weaker, being the lowest ammonia desorption temperature.

Regarding the basic sites, the presence of Pd significantly increased the density of basic sites, with a density over 20 times higher than pure zirconia. This may be due to the fact that Pd, treated in an oven with air, increased the formation of PdO, consequently in its presence the number of basic sites increased. The catalyst with 0.5% wt Pd had a higher density of acidic sites compared to 1% wt Pd: this result may indicate that more basic surface sites were present in the case of 0.5% Pd, due to the smaller size of the nanoparticles compared to 1 Pd % and maybe a higher number of PdO species.

TEM-EDX analysis

TEM-EDX analysis was carried out in order to calculate the particle size and, identify the degree of dispersion of the Pd nanoparticles and to better understand the structure of the Zirconia support. Figure 70 shows the STEM image and TEM-EDX images of the 0.5% Pd catalyst.

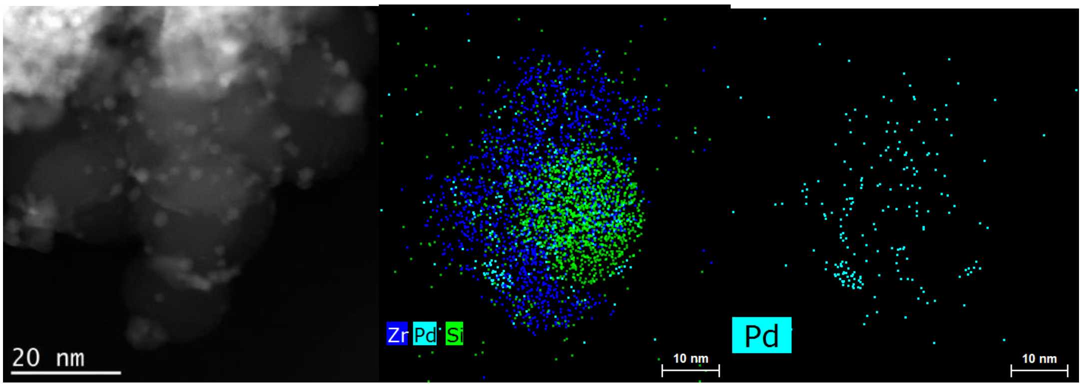

Figure 70. STEM and TEM-EDX images of Pd 0.5 % wt /ZrO$_2$ (61192).

From STEM-EDX mapping, it can be seen that the Si atoms tend to arrange themselves in "globular" structures within the zirconia material, concentrating in certain areas. Palladium, in blue, is preferentially arranged in the areas where ZrO_2 is present rather than where SiO_2 is present. The palladium was relatively well dispersed, with some areas where however a greater density was found. Palladium nanoparticles appear to have small dimensions, in the order of a few nanometers.

Figure 71 and Figure 72 show another STEM and TEM-EDX images of the same sample.

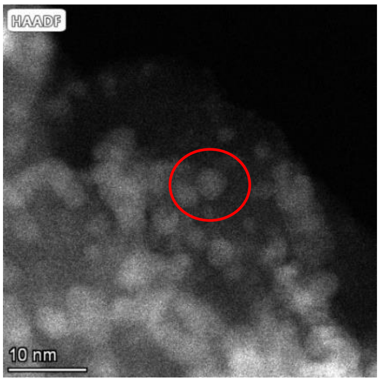

Figure 71. TEM image of Pd 0.5%wt/ZrO_2 (61192). In the red circle a Pd nanoparticle is highlighted.

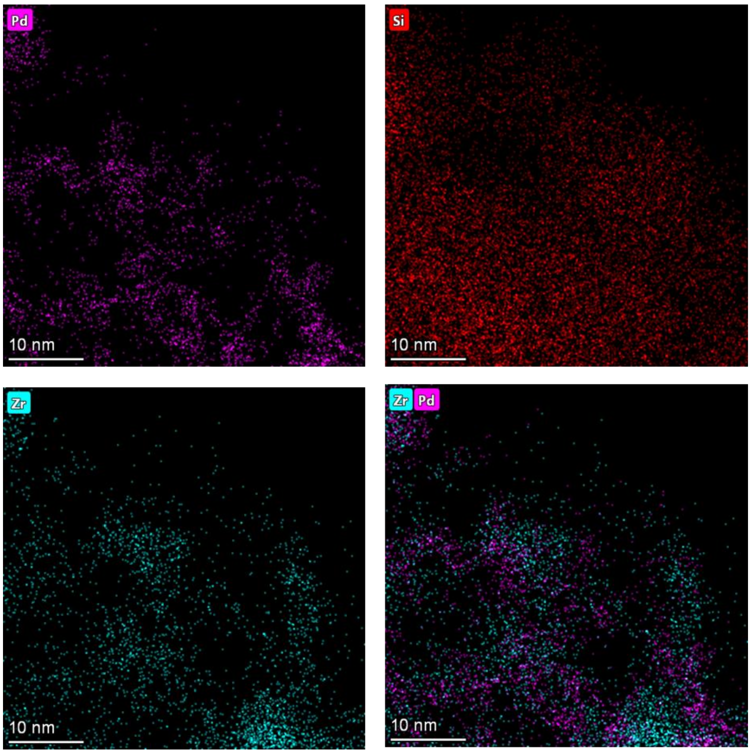

Figure 72. TEM-EDX images of Pd 0.5%wt/ZrO_2 (61192). In particular are reported (from left right and up to down): Pd; Si; Zr; Zr and Pd.

Also in this case we see that the palladium was preferentially arranged in the areas where there is the ZrO_2: in the two STEM-EDX images Zr and Zr-Pd, we see that the palladium, in fuchsia, tends to "reproduce" the position of where the zirconia. Also in this case we see a good dispersion of Pd, although there are areas with a greater density of Pd, which can however be attributed to its preference to deposit on zirconia. From the TEM image we can deduce the presence of Pd nanoparticles (circled in red) of small dimensions, of the order of a few nanometres. From the STEM images it is possible to calculate the size distribution of the Pd nanoparticles, shown in Figure 73.

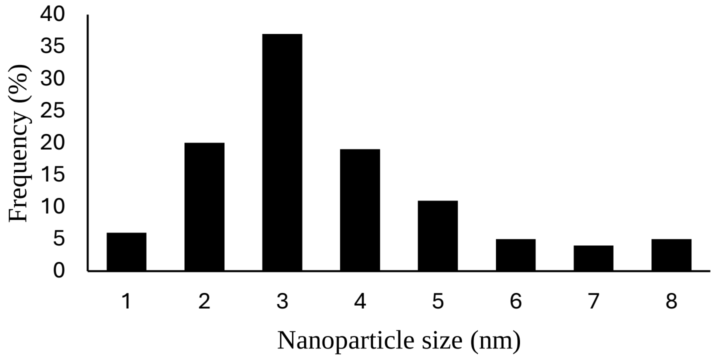

Figure 73. Distribution of nanoparticle dimensions for Pd 0.5% wt /ZrO_2 (61192).

In general, nanoparticles have a size around 2-4 nm, with a maximum at 3 nm. The average particle size is 3.6±1.7 nm. The maximum size identified is 8 nm. With this technique, small and well-dispersed nanoparticles were therefore obtained.

XPS analysis

The XPS analysis was carried out on the 0.5 % wt Pd /ZrO_2 catalyst (61192) in order to evaluate the oxidation state of palladium. The results obtained are shown in Figure 74.

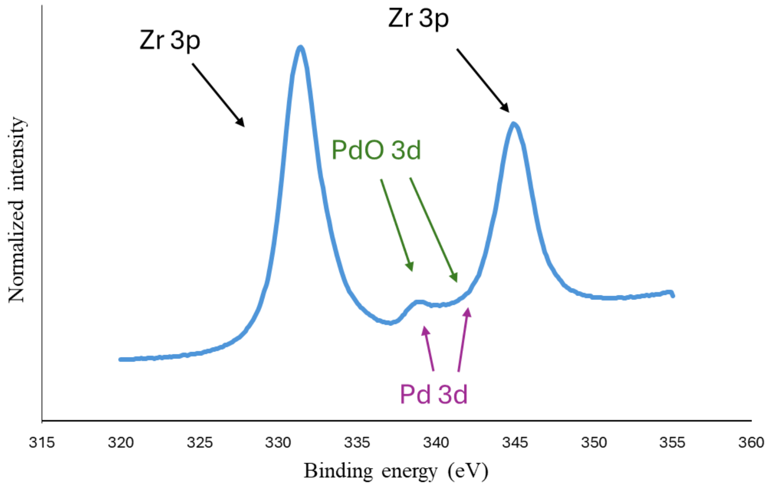

Figure 74. XPS analysis of Pd 0.5% wt /ZrO_2 (61192). Peaks of Zr (3p) and Pd (3d)

By examining the spectrum in the Pd region, it is seen that this is overlapped with the Zr (3p) peaks, as reported in the literature [127]. The peak (3p) of zirconia has a binding energy of 331.4 eV and 345.1 eV. In the region between 345 eV and 346 eV PdO and Pd(3d) are present, as can be seen from the widening of the peak. Due to the small quantity of palladium present (around 0.5% wt, confirmed by XPS analysis) the quantification of the ratio between Pd(II) and Pd(0) is complex.

3.4.4 Effect of gold in Furfural catalytic reduction

Having evaluated the effect of palladium for furfural catalytic reduction, it was decided to study the effect of gold on the same reaction. In particular, we proceeded by studying the monometallic catalyst based on gold nanoparticles Au/ZrO_2 (61192) and the bimetallic catalyst Au:Pd (1:1)/ZrO_2 (61192) as a reference. In this way, the variation in selectivity and activity in the reaction in question was evaluated when increasing the percentage of gold loaded and decreasing that of Palladium. Figure 75 shows the percentages of gold and palladium for the two catalysts mentioned above, comparing it with the Pd 1%wt/ZrO_2 catalyst (61192).

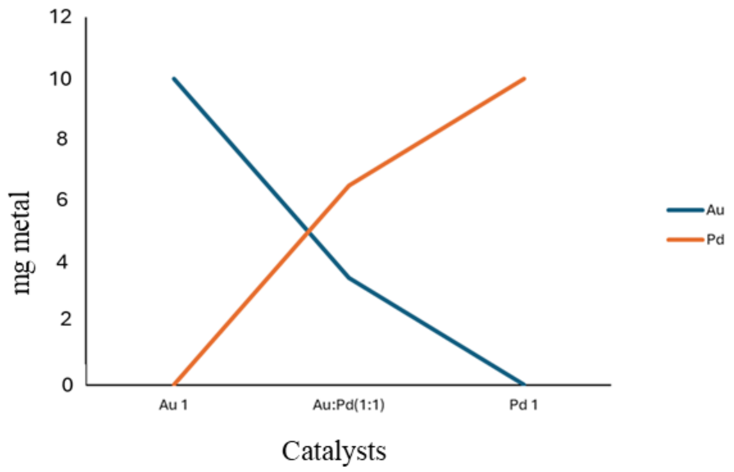

Figure 75. mg of Au and Pd metals in Au/ZrO_2 (61192), Pd 1%wt /ZrO_2 (61192); Au:Pd(1:1)/ZrO_2 (61192)

The three catalysts were tested under standard reaction conditions (T=130°C; PN2=20 bar; t=2h). The results are shown in Figure 76. The quantity of palladium reported on the X axis is related to 1 g of catalyst.

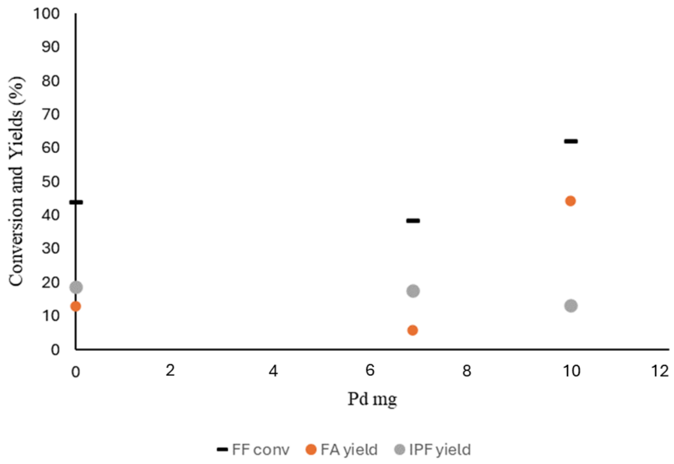

Figure 76. CTH of furfural in autoclave reactor for Au/ZrO_2 (61192); Au:Pd (1:1)/ZrO_2 (61192); Pd 1% wt /ZrO_2 (61192). Conditions of reaction: PN_2: 20 bar; stirring: 600 rpm; T=130°C; t=2h; Furfural:metal=500 molar ratio; H-donor:isopropanol; Vtot: 10 mL; 0.05 gr of catalyst.

Comparing the three catalysts Au, Pd 1% and Au:Pd(1:1), we see that the bimetallic catalyst is the one with the lowest catalytic activity. For monometallic gold catalyst (Pd mg= 0) the selectivity was more shifted towards the formation of the IPF. For the Pd monometallic catalyst (Pd mg=10) the selectivity was more shifted towards the formation of FA. From the results obtained it can be seen that monometallic catalysts were the most active in the reaction under examination, and depending on the metal used the selectivity of the reaction is more or less shifted towards one of the reaction products. Bimetallic catalysts fit into an intermediate point, with poor selectivity for any reaction product, and therefore worse catalytic performance.

3.4.5 Effect of furfural/ metal ratio: Au:Pd (1:1)/ZrO$_2$ (61192) catalyst

It was decided to evaluate the effect of the furfural/metal ratio in the CTH reaction of furfural. In particular, the hydrogenation reaction was carried out using Au:Pd(1:1)/ZrO$_2$ (61192) as the catalyst in standard conditions (T= 130 °C; stirring rate= 600 rpm; t=2h). The catalyst was tested under the following conditions:

- Furfural:metal ratio= 500 molar ratio
- Furfural:metal ratio=250 molar ratio
- Furfural:metal ratio=750 molar ratio

The results are reported in Figure 77.

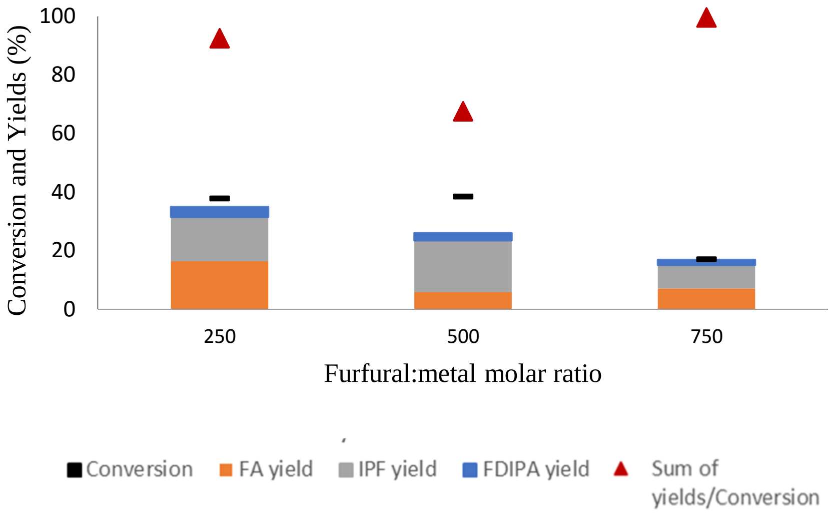

Figure 77. Effect of furfural:metal molar ratio in CTH reaction of furfural using Au:Pd(1:1)/ZrO$_2$ (61192). Conditions of reaction: PN$_2$: 20 bar; stirring: 600 rpm; T=130°C; t=2h; Furfural:metal=250-500-750 molar ratio; H-donor:isopropanol; Vtot: 10 mL; 0.05 gr of catalyst.

Comparing the three reactions carried out at 130 °C for two hours with different furfural:metal molar ratio, it is observed that with Furfural:metal ratio=500 molar ratio there is the greater activity of the catalyst, with a conversion of 38%, while at higher molar ration (furfural:metal ratio=750) the conversion is lower (17%), due to the fact the we are using less metal as catalyst as expected; at lower molar ratio (furfural: metal=250) the conversion is lower (38%) than at 500 molar ratio: it seems that there are diffusion limitations when we decrease the molar ratio below 500, because even if we use more catalyst the conversion was almost the same to the conversion at 500 molar ratio. Focusing on the yields of the products, we can see that we have a higher yield (16%) of Furfuryl alcohol at 500 molar ratio. Instead, at molar ratio of 750 we had a yield of FA of 7% and at 250 molar ratio a yield of 6%, with an increase in the production of IPF, with an yield of 15%. This suggests that by increasing the substrate: metal ratio the reaction is shifted more towards the formation of the IPF: this result may be interesting for the formation of isopropyl levulinate, a particularly interesting molecule at an industrial level, which can be obtained from the alcoholysis of IPF.

Catalyst characterization

The Au/ZrO_2 (61192) catalyst has been characterized using TEM and XPS analysis. The STEM images are reported in Figure 78.

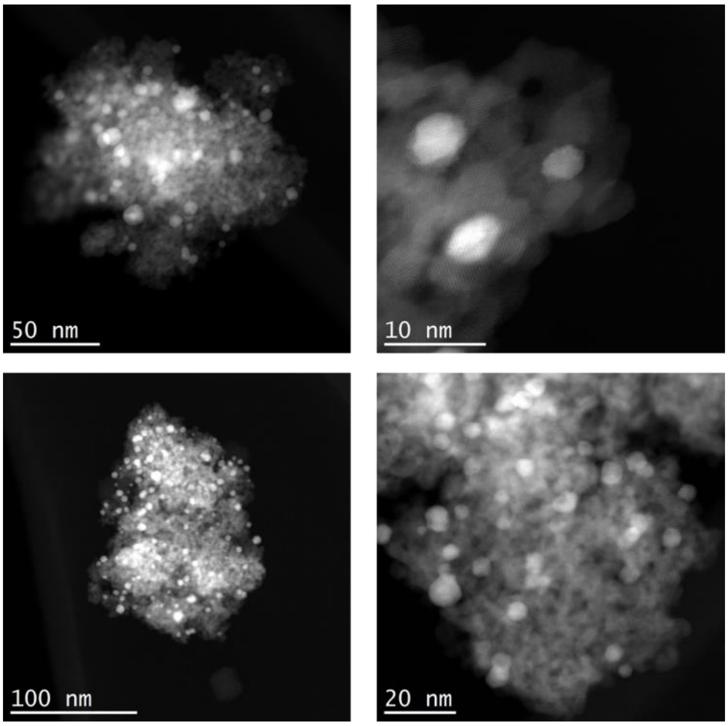

Figure 78. STEM images of Au/ZrO_2 (61192).

From the STEM images we can confirm a good dispersion of the Au nanoparticles on the zirconia support. We managed to obtain Au nanoparticles of small dimensions, around few nanometres. In particular, analysing the dimension of more than 150 nanoparticles the distribution of the dimension have been calculated and reported in Figure 79.

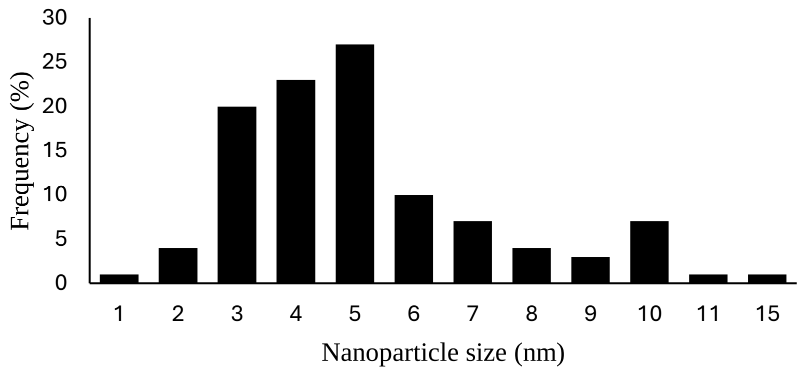

Figure 79. Nanoparticle size distribution for Au/ZrO_2 (61192) catalyst.

The majority of the nanoparticles have dimensions between 3-5 nm, with an average particle size of 5.2 ±1.7 nm. We can find also nanoparticles of smaller and bigger dimensions, but in smaller quantity. There are some agglomeration and formation of big nanoparticles of 15 nm in small quantity. Making a comparison of these results with the Pd 0.5 % wt /ZrO_2 (61992) we can see that in general we have the formation of bigger nanoparticles for gold catalyst respect to palladium catalyst. The reason of this could be found in the intrinsic properties of the metal and the interactions with the stabilizing agent. However, the main factor is the different loading between the two catalysts: indeed, for the Au catalyst we have a double loading of metal (1% wt) in comparison with the Pd catalyst studied with TEM analysis (with 0.5% wt metal loading). A higher loading could bring to a greater proximity between the nanoparticles, that for this reason tend to sinter, leading to bigger nanoparticles.

In Figure 80 we reported the TEM mapping of Au/ZrO_2 (61192), where the Au nanoparticles are highlighted in pink.

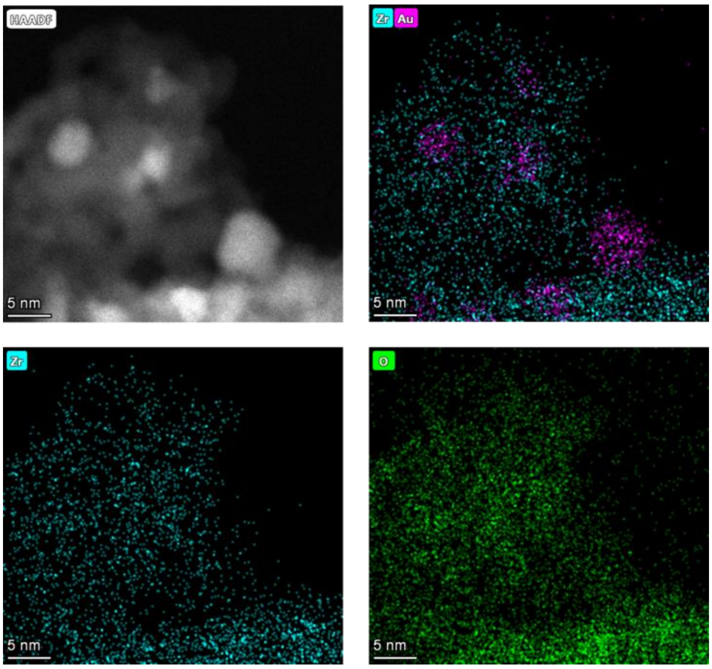

Figure 80. TEM images of Au/ZrO$_2$ (61192)

XPS analysis has been performed on Au/ZrO$_2$ (61192). In Figure 81 the signal for Au (4f) peaks are reported. In particular, the signal at higher energy is the 4f$_{5/2}$, while the signal at lower energy is the 4f$_{7/2}$. The area ratio of the two signal is ¾. From the signal 4f$_{7/2}$ is possible to determine the oxidation state of the superficial gold: the peak is at a binding energy of 83.9 eV, indicating the presence of Au in metallic state. It's possible to exclude the presence of Au^{+} and Au^{3+} atoms because there are no peaks at 84.7 eV and 86 eV respectively.

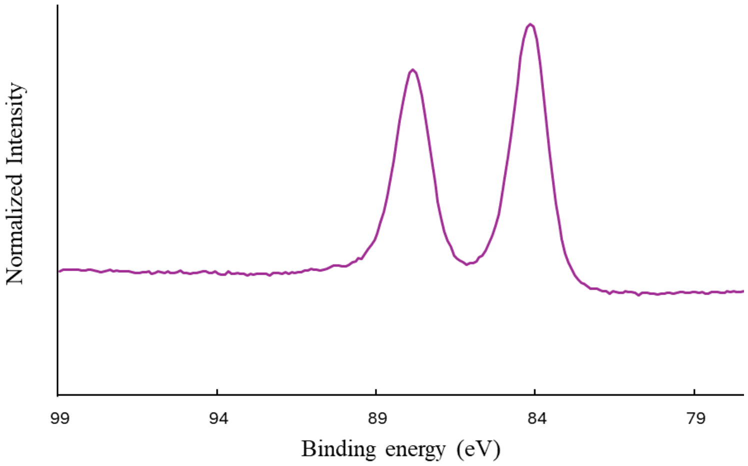

Figure 81. XPS Au (f) peaks for Au/ZrO$_2$ (61192) catalyst.

Au:Pd (1:1)

The Au:Pd (1:1)/ZrO_2 (61192) catalyst has been characterized with TEM analysis.

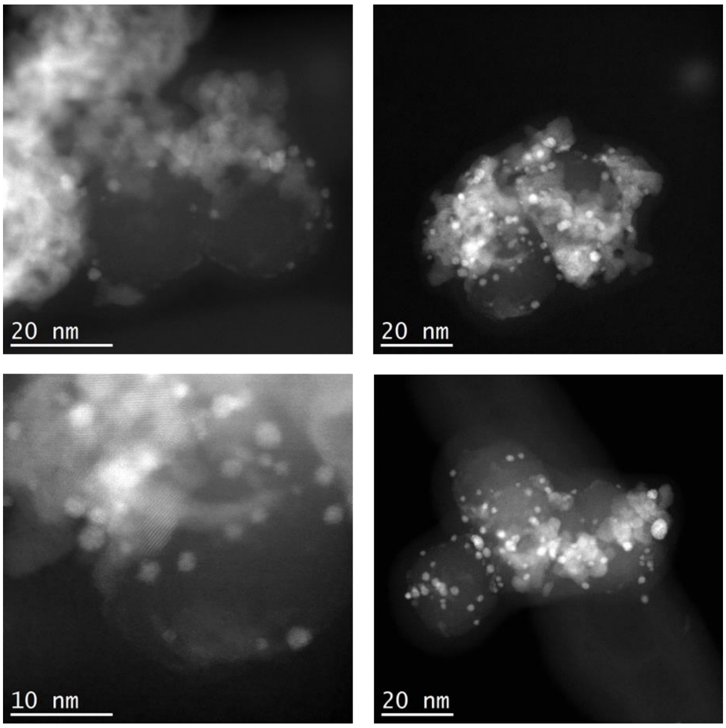

Figure 82. STEM images of Au:Pd (1:1)/ZrO_2 (61192)

From the STEM images (Figure 82) we can see a good dispersion of the Au-Pd nanoparticles, which are well separated from each other. Furthermore, by measuring the size of approximately 150 nanoparticles, their distribution was calculated, shown in Figure 83.

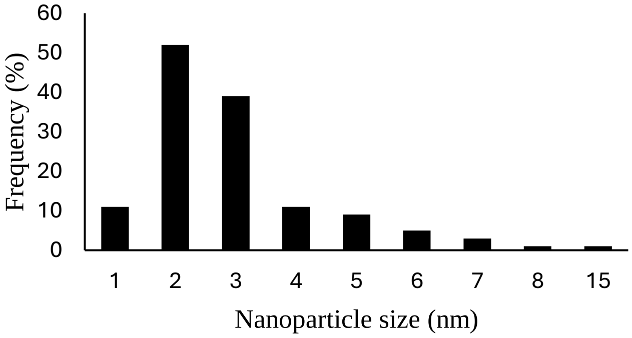

Figure 83. Nanoparticle size distribution for Au:Pd (1:1) /ZrO_2 (61192) catalyst.

Most of the nanoparticles have a size between 2 and 3 nm, with an average particle size of 3±2.3 nm. There are a few larger nanoparticles. Also in this case therefore, a good degree of dispersion of the nanoparticles was obtained and small nanoparticles were obtained. We also see that these are smaller on average than the Au/ZrO_2 catalyst (61192), with similar dimensions to the Pd 0.5%wt /ZrO_2 catalyst (61192).

Figure 84 shows the mapping images of a section of the catalyst, compared with the corresponding TEM image. Au-Pd nanoparticles tend to preferentially deposit on top of zirconia rather than SiO_2. Furthermore, from the images it is clear that the nanoparticles have an alloy structure, as expected from the synthetic procedure used and from the use of a strong reducing agent and in large quantities compared to the metal (with reducing agent: metal=5: 1 molar ratio), which consequently leads to an immediate reduction of both metals and the formation of an alloy structure.

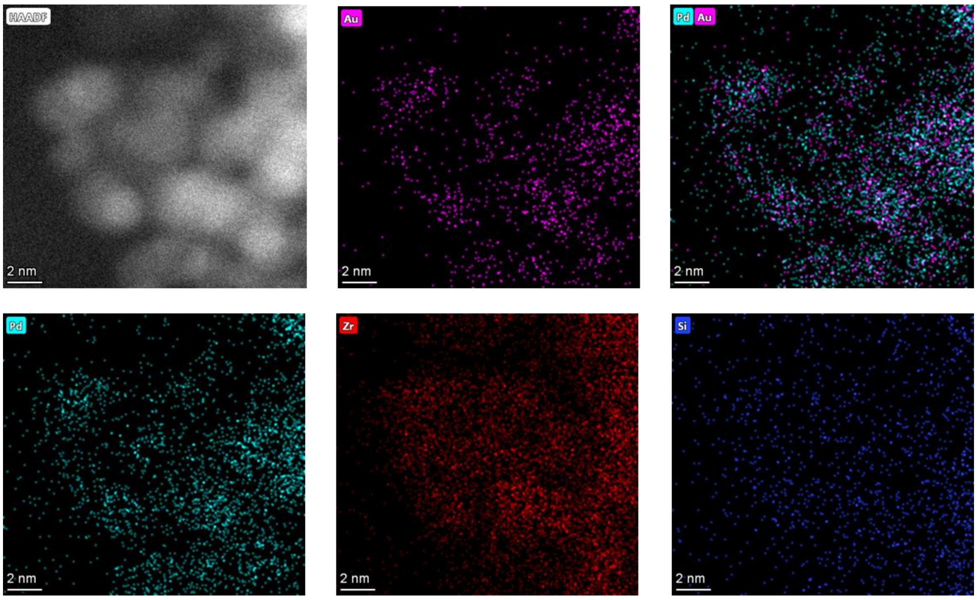

Figure 84. TEM image of Au:Pd (1:1)/ZrO2 (61192) and mapping of Au, Pd, Zr and Si elements.

3.5 Conclusions and future work

Ten catalysts of metal nanoparticles supported on a commercial zirconia ZrO_2 (61192), containing impurities of SO_3, SiO_2 and HfO_2, were synthesized using the sol-immobilization technique. In particular, monometallic gold and palladium catalysts and bimetallic Au-Pd catalysts have been synthesized.

A screening of the synthesized catalysts, together with ZrO_2 support (61192), in the CTH reaction of furfural in liquid phase was carried out, using isopropanol as H-donor.

The Pd 0.5% wt/ ZrO_2 (61192) catalyst showed the best catalytic performance, with the highest conversion and the highest selectivity towards the formation of Furfuryl alcohol (FA), the desired product. This was then tested in an autoclave-type reactor to optimize the reaction parameters. Under optimized reaction conditions (T=130°C; t=2h; rpm=600) a furfural conversion of 72% and a FA yield of 55% were achieved. The catalyst was characterized by TPD, TEM and XPS analysis. From the results obtained, the presence of both Pd and PdO on the surface of the catalyst was seen. TEM and XPS characterizations are required in the future to confirm the assumptions made on the density of acidic and basic sites regarding supported Pd NPs-based catalysts. The synthesis using the sol-immobilization technique allowed to obtain well-distributed and small-sized nanoparticles, with average values around 3.6±1.7 nm.

The variation in selectivity and activity in the reaction in question was evaluated when increasing the percentage of Gold loaded and decreasing that of Palladium. It has been seen that as the quantity of gold increases, the selectivity shifts towards the formation of IPF, while as the quantity of palladium increases, the selectivity shifts towards the formation of FA. Future work can be conducted by further varying the quantity of Palladium in the support, evaluating the effects on the catalytic activity. Furthermore, the effect of the stabilizing agent used for the synthesis of the catalyst can be evaluated by varying the type of stabilizer and the ratio between it and the metal, studying the effect on the size of the nanoparticles and on the reactivity. Regeneration tests of the catalyst and study of the spent catalyst must be carried out.

4. Oxidation of HMF to FDCA

4.1 Introduction

4.1.1 HMF

Another molecule identified among the “Top 12” starting from biomass is 5-hydroxymethylfurfural, or HMF. This can be produced from C6 carbohydrates through a dehydration process. Due to the presence of an aldehyde group and an alcohol group, HMF is a very highly value-added molecule due to the fact that can be converted into a number of important industrial products, including polymers such as resins and additives. HMF is also an interesting substitute for formaldehyde, since unlike the latter it is toxin-free and often biodegradable.

4.1.2 Oxidation of HMF to furandicarboxylic acid (FDCA)

One of the main uses of HMF is its selective oxidation to furandicarboxylic acid (FDCA). In fact, this product is very important because it is used to produce polyethylene furanoate (PEF), the bio substitute of PET, which is the main plastic for the production of bottles and packaging. Indeed, FDCA is the ideal substitute for terephthalate, [128]. In general, it is a highly desirable product as a substitute for products of fossil origin to produce polyesters [129] and resins [130]. It can also be used for the synthesis of several metal-organic frameworks (MOFs) [131,132].

The main reaction mechanism proposed during the oxidation with air or pure O_2 in liquid phase with the use of different types of catalysts focusing on supported metal nanoparticles, is the following: Oxidation takes place in two steps: in the first step there are two competitive reactions, the formation of 5-hydroxymethyl-2-furancarboxylic acid (HMFCA) and 2,5-diformylfuran (DFF). Subsequently, both of these two intermediates are oxidized to 5-formyl-2-furancarboxylic acid (FFCA), which is in turn finally oxidized to FDCA by reduction of the aldehyde group [133]. This step was normally performed by homogeneous catalysis using cobalt-based catalysts and acetic acid as solvent [134]. However, this process has been replaced by heterogeneous catalysts, which are more convenient because they can be easily separated from the post reaction and reused. In particular, for this reaction catalysts based on nanoparticulate Au and Pd on different supports are used [135-137], where in particular gold was found to be the one with the best catalytic performance because it is more resistant to oxidation phenomena and therefore deactivation of the catalyst. Furthermore, in the reported study by Albonetti et Al., [138], it was reported that not only the type of metal but also the support affects the catalytic activity in the oxidation of HMF. In particular, Au-based catalysts on TiO_2 and CeO_2 were tested: the latter proved to be the one with the best catalytic performance and with greater selectivity towards FDCA, reaching a yield of 52% in 4 h of reaction under optimized conditions (10 bar O_2, 4eq. NaOH, 70 °C). This is due to the fact that the transition from Ce^{4+} to Ce^{3+} occurs easily, allowing storage of oxygen and increasing its mobility from the catalytic structure to the substrate. Furthermore, the presence of numerous oxygen vacancies on the ceria favors the formation of Lewis acid sites and of cationic Au, which synergistically favor the reaction between the aldehyde group, the OH^- and the molecular oxygen [139-143]. However, monometallic catalysts of supported gold nanoparticles show a fast deactivation over time due to the formation of humins [144]. Bimetallic catalysts such as Au-Cu have also been tested [145] allowing to obtain an almost total conversion to FDCA in 4h at 95 °C. Catalysts based on Au-Pd on different supports have also been tested: Zinc hydroxycarbonate (ZOC) [146]; basic anion-exchange resin (AER)[147,148], Au-Pd nanoparticles supported on Activated carbons [149] showing excellent catalytic performance in terms of selectivity towards FDCA (>99%) and catalytic activity at mild reaction conditions. Moreover, these bimetallic catalysts with respect to the monometallic ones are active and stable even after numerous catalytic cycles, unlike the monometallic ones.

Furthermore, it has been reported that the presence of OH^- groups is fundamental for the enhancement of catalytic activity and the participation in the reported oxidation mechanism. These groups, in fact, are present in solution and allow the formation of diols from water and aldehyde; another part, on the other hand, tends to adsorb on the surface of the catalyst, stripping hydrogens from the -OH and -CH groups of the alcohol or diol that is formed, thus favoring the formation of carbonyl groups. The electrons formed, in the presence of oxygen, allow to regenerate the groups OH^- see Figure 27 [150].

For this reaction, the effect of the support using gold nanoparticle-based catalysts was studied and reported in literature. In particular, it was seen that oxides such as CeO_2 and TiO_2 showed the best catalytic performances, reaching a yield of 100% FDCA in 8h of reaction. Furthermore, they allow to work in aqueous medium in mild conditions with low temperatures (85 °C) [150].

4.2 Scope

In this work, several catalysts of supported nanoparticles, both mono and bimetallic, have been synthesized using the sol-immobilization technique and have been tested in the oxidation reaction of HMF to FDCA. In particular, we focused on evaluating the effect of the type of support, using ZrO_2, the type of metal and the ratio between the two metals in the case of bimetallic catalysts for the reaction under examination. We focused on ZrO_2 since it is a support that has not been studied thoroughly in the literature for this reaction and its influence in terms of metal-support interaction and therefore stability of the preformed colloidal nanoparticles could be significant. The most active and selective catalyst for the formation of FDCA was further characterized and tested in an autoclave reactor, by further optimization of the reaction conditions.

4.3 Experimental part

4.3.1 Synthesis of catalysts

The same series of catalysts tested for this reaction, where also tested in the liquid-phase hydrogenation reaction. This study made it possible to compare the performance of the same catalyst in different types of reactions (hydrogenation and oxygenation), solvent (isopropanol and water) and substrate (furfural and HMF). The additionally synthesized and tested catalysts, not tested in the furfural hydrogenation reaction, are shown in Table 14.

Table 14. List of additional catalysts synthetized specifically for the oxidation of HMF

Catalyst	Metallic nanoparticles	Theorical metal loading (wt %)
Au/ZrO_2 (61143)	Au	1
Au/ZrO_2 (61152)	Au	1

4.3.2 Characterization of catalysts

The characterization of the presented catalysts in this section are the same as described in chapter 3.2.4.

4.3.3 Oxidation of HMF in liquid phase

The catalytic oxidation of HMF was carried out at the university of Lille, France during my internship abroad. In particular, the screening of different catalysts was carried out in the screening pressure reactor (SPR), the same reactor used for the furfural hydrogenation, where it is possible to carry out 24 reactions in parallel while maintaining constant the reaction conditions. This was done in order to screen initially a number of catalysts. For each reactor, 10 mg of catalyst and 2 mL of aqueous solution of HMF (HMF:metal=100 molar ratio) were added. The reaction was carried out with 3 equivalents of NaOH. The reaction was carried out for two hours at different temperatures, stirring at 600 rpm and 20 bar of air. At the end of the reaction, the reactor was cooled to room temperature, the system was left to vent and finally the various post reactions were filtered with nylon filters with porosity 0.2 μm.

After that, for the best catalysts, the optimization of reaction conditions was studied in a TOP industry autoclave reactor (Figure 85). This reactor has a capacity of 30 mL and is equipped with a heating mantle that allows heating with high efficiency. The cooling system of the reactor instead consists of a line that sends cold air to the mantle.

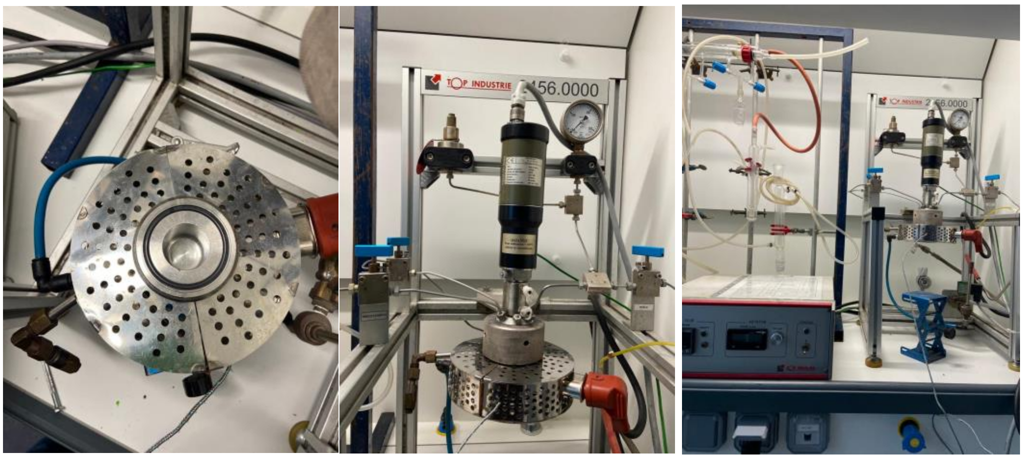

Figure 85. TOP industry autoclave reactor

The agitation consists of a mechanical impeller connected to a cooler which allows it to be refrigerated following friction. This reactor is equipped with a sampling system that allows you to take samples during the reaction.

The reaction was carried out by preparing the reaction solution (10 mL), HMF in distilled water with 3 equivalents of NaOH, adding it to the reactor and finally adding the desired amount of catalyst maintaining a ratio HMF/metal=100 molar. The reactor was then closed, purged with oxygen 3 times and finally charged with 8 bars of oxygen. The reaction was carried out for two hours at different times, stirring rates and quantities of catalyst. At the end of the reaction, the reactor was cooled by the air cooling system, it was opened and the post reaction was taken, the catalyst filtered with HPLC filters with porosity 0.2 μm and analysed by HPLC.

4.3.4 Analysis of post reaction

Post reaction products were analyzed with Shimadzu High Performance Liquid Chromatography (HPLC) (Figure 86) equipped with refractive Index (RI) and UV detectors. The Column used is a Rezex ROA–organic Acid H+ (dimensions Ø 7.8 mm x 300 mm) and the mobile phase of dilute sulfuric acid (H_2SO_4 5 mM, 0.5 mL min^{-1}). The response factors were determined experimentally for the commercial compounds.

The quantification of each product was calculated according to the same analytical procedure reported for the hydrogenation of furfural in chapter 3.2.6.

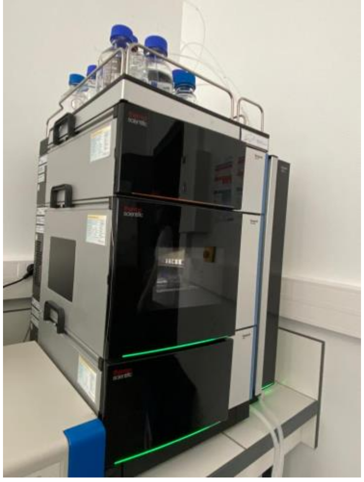

Figure 86. Shimadzu HPLC used of the quantitative analysis of HMF oxidation

In particular, the mol of each product were calculated following the equation:

$$mol_{product} = A_{product} * \ F_{product} * V_{final}(L)$$

Where *A* is the area under the peak corresponding to the compound under investigation; *F* is the response factor of the compound; *V* is the final volume of the post reaction solution reported in litres. Moreover, the conversion (Y) of the starting reagent and the yield (X) and selectivity (S) of each product were calculated following the equations:

$$\text{Y}_{\text{reagent}}= \frac{mol_{initial\,reagent} - mol_{final\,reagent}}{mol_{initial\,reagent}} *100$$

$$\text{X}_{\text{product}}= \frac{mol_{finalreagent}}{mol_{initial\,reagent}} *100$$

$$S_{product}= \frac{X_{product}}{Y_{reagent}} *100$$

4.4 Results

The oxidation reaction of HMF to FDCA has been studied considerably in the literature, not only because the production of FDCA is particularly interesting thanks to its wide applications in the industrial field as an important renewable building block because it can substitute for terephthalic acid (PTA) in the production of polyesters, but also because it is a target reaction used to study the activity of different catalytic systems, especially of supported nanoparticles, where parameters like the influence of particle size, the oxidation state of the metal, the dispersion of the metal nanoparticles, and the metal support interaction can have a significant impact in terms of catalytic performance.

In particular, the reaction can occur through two main mechanisms (as reported in Figure 87): in a first mechanism there is a first oxidation of the aldehyde group to carboxylic acid, forming the intermediate HMFCA; subsequently, this can be oxidized to FFCA before further oxidation to FDCA. In a second mechanism, instead of forming HMFCA from a first oxidation of HMF, DFF is formed through the oxidation of the -OH group to carbonyl. Subsequently the DFF oxidizes first to FFCA and finally to FDCA, as in the case of the other mechanism. Which mechanism is the predominant one depends on the reaction conditions, which stabilize one intermediate rather than another. At high pH it has been seen that mainly HMFCA tends to be formed instead of DFF.

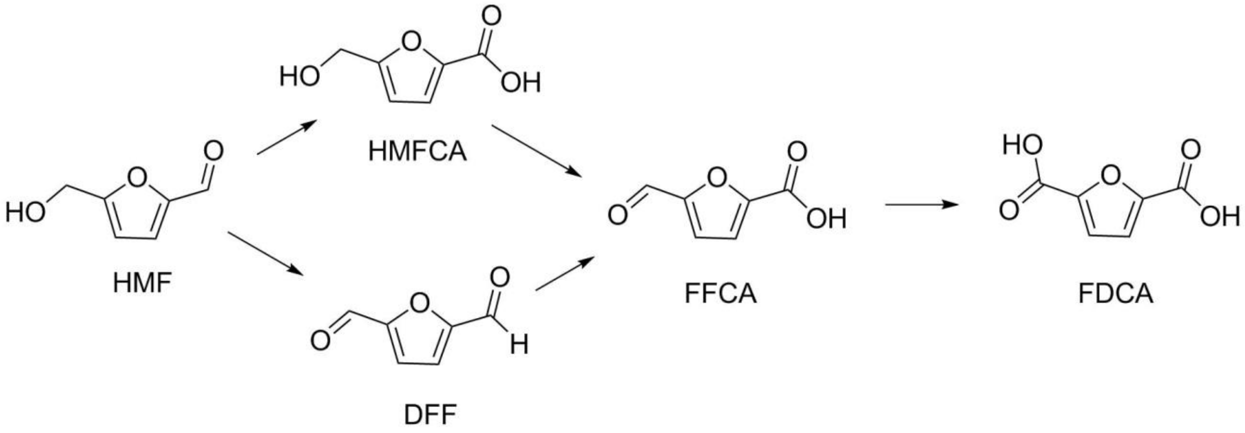

Figure 87. Mechanisms of oxidation of HMF to FDCA

For this reaction it was decided to synthesize different nanoparticle catalysts deposited on different commercial Zirconia supports. The technique used is that of sol-immobilization. In particular, both monometallic and bimetallic nanoparticle-based catalysts were synthesized, varying the composition of the latter in order to evaluate how this acted on the catalytic activity for the oxidation of HMF. Once the best performing catalyst was selected, the reaction parameters were optimised.

4.4.1 Screening of catalysts in HMF oxidation in liquid phase

Three different types of commercial Zirconia were used to synthesize these catalysts. This was characterized using ICP analysis to study its composition and BET to evaluate the specific surface area. The results obtained are shown in Table 15:

Table 15. Composition and surface area of ZrO_2 commercial supports

Support	Composition	Surface area (m^2/g)
ZrO_2 61143	ZrO_2 (83%), WO_3 (15%) HfO_2 (1.5%)	119
ZrO_2 61192	ZrO_2 (90%), SO_3 (4.7%), SiO_2 (3.3%), HfO_2(1.9%)	176
ZrO_2 61156	ZrO_2 (90%), La_2O_3 (7.96%), HfO_2 (1.75%), Al_2O_3 (0.23%)	122

For the monometallic catalysts, three catalysts based on Au nanoparticles were synthesized using the three different supports. For the bimetallic catalysts, we focused on a single support, in particular ZrO_2 61192, since having a higher surface area it seemed to be the most interesting and easy one for the deposition of the nanoparticles. Catalysts based on Au and Pd nanoparticles were prepared by varying the percentages of the two metals. The list of synthesized catalysts is shown in Table 16.

Table 16. List of mono and bimetallic catalysts synthesized and theorical metal loading

Catalyst	Metallic nanoparticles	Theorical metal loading (% wt)
Au/ ZrO_2 (92)	Au	1
Au/ ZrO_2 (56)	Au	1
Au/ ZrO_2 (43)	Au	1
Au-Pd (1:1)/ ZrO_2 (92)	Au, Pd	0.65 Au; 0.35 Pd
Au-Pd (2:1)/ ZrO_2 (92)	Au, Pd	0.78 Au; 0.22 Pd
Au-Pd (3:1)/ ZrO_2 (92)	Au, Pd	0.85 Au; 0.15 Pd
Au-Pd (1:2)/ ZrO_2 (92)	Au, Pd	0.48 Au; 0.52 Pd
Au-Pd (1:3)/ ZrO_2 (92)	Au, Pd	0.38 Au; 0.62 Pd
Pd/ ZrO_2 (92)	Pd	1

4.4.1.1 Catalysts characterization

The catalysts were first characterized by XRF analysis, in order to confirm the loading of the correct amount of metal on the surface of the support. Table 17 shows the results obtained.

Table 17. Results of XRF analysis of mono and bimetallic catalysts

Catalyst	Au (% wt)	Pd (% wt)
Au/ ZrO_2 (92)	1± 0.20	-
Au/ ZrO_2 (56)	0.98 ± 0.18	-
Au/ ZrO_2 (43)	1.1 ± 0.12	-
Au-Pd (1:1)/ ZrO_2 (92)	0.64 ± 0.10	0.33 ± 0.18
Au-Pd (2:1)/ ZrO_2 (92)	0.79 ± 0.18	0.20 ± 0.19
Au-Pd (3:1)/ ZrO_2 (92)	0.85 ± 0.12	0.14 ± 0.10
Au-Pd (1:2)/ ZrO_2 (92)	0.52 ± 0.18	0.57 ± 0.30
Au-Pd (1:3)/ ZrO_2 (92)	0.40 ± 0.20	0.64 ± 0.15
Pd/ ZrO_2 (92)	-	0.96 ± 0.15

As can be seen, for all catalysts the desired percentage of metal was loaded. This confirms that the sol-immobilization technique is effective for the preparation of nanoparticle-based catalysts, both for mono and bimetallic systems. Furthermore, it is therefore possible to compare bimetallic catalysts, observing how variations in the percentages of the two metals influence the catalytic activity for the oxidation of HMF.

For the oxidation of HMF to FDCA the screening of different catalysts were performed. The reaction has been performed at 110 °C and 50 °C for 2 h. The results obtained are reported in Figure 88 for T=110 °C and Figure 89 for T=50 °C.

Screening of catalysts at 110°C for 2 h

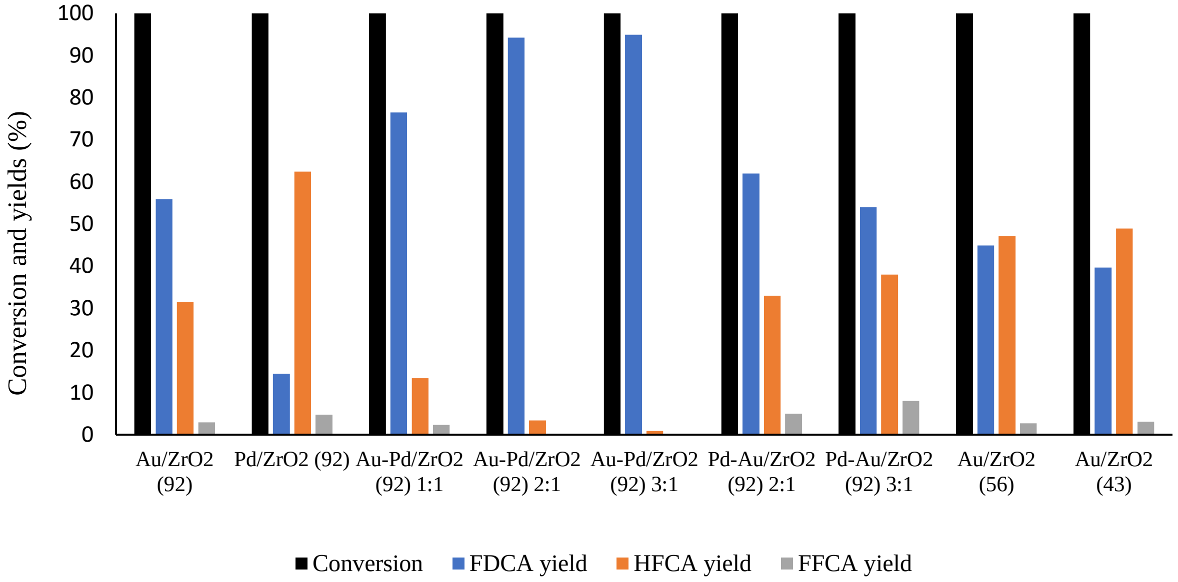

Figure 88. Screening of catalysts in HMF oxidation to FDCA in SPR reactor. Reaction conditions: 20 bar of air; T=110 °C; t=2h; stirring rate= 600 rpm; NaOH:HMF=3:1 molar ratio.

From the results obtained in Figure 88, we see in general a total conversion for all the catalysts was achieved as it is reported in literature at these reaction conditions. Moreover, in all reactions HFCA was produced as intermediate, while there was no trace of DFF. This is due to the strong alkaline conditions, high pH, due to the use of NaOH. NaOH is essential for the activation of gold-based catalysts and facilitate the consecutive oxidation of the intermediates for the production of FDCA.

Comparing the monometallic catalysts, the one with the best catalytic performance is Au/ZrO_2 (92), with a FDCA yield of 56%, followed by Au/ZrO_2 (56) (yield of 45%) and Au/ZrO_2 (43) (39% yield). This may be due to the higher surface area of zirconia (92), as during synthesis it could tend to keep the nanoparticles more dispersed and consequently avoid sintering phenomena, obtaining nanoparticles of smaller particle size and therefore with a higher surface area and finally better dispersion of the Au nanoparticles onto the surface. The palladium-based catalyst, as expected, is not very active in the oxidation reaction, with a yield of 15%.

Regarding bimetallic catalysts, the best catalyst for the production of FDCA was Au-Pd/ZrO_2 (92) 3:1 with a yield of 95%, followed by Au-Pd/ZrO_2 (92) 2:1 (94% of FDCA yield) and by

Au-Pd/ZrO_2 (92) 1:1 (77% FDCA yield). Bimetallic catalysts, in general, were much more selective towards FDCA than monometallic catalysts, with excellent catalytic performance after just two hours of reaction. In general, from these results it can be seen that, although Pd alone is not active in the HMF oxidation reaction, a small percentage of Palladium in a gold nanoparticle catalyst tends to improve catalytic performance: the reason is the formation of alloyed Au-Pd nanoparticles and the role of Au is to act as a diluent for Pd, increasing the catalytic activity as it has been shown previously. This phenomenon consists in the fact that the palladium atoms are kept separate from gold atoms as isolated monomers. In particular, gold atoms, having a high electronic affinity, tend to acquire electrons from the s and p orbitals, losing electrons from the d orbitals, while Pd loses electrons from the s and p orbitals and acquires them for the d orbitals. Consequently, as Pd acquires electrons in the d orbitals, the center of the band moves away from the Fermi level, making the bonds between the Pd atoms weaker. Furthermore, often in these conditions Pd was found to adopt the lattice constant of gold, increasing the Pd-Pd bond length and therefore making the bond weaker. This phenomenon increases in intensity as the Au/Pd ratio increases [151].

Screening of catalysts at 50 °C for 2 h

Considering the excellent catalytic performance at 110 °C only after two hours of reaction, it was decided to test the catalyst using the same reaction conditions but at 50 °C. The results obtained are shown below in Figure 89.

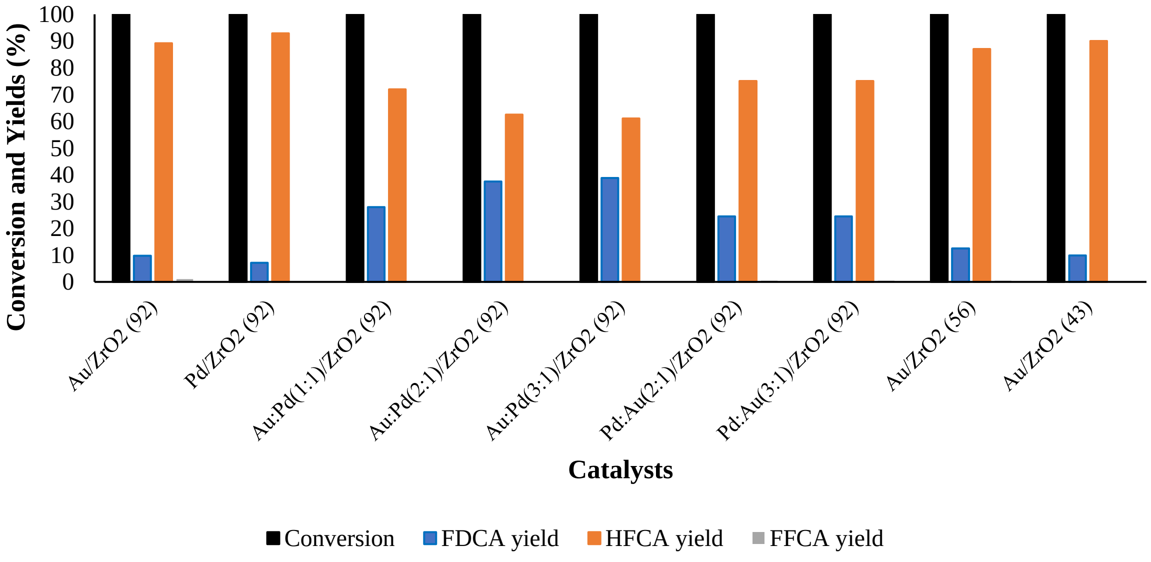

Figure 89. Screening of catalysts in HMF oxidation to FDCA in SPR reactor. Reaction conditions: 20 bar of air; T=50 °C; t=2h; stirring rate= 600 rpm; NaOH:HMF=3:1 molar ratio.

In general, we can see a similar trend to that of the reaction at 110 °C. Also in this case the conversion was complete after two hours of reaction. Bimetallic catalysts were the most active catalysts in the reaction, with an FDCA yield of 28 to 39%. Also in this case the catalysts Au:Pd(3:1) ZrO_2 (61192) and Au:Pd(2:1) ZrO_2 (61192) were the most selective towards the formation of FDCA and with very similar catalytic performances, as found for the reaction at 110 °C, with FDCA yields of 39 and 38% respectively. These very similar catalytic performances can be explained by examining the quantity in mg of the two metals with the different molar ratios. From Figure 90 we can see that we have a similar loading in weight for Au:Pd (3:1) and Au:Pd(2:1) of Au (8.2 mg and 7.8 mg respectively) and Pd (1.8 mg and 2.2 mg respectively), differences which increase considerably for the other molar ratios.

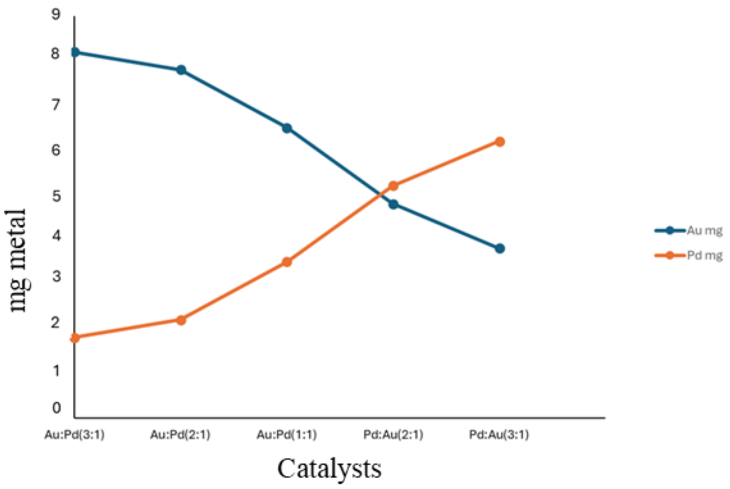

Figure 90. Quantity (in mg) of Au and Pd in bimetallic synthesized catalysts

Focusing on the selectivity towards the FDCA and HFCA for the two reactions at 50 (orange curve) and 110 °C (blue curve) in Figure 91 for the bimetallic catalysts, we can see that there is a similar trend of a volcano plot: increasing the amount of gold, therefore increasing the Au:Pd molar ratio, selectivity towards FDCA increased, while selectivity towards HFCA decreased. Conversely, lowering the Au:Pd molar ratio and therefore decreasing the quantity of gold has an effect to decrease the selectivity for FDCA. We see that the increase in selectivity of FDCA by increasing the Au:Pd ratio was significant at higher temperatures (110 °C) than at 50°C (Figure 91). The catalytic trends were very similar for both temperatures: in general, a higher temperature favoured the oxidation reaction to FDCA in agreement with literature.

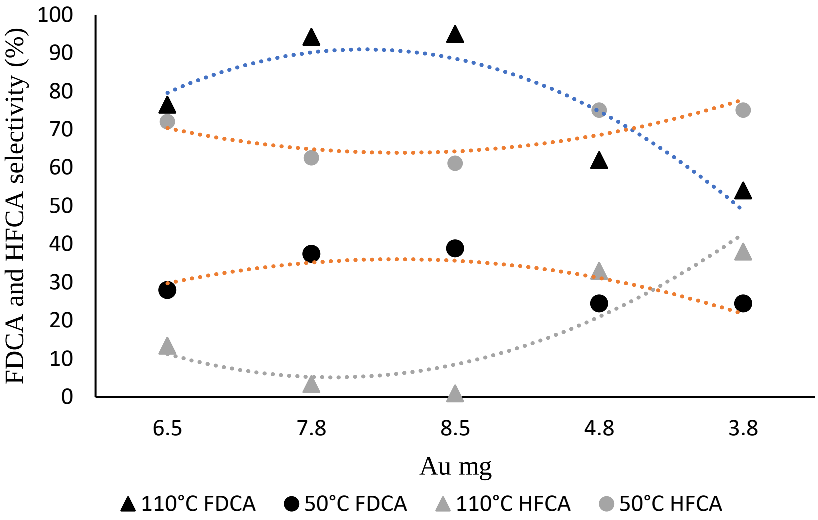

Figure 91. FDCA and HFCA selectivity for bimetallic catalysts is HMF oxidation at reaction temperature of 50 °C and 110 °C Reaction conditions: 20 bar of air; t=2h; stirring rate= 600 rpm; NaOH:HMF=3:1 molar ratio

Catalytic testing at room temperature

We proceeded by testing the same catalysts in an autoclave-type reactor. It was decided to carry out the reaction at room temperature (T=25°C), using pure oxygen instead of air as the oxidizing gas. In particular, air is composed of 20.9% oxygen. Consequently, a reaction carried out at 20 bars of air corresponds to approximately 4 bars of pure oxygen. The autoclave was loaded with 8 bars of pure oxygen, therefore corresponding to approximately 40 bars of air. The catalytic results obtained are shown in Figure 92.

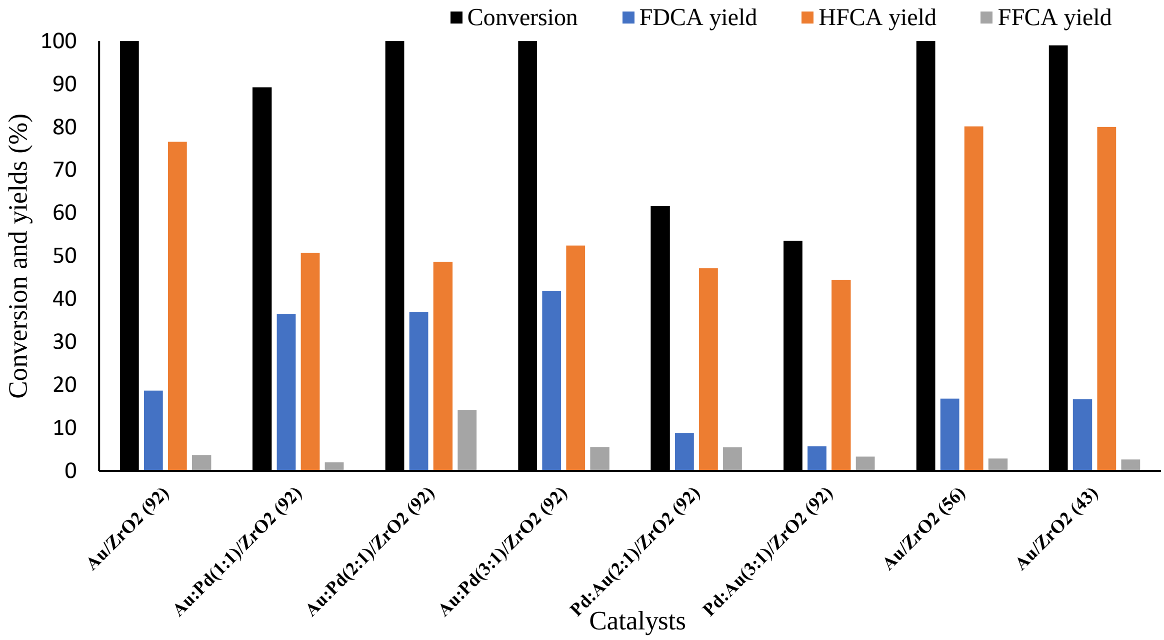

Figure 92. Screening of catalysts in autoclave reactor for HMF oxidation to FDCA. Reaction conditions: 8 bar of O_2; T=ambient(25°C); t=2h; stirring rate= 600 rpm; NaOH:HMF=3:1 molar ratio

The catalytic results show that the trend is very similar to the results seen previously. Focusing on monometallic catalysts, Au/ZrO_2 (92) was the most active, with an FDCA yield of 19%. Among the bimetallic catalysts, Au:Pd (3:1) was the most active, with a yield of 42%. These results are prosiming, because we manage to reach a good yield of FDCA in just two hours of reaction and at a relative low pressure of O_2, in comparison with other work were the pressure was higher (20 bar, 18 h for 71 % of yield using Gold-based catalyst) [152] and time of reaction longer (t=22 h; PO_2=4 bar; yield of FDCA= 69 % using Au/TiO_2 catalyst [153]. Considering that we don't have the same conversion for all the bimetallic catalysts, it's necessary to compare both the selectivities and the yields to study the bimetallic catalysts. Regarding the selectivities (Figure 93), we see that as the quantity of Pd increases (corresponding to the decrease in the quantity of Au), the selectivity towards FDCA decreased and that towards HFCA increased, as seen in the SPR reactor. Instead, comparing the yields, a decrease in the quantity of Au (and increase in the quantity of Pd) generates a decrease in FDCA yield, while the HFCA yield remains constant. Indeed, increasing the quantity of Pd a decrease in conversion is seen.

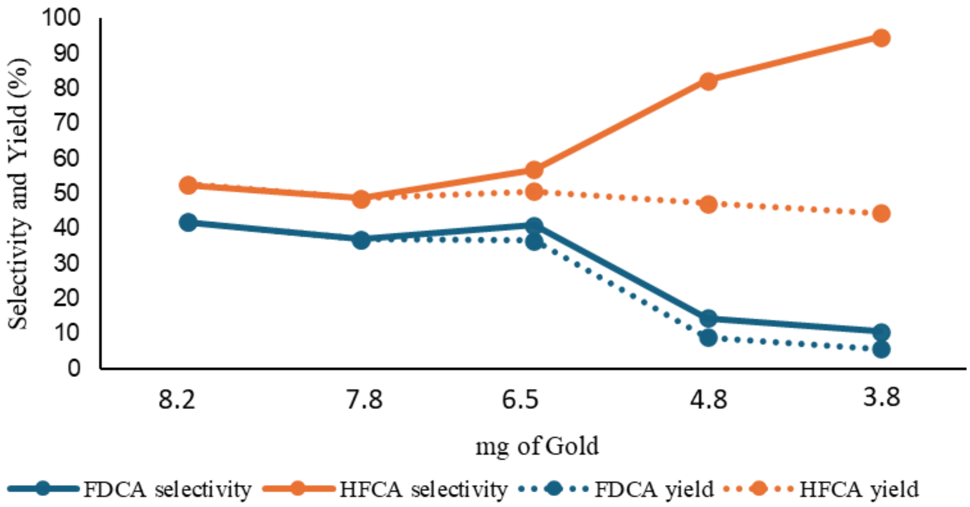

Figure 93. Selectivity for FDCA and HFCA for bimetallic catalysts in HMF oxidation

4.4.2 HMF oxidation in liquid phase: Au:Pd(3:1)/ZrO_2 (61192) as catalyst

Considering the catalytic results obtained during the screening phase, for subsequent tests in the autoclave-type reactor we focused on the catalyst that gave the best catalytic performance, therefore the chosen catalyst was: Au:Pd (3:1)/ZrO_2 (61192).

4.4.2.1 Optimization of reaction parameters

Quantity of catalyst

We proceeded first by evaluating the effect of the mass of the catalyst, in order to exclude possible external diffusion phenomena. The results obtained by varying the catalyst mass while keeping the other parameters constant (PO_2=8 bar; T=amb) are shown in Figure 94.

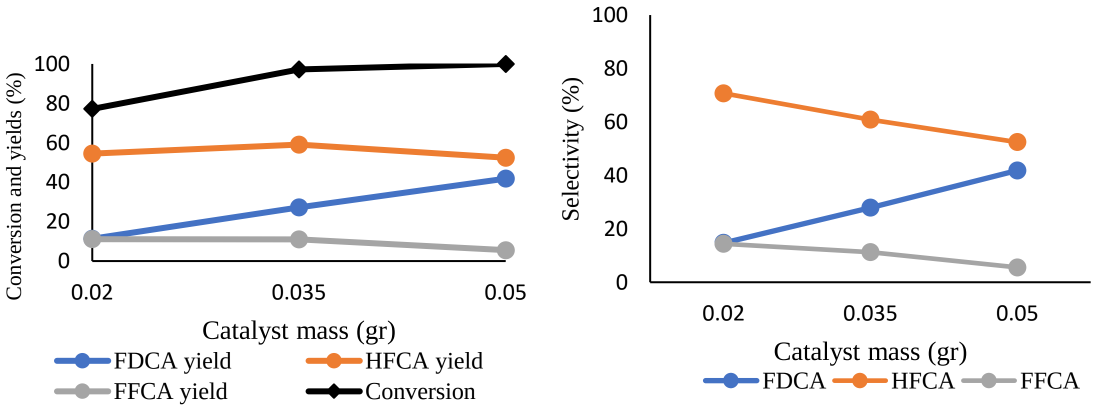

Figure 94. Conversion and Yields (graph on the left) and Selectivities (graph on the right) for HMF oxidation using Au:Pd (3:1)/ZrO_2 (61192) as catalyst. Reaction conditions: 8 bar of O_2; T=amb; t=2h; stirring rate= 600 rpm; NaOH:HMF=3:1 molar ratio

By increasing the mass of the catalyst, the conversion increased: in particular, already with a mass of 0.035 g there was an almost complete conversion, of 97.5%, which was then complete using a catalyst mass of 0.05 g. The linear increase in conversion indicates that there are no apparent diffusion limitations. By further increasing the catalyst mass up to 0.06 g, it is seen that the conversion tends to no longer increase linearly, indicating that limitations due to external diffusion phenomena are present. However, due to the high level of conversion produced at 0.035 and 0.05, it is more evident to make the comparison following the increase of selectivity of intermediates. The main products were FDCA, HFCA and FFCA. We see that as the mass of the catalyst increased, the selectivity for FDCA, the desired product, increased linearly, with a selectivity of 42% using 0.05 g of catalyst. At the same time, the selectivity towards the reaction intermediates, HFCA and FFCA, decreased, where the selectivity using 0.05 g of catalyst is 52.4% and 5.6% respectively. It can be deduced that with a mass of 0.05 g of catalyst we are in a kinetic regime and there are no limitations from external diffusion; consequently, since at this value there is also the highest conversion and the highest yield in FDCA, for subsequent experiments 0.05 g was used as the standard mass of the catalyst.

Effect of stirring rate

Subsequently, the effect of the stirring rate was investigated under the same reaction conditions (T=amb; PO_2=8bar; t=2h) in order to make sure that we are working in a kinetic regime and exclude possible external diffusion phenomena. To do this it is necessary to evaluate whether there are any weaknesses to mass transfer (external diffusion). The results at different stirring rate are shown in Figure 95.

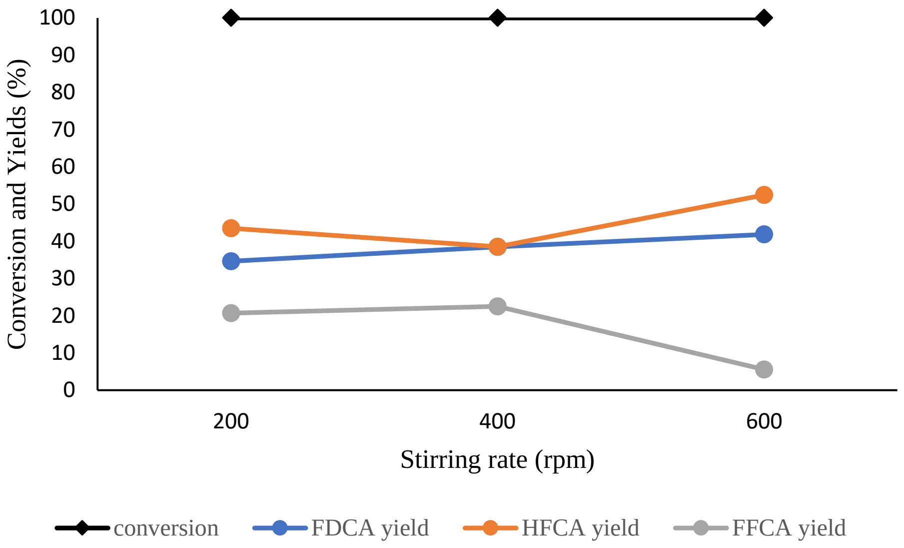

Figure 95. Catalytic results for HMF oxidation using Au:Pd (3:1)/ZrO_2 (61192) as catalyst at different stirring rate. Reaction conditions: 8 bar of O_2; T=amb; t=2h; stirring rate= 200-400-600 rpm; NaOH:HMF=3:1 molar ratio

From the results obtained it can be seen that for all the different stirring rates we have a total conversion of HMF, so we can not make a direct conclusion for the effect of stirring. Moreover, considering the Yields of the different products, we can see that at 600 rpm we have the maximum yield of FDCA (52.4%), the desired product and the minimum formation of FFCA (5.6%). Considering the total sum of the two by products/intermediates of the reactions (HFCA and FFCA), we have the smaller formation of them at 600 rpm (sum of Yields of HFCA and FFCA= 47.6%). In conclusion, at higher stirring rate we have the best catalytic performance. For this reason, for the next studies we have decided to consider 600 rpm as standard. Higher stirring rates should be tested in the future, to evaluate the effect of the selectivity of the reaction in question.

Effect of reaction time

Time on line analysis as a function of reaction time was carried out. In particular, tests were carried out with reaction times from 30 min to 2 h. The results obtained keeping the other reaction parameters unchanged (T=ambient; PO_2=8 bar; g catalyst: 0.05 gr) are reported in Figure 96.

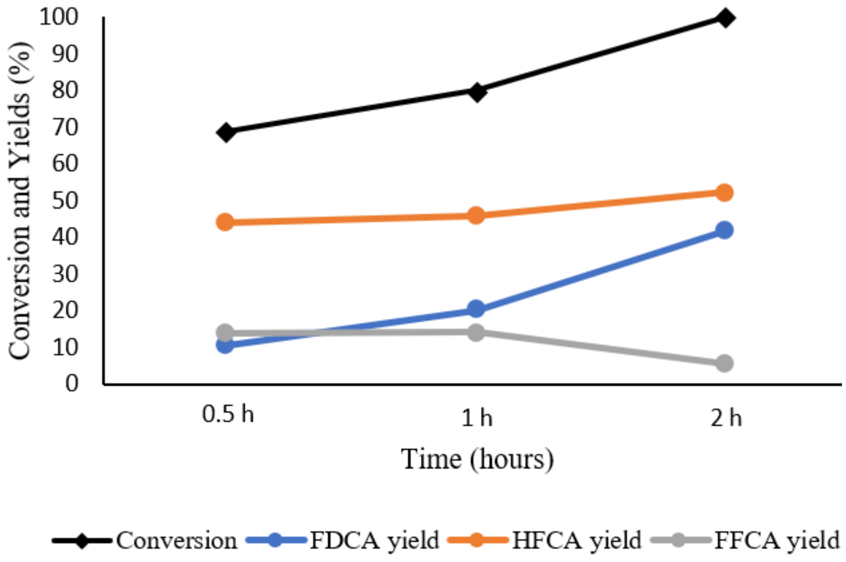

Figure 96. Catalytic results for HMF oxidation using Au:Pd (3:1)/ZrO_2 (61192) as catalyst at different times. Reaction conditions: 8 bar of O_2; T=ambient; t=0.5-1-2h; stirring rate= 600 rpm; NaOH:HMF=3:1 molar ratio

Increasing the time up to 2 hours the yields of FDCA increased almost linearly, varying from a yield of 12% for half an hour of reaction to 20% at one hour of reaction and to 42% at two hours of reaction. At the same time, the yield of FFCA decrease, varying from 14% at half an hour and one hour of reaction to 6% at two hours of reactions. The yield of HFCA was quite constant over time, with values of 44, 46 and 52% respectively at half an hour, 1 hour and two hours of reaction. This result indicates that as the reaction time increases, the oxidation step from FFCA to FDCA was favored, since the yield of the latter increased at the expense of FFCA in agreement with literature.

4.4.2.2 Catalyst characterization

For the characterization we focused on the Au:Pd(3:1)/ZrO_2 (61192) catalyst, which was found to be the most active in the oxidation reaction of HMF to FDCA.

Regarding the characterization of the support, this has already been carried out and presented in the chapter on the hydrogenation of furfural. We therefore focused on characterization techniques necessary to study the morphology of the supported nanoparticles. In particular, through TEM analysis to evaluate the degree of dispersion, structure and size of the nanoparticles, in order to evaluate the degree of oxidation of Pd and Au and surface content of the metals.

Characterization: TEM analysis

TEM-EDX analysis was carried out in order to evaluate the degree of dispersion of the Au and Pd nanoparticles, to better understand the structure of the bimetallic nanoparticles and to calculate the dimensions of them. Figure 97 shows the STEM images and TEM-EDX images of the Au:Pd (3:1)/ZrO_2 (61192) catalyst.

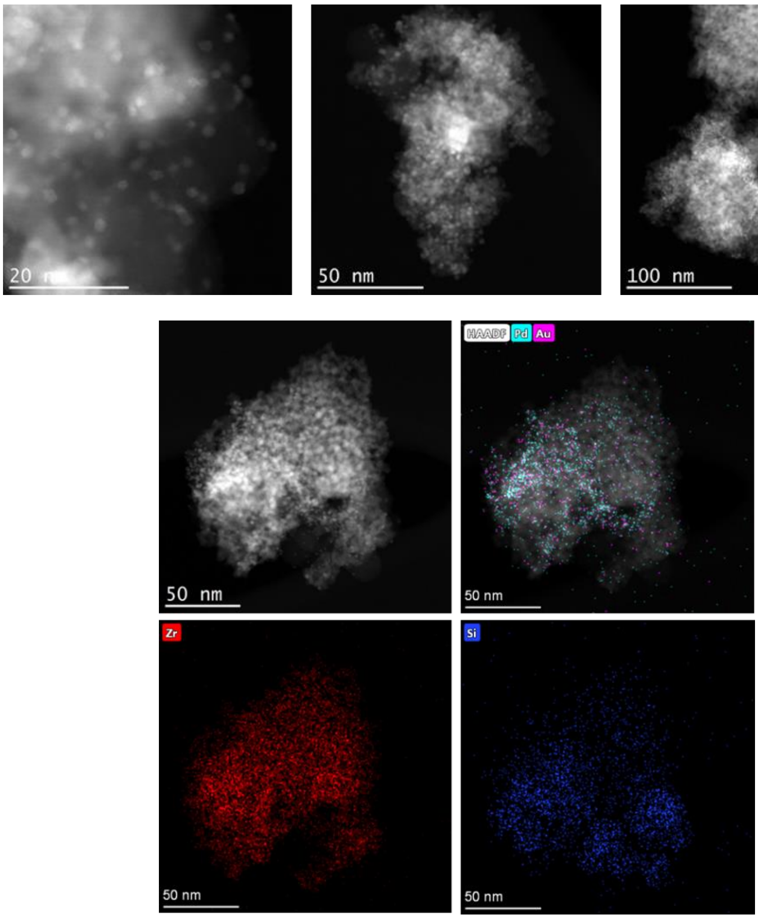

Figure 97. STEM and TEM-EDX images for Au:Pd (3:1)/ZrO_2 (61192) catalyst

From STEM-EDX mapping, it can be seen that Pd and Au amounts are preferentially arranged in the areas where ZrO_2 is present rather than where SiO_2 is present. We also see that the Au-Pd nanoparticles have an alloy structure and are well dispersed.

Figure 98 shows another STEM and TEM-EDX images of the same sample.

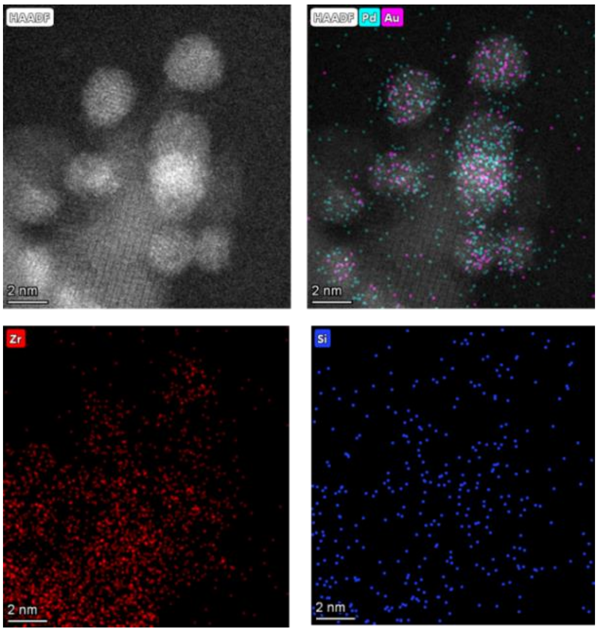

Figure 98. STEM and TEM-EDX images for Au:Pd (3:1)/ZrO_2 (61192) catalyst

In this case we observe that the Pd-Au nanoparticles are well dispersed and in the form of an alloy. Also in this case we observe that the nanoparticles tend to deposit preferentially on the zirconia structure compared to that of SiO_2.

The particle size distribution of the Au-Pd nanoparticles, is shown in Figure 99. It has been calculated from different STEM images, analysing more than 150 nanoparticles.

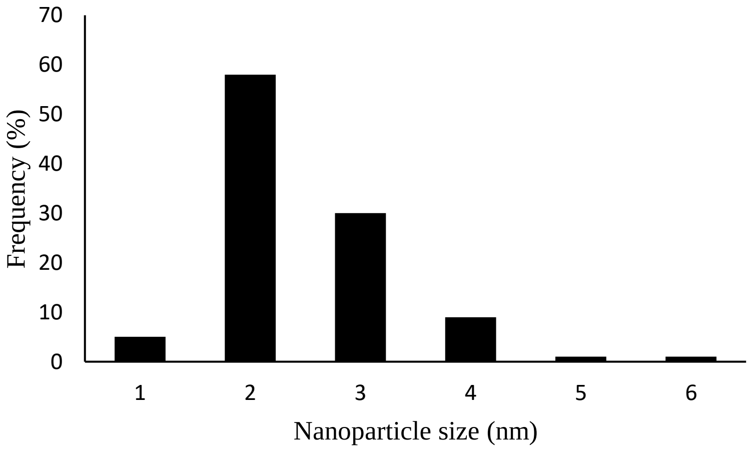

Figure 99. Nanoparticles distribution for Au:Pd (3:1)/ZrO_2 (61192) catalyst

In general, Au-Pd nanoparticles have a particle size around 2-3 nm. The average particle size is 2.4±0.7 nm. It can be concluded that small-sized, regular and well-dispersed nanoparticles with an Au-Pd alloy structure were obtained with the optimized sol-immobilization synthesis method.

4.5 Conclusions and future work

Various mono- and bimetallic catalysts supported on zirconia supports have been synthesized using the sol-immobilization technique for the oxidation reaction of HMF to FDCA. Most of these studied catalysts have already been tested for the CTH reaction of furfural.

A screening of these catalysts in the SPR reactor in the reaction in question was carried out, using air as oxidizing agent. In particular, the catalysts were tested at two different temperatures, 50°C and 110°C. From the results obtained, bimetallic catalysts resulted to be the most active and selective for the formation of FDCA. In particular, the Au:Pd (3:1)/ZrO_2 (61192) catalyst showed the best catalytic performance, with total conversion of HMF and selectivity in FDCA of 95% at 110°C and 39% at 50 °C respectively. Starting from the results obtained, it was decided to optimize the reaction parameters using the Au:Pd (3:1)/ZrO_2 (61192) catalyst in an autoclave-type reactor, using pure oxygen as an oxidizing agent (8 bar) and carrying out the reaction at room temperature. Under optimized reaction conditions (t=2h; T=amb; PO_2=8bar; rpm=600; molar ratio NaOH:HMF=3:1) a total conversion of HMF was obtained, with a FDCA yield of 52%.

From the TEM-EDX analysis of the synthesized catalyst Au:Pd (3:1)/ZrO_2 (61192 it was seen that the sol-immobilization technique is effective for the synthesis of bimetallic catalysts: in fact, the nanoparticles are well dispersed and small in size, with average values of 2.4±0.7 nm; with the synthesis method used, a random distribution of gold and palladium nanoparticles was obtained, with an alloy structure.

In future work subsequent autoclave tests will be necessary, in order to further optimize the reaction parameters, to increase the selectivity in FDCA. In particular, the effect of temperature, NaOH:HMF ratio, oxygen pressure and reaction time must be evaluated. Reusability tests have to be carried out, in order to evaluate the activity of the catalyst after several reactive cycles. Furthermore, characterizations of spent catalysts are necessary in order to better understand possible deactivation phenomena.

5. Glucose oxidation: a computational study

5.1 Introduction

5.1.1 Glucaric acid: an interesting platform molecule

Between the 12 top value-added chemicals that can be obtained starting from biomass there is glucaric acid (GLA). GLA also known as saccharic acid, is a polyhydroxy dicarboxylic acid obtained from the oxidation of glucose (GLU). The mechanism consists of two main steps, as shown in Figure 100. The first step of the reaction involves the selective oxidation of glucose to gluconic acid (GLO). Subsequently, in the second step the oxidation of the terminal alkoxide group to a carboxyl group occurs, obtaining the GLA product.

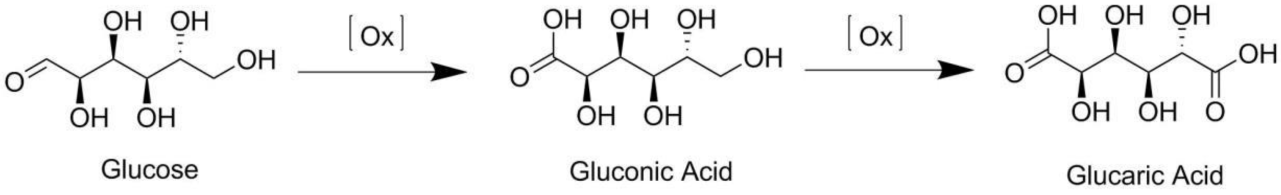

Figure 100. Mechanism of oxidation of Glucose to Glucaric Acid

Glucaric acid has nowadays acquired great importance on an industrial level thanks to its vast fields of application and use: it can be used as a chelating agent and therefore a sequestering agent for the production of detergents [154]: the gluconate ion, in fact, having a net negative charge, can be used as a chelating agent for metals such as Ca^{2+}, Fe^{2+} and Al^{3+}. GLA can also be used to inhibit metal corrosion [155] and in the pharmaceutical and food industry, for example as a regulator of cholesterol levels [156]. Its main use, however, is in the field of the production of elastomers and polyesters: it can in fact be reduced to adipic acid, the monomer of nylon-6,6. This would allow adipic acid to be obtained starting from raw materials from natural sources, resulting in a valid and sustainable alternative to the normal use of derivatives from fossil-based benzene.

5.1.2 Glucaric acid production

At an industrial level, glucaric acid is nowadays mainly obtained according to the Sohst-Tollens process, where nitric acid is used both as an oxidizing agent and as a solvent [157]. Although it is a very simple process, it has several problems from both an environmental and economic point of view: nitric acid produces NO_x, which have been classified as air pollutants.

Furthermore, due to the use of nitric acid, it is necessary to use specific and more expensive materials for the structure of the plant, capable of resisting the oxidation action of the acid.

Several alternative methods to the use of nitric acid have been proposed to produce GLA starting from GLU. These include electrochemical and biocatalytic methods. Among the electrochemical methods there is the use of MnO_2 nanoparticles deposited on titanium as an anode and on metal mesh as a cathode. [158] This method showed excellent performance from a catalytic point of view, with a high yield of GLA (about 84%) and mild reaction conditions, avoiding the use of an oxidizing agent. However, currently the construction of an electrocatalytic system is still very expensive, especially for the scale up. Among the proposed biochemical methods there is the use of recombinant Escherichia Coli [159] as an oxidizing agent, which allows maintaining mild reaction conditions. However, this process, in addition to being economically expensive, is not particularly selective to produce GLA, with a yield of only 17%.

Research in recent years has focused on the use of metal nanoparticles deposited on supports for the catalytic oxidation of GLU to GLA, using oxygen as an oxidizing agent. The use of heterogeneous catalysts offers the advantage of being able to easily separate the catalysts at the end of the reaction and reuse them, with very low separation costs.

For the oxidation of GLU, the use of various metals in nanoparticle form has been proposed, such as Au, Pt, Pd etc. It was decided to focus attention on the use of gold, a metal that is particularly effective in oxidation reactions and is not subject to major leaching and poisoning phenomena, unlike other metals such as Pd and Pt.

5.1.3 Glucose oxidation to glucaric acid using gold supported nanoparticles: a previous work

In work previously carried out by the research group in Bologna [160], catalysts based on gold nanoparticles supported on activated carbon (AC) were studied, obtained through the sol-immobilization technique, reported in the previous chapters for the synthesis of other materials presented in this thesis.

In particular, in the work that had been initiated by Eleonora Monti and later it was continued by coworkers, we focused on the effect of the stabilizing agent in the reaction, especially the effect of the stabilizer on the structural properties of the catalysts and how the different structural properties can influence the catalytic performance. In this chapter we present and summarise the main findings since part of these results have been published in a previous PhD thesis. The focus on this chapter is to correlate the experimental data with the computational data, which is the main novelty of the PhD student, Alessia Ventimiglia. In fact, three main stabilizing agents were tested: PVA, PVP and PEG (polyvinylalcohol, polyvinylpyrrolidone, polyethylene glycol), and the effect of these polymers was evaluated as a function of the weight ratio with gold. The choice of the stabilizers was based on studying the effect of the steric and electronic properties the stabilizers possess.

The synthesis procedure of the catalysts consists of dissolving 0.0209 g of $HAuCl_4 * H_2O$ in 385 mL of distilled water in a beaker. After that, the desired volume of stabilizing agent (PVA, PEG and PVP) previously dissolved in distilled water (0.1010 g in 10 mL of distilled water) iwas added. After 3 minutes from the addition of the stabilizing agent, the reducing agent was added, i.e. $NaBH_4$ (0.0096 g in 2.5 mL of distilled water; $NaBH_4$: Au = 5:1 molar ratio). After half an hour, the support was added, 0.99 g of AC. The suspension was acidified with H_2SO_4 to a pH=2, below the isoelectric point of AC and left under stirring for one hour. Finally, at the end of the synthesis, after having filtered and washed the catalyst with approximately 1 L of water to remove impurities, it was left to air dry overnight and finally in an oven for 4 hours at 80 °C, in order to remove all the physisorbed water.

The oxidation reaction was carried out in a batch autoclave reactor (Figure 101) with a capacity of 50 mL, using oxygen as oxidant agent.

Figure 101. Autoclave reactor used for glucose oxidation.

The typical experimental procedure was the following: An aqueous solution was prepared by adding 0.7895 g of glucose (0.29 M) in 15 mL of distilled water; then, NaOH was added to obtain a molar ratio GLU:NaOH = 1:3; finally, 0.0087 g of catalyst was added. A magnetic stir bar was added and the reactor was closed, then purged with O_2 three times and finally pressurized with O_2 at 10 bar. The reactor was placed on a heating mantle, set at a temperature of 60 °C, measuring the temperature with a thermocouple. The reaction was conducted for the desired time, counting t= 0 from the moment that the thermocouple reads T= 60° C. At the end of the reaction, the autoclave was placed in an ice bath to cool down quickly, then depressurized and opened. The post-reaction mixture was centrifuged for 15 min at 4500 rpm, the catalyst was separated, while the liquid part was filtered with a syringe filter with 45 μm porosity and the volume of the final solution was measured. The post reaction mixture was analysed by high-performance liquid chromatography (HPLC), in order to identify the products obtained and quantify them. Two Rezex ROA-H $^+$ (8%) 300 × 7.8 mm ion exclusion columns were used in series to best separate all reactant and product peaks. Quantification of products was done based on external calibration methods of commercial standards.

The results obtained with the catalysts synthesized with different stabilizing agents and with different Polymer to Au weight ratio in standard reaction conditions (t=1h; T=60 °C; stirring rate: 1000 rpm; PO_2=10 bar) are reported in Table 18.

Table 18. Catalytic results using different stabilizing agents and different polymer:Au weight ratio[166]

	Polymer:Au weight ratio	Conversion (%)	Gluconic Acid Yield (%)	Glucaric Acid Yield (%)	Others Yield (%)
PVA	0.3	89	38	22	30
	0.6	90	38	22	30
	1.2	90	40	20	28
	2.4	89	44	17	26
PEG	0.3	88	77	4	4
	0.6	96	32	20	48
	1.2	90	72	3	19
	2.4	88	87	3	9
PVP	0.3	93	42	20	30
	0.6	90	38	20	30
	1.2	92	51	16	26
	2.4	92	51	16	23

The best catalytic performances were obtained using PVA as a stabilizing agent with the highest yield in GLA around 22% with low PVA:Au weight ratios, which decreased up to 17% as the PVA:Au ratio was further increased. Using PEG as the choice of stabilizer showed the worst catalytic performances, with GLA yields around 3-4%, with the exception of the PEG:Au weight ratio of 0.6, where the GLA yield was 20%. When PVP was used, the GLA yields were around 20% for low PVP:Au weight ratios, which decreased further to 16% at higher ratios, probably due to the blocking of the catalytic sites by the increase amount of the stabilizing agent, which thus tends to block the reactive step from GLO to GLA.

From the results obtained it can be deduced that the choice of the stabilizing agent and the relationship with the metal has a fundamental role in the catalytic performance of the material, since it plays an important effect (i) on the size of the nanoparticles and (ii) on the exposure of the catalytic sites, which can be covered from the polymer itself and block the reaction in question. In fact, at high weight ratios of stabilizing agent:Au, a general decrease in catalytic performance was observed, in particular for the oxidation step from gluconic acid to glucaric acid.

Study of reaction parameters: reaction time

In the study carried out by the research group, other reactive parameters were evaluated, including the reaction time. In particular, the reaction was carried out at different times (time of reaction: 15 minutes, 1 hour and 2 hours) using PVA: Au=0.6 weight ratio as the reference catalyst, showing promising catalytic performance. The catalytic results are shown in Figure 102

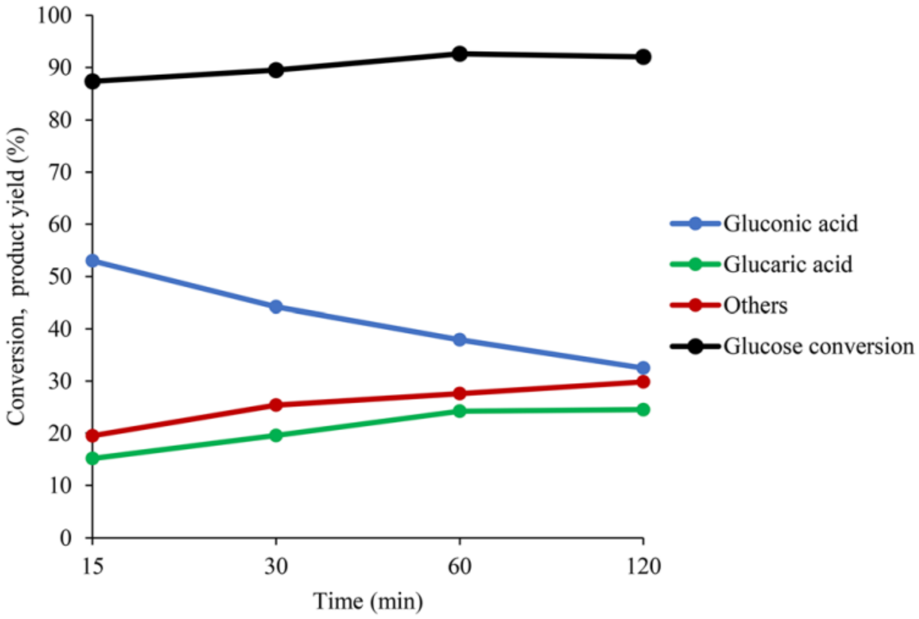

Figure 102. GLU conversion and formation of GLO, GLA and byproducts as a function of reaction time. Reaction conditions: 60 °C, 1000 rpm, 10 bar O_2, GLU : Au : NaOH molar ratio of 1000 : 1 : 3000.

The conversion of GLU increased as the reaction time increased up to one hour, with an increasing in GLA and Others yields; The yield of GLO decreased during the first hour of reaction; after one hour of reaction the yield of GLA and other by product follow a different trend: both the yields increased with increasing reaction time up to one hour, but after one hour the GLA yield did not increase but remained constant and the yield of others decreased slightly. The obtained results suggest a possible catalyst deactivation due to GLA or other byproducts. For this reason, it was decided to carry out a computational study, analyzing the adsorption energies of the main molecules involved in the reaction, in order to understand which could be the one that leads to a deactivation of the catalyst.

5.2 Scope

In this work we focused on evaluating the catalytic deactivation phenomena through a computational approach, studying the catalyst-adsorbate interaction of the main reactants and products of the reaction, in order to evaluate the adsorption energies and geometries. We then proceeded by studying, again using a computational approach, the interaction between the gold nanoparticle and the three stabilizing agents PVA, PEG and PVP.

5.3 Computational study details

A DFT study was then carried out, using the Gaussian 16 software [83]. Au nanoparticles of small dimensions have been modeled using the "cluster approach": in particular, as starting structures, five amorphous Au_{55} structures previously modeled and optimized at the density functional tight-binding theory (DFT-B) level were used, re-optimising them at the DFT level using the B3LYP functional[71-75] and the Stuttgart ECPs[77] as the basis set for the gold atoms. Once these structures were optimized, we proceeded to study the adsorption of various molecules on the most stable one, in order to evaluate the adsorbate-catalyst interactions. For the atoms of the adsorbates (H, C, N and O) the 6-31G** basis set was used [73-76] and the final energies were evaluated using a larger basis set for the lighter atoms, 6- 311++G**. All calculations were carried out in vacuum and to calculate the final energies the counterpoise correction was applied in order to account for the basis set superposition error. Density of electronic states (DOS) have been computed using the program Multifwn.

5.4 Results

5.4.1 Modelling of clusters

To model gold nanoparticle structures, we focused on stable, small clusters, in particular those with 55 Au atoms. This choice is based on various reasons: first of all, because of computational cost, since gold has atomic number = 79, modeling large structures would have required a lot of calculation time. Furthermore, a gold structure of 55 atoms has almost the size of 1 nm, therefore, not too far from the nanoparticles synthesized in the laboratory (around 2-3 nm). Such small structures also appear to have a high exposed surface area, with numerous defects, therefore suitable for realistically studying the adsorption of small molecules. Furthermore, the number “55” for metal clusters is generally a “magic” number, since it brings a symmetric structure with a high state of degeneracy and stability, for example for Au and Cu clusters [161-162].

Regarding gold clusters, using photoelectron spectroscopy and DFT calculations [163] it was discovered that structures of this size (with atoms from 53 to 65) appear to have an irregular structure, due to relativistic effects. We then proceeded by re-optimising at the DFT level five structures previously optimized at the DFT-B level by Van den Bossche et al. [164] The structures were indicated as Sn, where n=1,2,..,5 and are shown in Figure 103. The energy difference compared to the most stable structure (S3) is reported in kcal/mol.

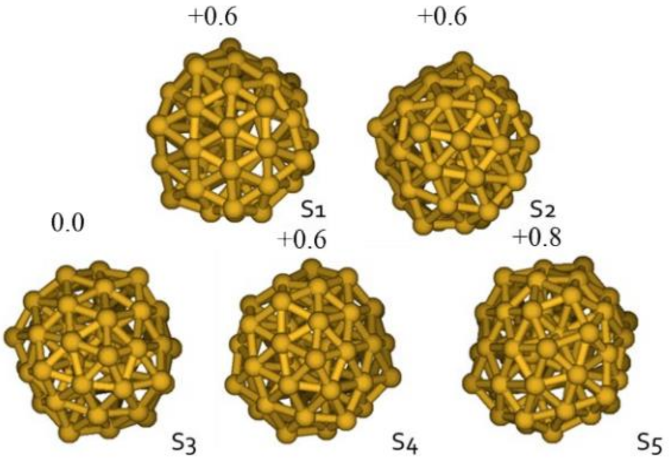

Figure 103. Five amorphous Au_{55} structures after optimisation at DFT level

As can be seen from the values obtained, the five structures are almost degenerate in energy, with a maximum ΔE of 0.8 kcal/mol.

Figure 104 shows the DOS of the five structures. As can be seen, the electronic structure of all five is very similar, and consequently there is not preference of one structure over the other for the subsequent study.

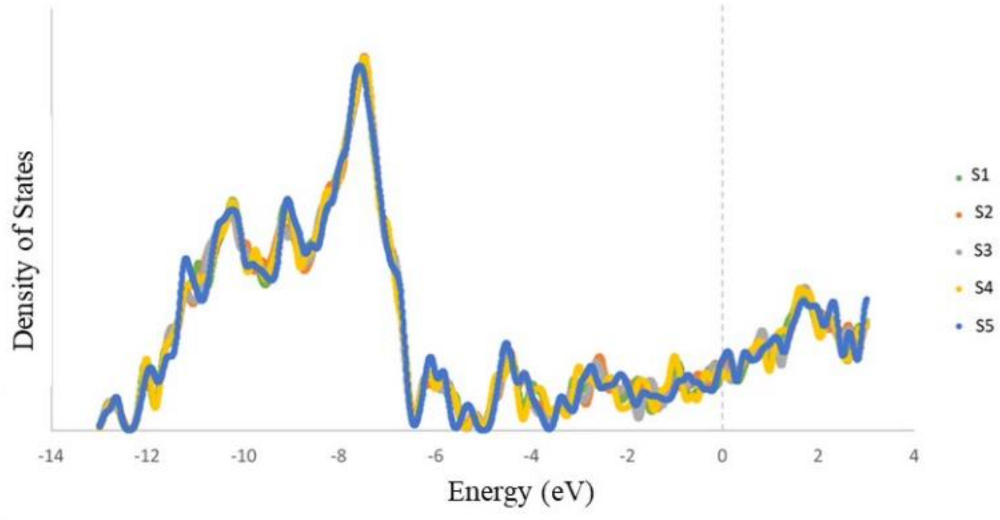

Figure 104. Overlapped DOS of Au_{55} clusters after DFT optimisation

It was decided to focus on the most stable structure from an energetic point of view, S3, to carry out subsequent adsorption studies. As catalytic site, we focused on the one with the lowest coordination, following the starting idea that an under-coordinated site is also the most reactive one. Some target molecules were adsorbed onto this site: GLU, the starting reagent; GLO, the main reaction intermediate; GLA, the main reaction product.

5.4.2 Study of deactivation phenomena: adsorption of target molecules

To study the adsorption of reaction target molecules, two main approaches were followed:

- Study of isolated molecules on clean clusters
- Study of molecules on clusters with hydroxyl groups

The surface of the catalyst is in fact rich in hydroxyl groups, as the reaction takes place in a basic environment due to the use of NaOH. We therefore wanted to evaluate the effect of these groups on the catalyst deactivation phenomena.

Study of isolated molecules on clean clusters

For the study of isolated molecules, without the presence of OH^- groups, as previously mentioned, GLU, GLO and GLA were made to adsorb on the surface of the catalyst, on the most under-coordinated site. The adsorption energy ($Eads_{NP}$) was then calculated according to the following formula and reported in Tabel 19:

$$Eads_{NP} = E_{Au_{55}+ads} - (E_{Au_{55}} + E_{ads})$$

The structures obtained after the optimization are shown in Figure 105, while the adsorption energies are reported in Table 18.

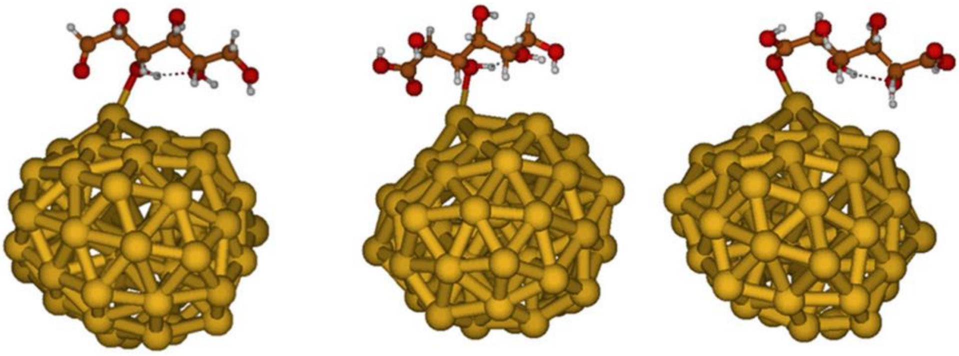

Figure 105. Adsorption of GLU (left), GLO (center) and GLA (right) on Au_{55} cluster after DFT optimisation

Table 19. Energies of adsorption of GLU, GLO and GLA on S3 Au_{55} cluster after DFT optimization

	Adsorption energy (kcal/mol)
Glu on S3	-10.5
Glo on S3	-12.0
Gla on S3	-12.6

From the adsorption energies it can be seen that the intermediate GLO and the product GLA adsorb on the catalytic surface slightly more strongly than GLU. However, such a minimal difference cannot clarify which molecule can cause the catalyst deactivation.

Examining Figure 105 an intramolecular bond is identified for all three molecules: this result can lead us to conclude that no other specific intramolecular interactions are generated by the catalyst-adsorbate interaction, which could be the cause of a different adsorption.

Given the results obtained, it was therefore decided to proceed by considering the effect of the basic environment on the adsorption of the molecules on the catalytic surface.

Study of molecules on clusters with hydroxyl groups

For the study of adsorbates in the presence of hydroxyls it was decided to add two hydroxyl groups: this is due to the fact that, during the reaction of oxidation from glucose to gluconic acid and then glucaric acid, the changing in the structure of the molecules is mainly visible in the two terminal groups, which are progressive oxidized. Consequently, a different adsorption can be explained by the interaction with these two groups, and therefore by the interaction with two hydroxyl groups.

The structures were optimized at the DFT level and are shown in Figure 106.

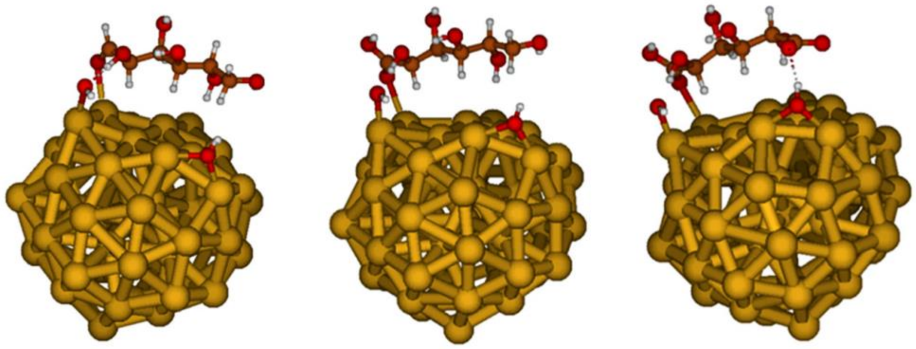

Figure 106. Adsorption of GLU (left), GLO (center) and GLA (right) on Au_{55} cluster with OH^- groups.

The adsorption energies ($Eads_{NP+2OH^-}$) were calculated according to the following equation and reported in Table 20.

$$Eads_{NP+2OH^-} = E_{Au_{55}+ads+2OH^-} - (E_{Au_{55}+2OH^-} + E_{ads})$$

Table 20. Adsorption energy in kcal/mol of GLU, GLO and GLA, on S3 Au_{55} cluster in presence of 2 OH^- groups.

	Adsorption energy (kcal/mol)
Glu on S3 + 2OH$^-$	-31.2
Glo on S3 + 2OH$^-$	-40.7
Gla on S3 + 2OH$^-$	**-44.3**

From the adsorption energies we can see a substantial difference between the three molecules: GLO and GLA adsorb much more strongly than GLU. In particular, GLA is the one with a highest adsorption energy, with a difference of 3.6 kcal/mol compared to GLO and 13.1 kcal/mol compared to GLU.

The presence of hydroxyl groups on the surface of the catalyst modifies the adsorption geometry: first of all, we see that the O-Au bond is this time shorter for GLO and GLA (2.50 Å) compared to GLU (2.54 Å), explaining the higher energy adsorption of GLO and GLA compared to GLU. Furthermore, GLA is further stabilized thanks to the hydrogen-type interaction between the oxygen of the new carboxyl group formed and the hydrogen of an hydroxyl group on the surface of the catalyst, further increasing its adsorption energy.

In conclusion, from the computational study, we can conclude that GLA adsorbs more strongly on the surface of gold nanoparticles compared to GLU and GLO. This is due to the intermolecular hydrogen-type interactions with the hydroxyl groups present on the surface of the catalyst, interactions which occur through the extra carboxylic acid group present in the GLA molecule; these interactions tend to stabilize the molecule on the catalytic surface, leading to possible phenomena of catalyst deactivation during the reaction.

5.4.3 Study of interaction of stabilising agent and gold nanoparticles

The stabilising agent plays a fundamental role on the catalytic activity of a material. This is because it can interact with the molecules of the reactants and products, modifying the catalytic activity, but also because, being large polymeric molecules, it can block the catalytic sites and lower their activity. Consequently, for a stabilizing agent to best perform its task, it must keep the nanoparticles separated during the synthesis phase, but then be easily removed before its use in the reaction.

In order to better understand the interactions between gold nanoparticles and some stabilizing agents, their interaction was studied computationally on the same Au_{55} S3 gold structure described above. In particular, we focused on three commonly used stabilizing agents: Polyvinyl alcohol (PVA) (used for the synthesis of materials in this work), Polyethylene glycol (PEG) and Polyvinyl pyrrolidone (PVP).

To study interaction of these polymers with the gold cluster, the adsorption of their monomeric units was considered in order to lower the computational cost. To create the initial structures, the same catalytic site as in the previous study was selected, i.e. the most under-coordinated atom. The optimized structures obtained are shown in Figure 107.

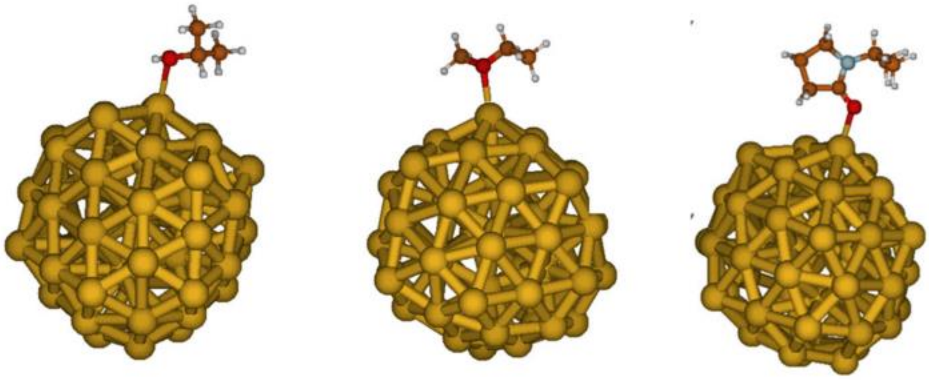

Figure 107. The DFT optimized structures of the monomer of the stabilizing agents (PVA on the left, PEG in the center and PVP on the right) adsorbed on the Au_{55} cluster model.

From the geometries obtained we see that the adsorption occurs via the O atom for the three monomeric units, in particular with the hydroxyl group of PVA, the ether oxygen of PEG and the carboxylic group of PVP. The Au-O distances are reported in Table 21.

Table 21. Energy of adsorption and distance Au-O for PVA, PEG and PVP monomers on Au_{55} cluster.

Stabilizing Agent	Eads (kCal/mol)	Distance Au-O (Å)
PVA	-28.7	2.50
PEG	-31.6	2.47
PVP	-36.8	2.31

From the Au-O distance we see that PVA is the least bound to the gold nanoparticle, since it features a greater distance, followed by PEG and PVP. Moreover, we can see that also the Eads of PVA on Au_{55} cluster is lower than PEG and PVP, so the interaction is weaker. These results agree with experimental studies that demonstrate that by washing PVA-stabilised catalysts with water, this is washed away at relatively low temperatures and more easily than PEG and PVP. [165-167]

5.5 Conclusions and future work

The oxidation reaction of glucose (GLU) to glucaric acid (GLA) was studied computationally using a cluster approach. In particular, experimental results obtained previously in the research group were analyzed, testing catalysts of gold nanoparticles supported on activated carbons in the oxidation reaction of GLU in liquid phase in an autoclave, using oxygen as oxidizing agent in presence of a base (NaOH). The tested catalysts were synthesized using the sol-immobilization technique. The effect of three different stabilizing agents was evaluated (i.e. PVA, PEG and PVP) studying the possible correlation between the stabilizing agent used, its quantity and the activity, selectivity and stability of the catalyst for the reaction in question. Experimental studies have shown that using PVA as a stabilizing agent the highest yield (22%) in GLA is obtained. Furthermore, by testing the catalyst at different reaction times, it was seen that, after an hour of reaction, the yield of GLA does not increase further, while the yield of the other products decreases slightly. A computational study was therefore carried out by optimizing Au_{55} gold cluster structures and studying the adsorption of the main reaction molecules in order to better understand these deactivation phenomena.

By studying the adsorption of GLU, gluconic acid (GLO) and GLA, it was seen that on the clean Au_{55} gold nanoparticle the adsorption energy is almost the same. In the presence of hydroxyl groups, however, GLA interacts more strongly with the catalyst surface, due to the presence of an additional carboxylic acid group, which favors the formation of hydrogen bonds between the molecule and the hydroxyls on the catalyst surface.

On the cluster structures obtained, the adsorption of the three stabilizing agents PVA, PEG and PVP was studied. From the computational results obtained, it was seen that PVA interacts less strongly with the nanoparticle, followed by PEG and PVP. As a result, this can be washed away more easily after synthesis, leaving the reactive sites free and thus favoring the reaction.

Subsequent computational studies can be carried out in order to better understand the reaction mechanism, which is still little known for the reaction step from GLO to GLA, with the aim of subsequently optimizing the catalytic process.

References

[1] Amato, I., The Slow Birth of Green Chemistry, Science, 1993, 259, 1538−1541

[2] Anastas, P.; Eghbali, N., Green Chemistry: Principles and Practice, Chem. Soc. Rev., 2010, 39, 301-312

[3] EA. IEA bioenergy Task 42 on biorefineries: co-production of fuels, chemicals, power and materials from biomass. In: Minutes of the third Task meeting, Copenhagen, Denmark, 25–26 March 2007

[4] Cherubini, F., The biorefinery concept: Using biomass instead of oil for producing energy and chemicals, Energy Conversion and Management Volume 51, Issue 7, 2010, 1412-1421

[5] Pileidis, F. D.; Titirici, M. M., Levulinic Acid Biorefineries: New Challenges for Efficient Utilization of Biomass. ChemSusChem 9, 2016, 562–582

[6] Liu, W.; Jiang, H.; Yu, H., Thermochemical conversion of lignin to functional materials: a review and future directions. Green Chem. 17, 2015, 4888–4907

[7] Cho, E.J.; Trinh, L.P.T.; Song, Y.; Lee, Y.G.; Hyeun-Jong, B.; Mint: Bioconversion of biomass waste into high value chemicals. Bioresource Technology, 2019, 298:122386

[8] Peña, J.; Martínez, P.; Cortés, M.; Chirivi, N.; Geney, L.M., Mint: Uso energético de la biomasa a través del proceso de gasificación, 2017

[9] Moragues, J.; Rapallini, A., Energía de la biomasa. 2017

[10] Kumar, M.; Oyedun, A.O.; Mint A.K., A review on the current status of various hydrothermal technologies on biomass feedstock. Renewable Sustainable Energy Reviews, Elsevier, 2018, 81(P2): 1742-1770

[11] Zhang, L.; Xu, C.; Mint, C.P., Overview of recent advances in thermo-chemical conversion of biomass, Energy Conversion and Management, 2010, 51:969-982

[12] Taherzadeh, M.; Karimi, K., Mint: Acid-based hydrolysis processes for ethanol from lignocellulosic materials: A bioethanol review, BioResources, 2007, 2:707-738

[13] Hamelinck, C. N.; Van Hooijdonk, G.; Faaij, A.P.C., Ethanol from lignocellulosic biomass: Techno-economic performance in short-, middle- and long-term. Biomass and Bioenergy 28, 2005, 384–410

[14] Kamm, B.; Gruber, P.; Kamm, M., Biorefineries – Industrial Processes and Products. Weinheim : Wiley-VCH, 2006

[15] Werpy, T.; Petersen, G., Top Value Added Chemicals from Biomass: Volume I -- Results of Screening for Potential Candidates from Sugars and Synthesis Gas, DOE/GO-102004-1992, 15008859; 2004,

[16] Rackemann, D.W.; Doherty, W.O., The Conversion of Lignocellulosics to Levulinic Acid. Biofuels, Bioprod. Biorefin., 2011, 5 (2), 198−214

[17] Grilc, M.; Likozar, B., Levulinic acid hydrodeoxygenation, decarboxylation and oligmerization over NiMo/Al2O3 catalyst to bio-based value-added chemicals: Modelling of mass transfer, thermodynamics and micro-kinetics, Chemical Engineering Journal Volume 330, 2017, 383-397

[18] Chatzidimitriou, A.; Bond, J.Q., Oxidation of levulinic acid for the production of maleic anhydride: breathing new life into biochemicals, Green Chem., 2015, 17, 4367-4376

[19] Shao, Y.; Ba, B.; Sun, K.; Gao, G.; Fan, M.; Wang, J.; Fan, H.; Zhang, L.; Hu, X., Selective production of γ-valerolactone or 1,4-pentanediol from levulinic acid/esters over Co-based catalyst: Importance of the synergy of hydrogenation sites and acidic sites, Chemical Engineering Journal, Volume 429, 2022, 132433

[20] Zeikus, J.G.; Jain, M.K.; Elankovan, P., Biotechnology of succinic acid production and markets for derived industrial products, Appl. Microbiol. Biotechnol 51, 1999, 545–552

[21] Saxena, R.K.; Saran, S.; Isar, J.; Kaushik, R., Production and Applications of Succinic Acid, Current Developments in Biotechnology and Bioengineering Production, Isolation and Purification of Industrial Products, 2017, 601-630

[22] Li, J.; Tian, W.P.; Wang, X.; Shi, L., Chem. Eng. J. 175, 2011, 417–422

[23] Dunlop, A.P.; Shelbert, S., Preparation of succinic acid., 1952

[24] Podolean, I.; Kuncser, V.; Gheorghe, N.; Macovei, D.; Parvulescu, V.I.; Coman, S.M., Ru-based magnetic nanoparticles (MNP) for succinic acid synthesis from levulinic acid. *Green Chem.* 15, 2013, 3077

[25] Dutta, S.; Yu, I.K.M.; Tsang, D.C.W.; Hau, Y.; Ok, Y.S.; Sherwood, J.; Clark, J.H., Green synthesis of gamma-valerolactone (GVL) through hydrogenation of biomass-derived levulinic acid using non-noble metal catalysts: A critical review., *Chem. Eng. J.* 372, 2019, 992–1006

[26] Horváth, I. T.; Mehdi, H.; Fábos, V.; Boda, L.; Mika, L. T., γ-Valerolactone-a sustainable liquid for energy and carbon-based chemicals. *Green Chem.* 10, 2008, 238–242

[27] Fábos, V.; Koczó, G.; Mehdi, H.; Boda, L.; Horváth, I. T., Bio-oxygenates and the peroxide number: A safety issue alert. *Energy Environ. Sci.* 2, 2009, 767–769

[28] Rackemann, D. W.; Doherty, W. O., The Conversion of Lignocellulosics to Levulinic Acid, Biofuels, Bioprod. Biorefin., 2011, 5 (2), 198–214

[39] Zhang, J.; Wu, S.; Li, B.; Zhang, H., Advances in the Catalytic Production of Valuable Levulinic Acid Derivatives, ChemCatChem, 2012, 4, 1230-1237

[30] Mehdi, H.; Fabos, V.; Robert, T.; Bodor, A.; Mika, L.T.; Horvath, I.T., Top. Catal., 2008, 48, 49 – 54

[31] Li, W.; Xie, J.-H.; Lin, H.; Zhou, Q.-L., Green Chem., 2012, 14, 2388 – 2390

[32] Ortiz-Cervantes, C.; Flores-Alamo, M.; Garcia, J.J., ACS Catal., 2015, 5, 1424 – 1431

[33] Galletti, A.M.R.; Antonetti, C.; De Luise, V.; Martinelli, M., A sustainable process for the production of γ-valerolactone by hydrogenation of biomass-derived levulinic acid, Green Chem, 14, 2012, 688-694

[34] Primo, A.; Concepción, P.; Corma, A., Synergy between the metal nanoparticles and the support for the hydrogenation of functionlized carboxylic acids to diols on Ru/TiO2. Chem. Commun., 2011, 47, 3613–3615

[35] Luo, W.; Sankar, M.; Beale, A.M.; He, Q.; Kietly, C.J.; Bruijnincx, P.C.A.; Weckhuysen, B.M., High performing and stable supported nano-alloys for the catalytic hydrogenation of levulinic acid to γ-valerolactone. Nat. Commun,. 2015, 6, 1–10

[36] Feng, J.; Li, M.; Zhong, Y.; Xu, Y.; Meng, X.; Zhao, Z.; Feng, C., Hydrogenation of levulinic acid to γ-valerolactone over Pd@UiO-66-NH2 with high metal dispersion and excellent reusability; Microporous and Mesoporous Materials Volume 294, 2020, 109858

[37] Yan, K.; Lafleur, T.; Liao, J., Facile synthesis of palladium nanoparticles supported on multi-walled carbon nanotube for efficient hydrogenation of biomass-derived levulinic acid; J Nanopart Res, 2013, 15,1906

[38] Sun, D.; Ohkubo, A.; Asami, K.; Katori, T.; Yamada, Y.; Sato, S., Vapor-phase hydrogenation of levulinic acid and methyl levulinate to γ-valerolactone over non-noble metal-based catalysts, Molecular Catalyis 437, 2017 105-113

[39] Komanoya, T.; Nakajima, K.; Kitano, M.; Hara, M., Synergistic Catalysis by Lewis Acid and Base Sites on ZrO2 for Meerwein- Ponndorf-Verley Reduction. J. Phys. Chem. C, 2015, 119 (47), 26540-26546

[40] Tabanelli, T., Unrevealing the hidden link between sustainable alkylation and hydrogen transfer processes with alcohols, Current Opinion in Green and Sustainable Chemistry, 2021, 29, 100449

[41] Gyngazova, M. S.; Grazia, L.; Lolli, A.; Innocenti, G.; Tabanelli, T.; Mella, M.; Albonetti, S.; Cavani, F., Mechanistic insights into the catalytic transfer hydrogenation of furfural with methanol and alkaline earth oxides, Journal of Catalysis 372, 2019, 61-73

[42] Grazia, L.; Bonincontro, D.; Lolli, A.; Tabanelli, T.; Lucarelli, C.; Albonetti, S.; Cavani, F., Exploiting H-transfer as a tool for the catalytic reduction of bio-based building blocks: the gas-phase production of 2-methylfuran using a FeVO4 catalyst, Green Chem., 2017, 19, 4412-4422

[43] Rojas-Buzo, S.; Garcia-Garcia, P.; Corma, A., Catalytic transfer hydrogenation of biomass-derived carbonyls over hafnium- based metal–organic frameworks. ChemSusChem, 2018, 11: 432-438

[44] Scholz, D.; Aelli, C.; Hermans, I., Catalytic transfer hydrogenation/hydrogenolysis for reductive upgrading of furfural and 5-(hydroxymethyl)furfural, ChemSusChem, 2014, 7, 268-275

[45] Garcia, B.; Moreno, J.; Iglesias, J.A.; Melero, J.; Morales, G., Transformation of glucose into sorbitol on raney nickel catalysts in the absence of molecular hydrogen: sugar disproportionation vs catalytic hydrogen transfer. Top Catal, 2019, 62: 570-578

[46] Chia, M.; Dumesic, J.A., Liquid-Phase Catalytic Transfer Hydrogenation and Cyclization of Levulinic Acid and Its Esters to γ- Valerolactone over Metal Oxide Catalysts. Chem. Commun., 2011, 47

[47] Komanoya, T.; Nakajima, K.; Kitano, M.; Hara, M., Synergistic Catalysis by Lewis Acid and Base Sites on ZrO 2 for Meerwein–Ponndorf–Verley Reduction. J. Phys. Chem. C, 2015, 119 (47), 26540–26546

[48] Johnstone, R. A. W.; Wilby, A. H.; Entwistle, I. D., Heterogeneous Catalytic Transfer Hydrogenation and Its Relation to Other Methods for Reduction of Organic Compounds. Chem. Rev., 1985, 85 (2), 129–170

[49] Tang, X.; Hu, L.; Sun, Y.; Zhao, G.; Hao, W.; Lin, L.; Conversion of Biomass-Derived Ethyl Levulinate into γ-Valerolactone via Hydrogen Transfer from Supercritical Ethanol over a ZrO2 Catalyst, RSC Adv. 2013, 3 (26), 10277

[50] Xie, Y.; Li, F.; Wang, J.; Wang, R.; Wang, H.; Liu, X.; Xia, Y., Catalytic transfer hydrogenation of ethyl levulinate to γ-valerolactone over a novel porous Zirconium trimetaphosphate, Molecular Catalysis, 442, 2017, 107-114

[51] Vásquez, P. B.; Tabanelli, T.; Monti, E.; Albonetti, S.; Bonincontro, D.; Dimitratos, N.; Cavani, F., Gas-Phase Catalytic Transfer Hydrogenation of Methyl Levulinate with Ethanol over ZrO2, ACS Sustain. Chem. Eng., 2019, 7 (9), 8317-8330

[52] Tabanelli, T.; Paone, E.; Vasquez, P.B.; Pietropaolo, R.; Cavani, F.; Mauriello, F., Transfer Hydrogenation of Methyl and Ethyl Levulinate Promoted by a ZrO2 Catalyst: Comparison of Batch vs Continuous Gas-Flow Conditions, ACS Sustain. Chem. Eng., 2019, 7,9937-9947

[53] Chuah, G.; Jaenicke, S.; Cheong, S.; Chan, K. The Influence of Preparation Conditions on the Surface Area of Zirconia. Appl. Catal. Gen., 1996, 145 (1–2), 267–284

[54] Christensen, A.; Carter, E. A. First-Principles Study of the Surfaces of Zirconia. Phys. Rev. B 1998, 58 (12), 8050–8064

[55] Ricca, C.; Ringuedé, A.; Cassir, M.; Adamo, C.; Labat, F., A Comprehensive DFT Investigation of Bulk and Low-Index Surfaces of ZrO2 Polymorphs. J. Comput. Chem. 2015, 36 (1), 9–21

[56] Štefanić, G.; Musić, S., Croat. Chem. Acta 2002, 75, 727

[57] Garvie, R. C.; Hanink, R. H. J.; Pascoe, R.J., Shape memory behaviour in partially stabilized zirconia ceramics, Nature, 1975, 258, 703

[58] Puigdollers, A. R.; Illas, F.; Pacchioni, G., Structure and Properties of Zirconia Nanoparticles from Density Functional Theory Calculations. J. Phys. Chem. C, 2016, 120 (8), 4392–4402

[59] Eichler, A.; Kresse, G. First-Principles Calculations for the Surface Termination of Pure and Yttria-Doped Zirconia Surfaces. Phys. Rev. B 17, 2004, 69(4)

[60] Zirconium and Hafnium Statistics and Information, minerals.usgs.gov.

[61] Tiloke, C.; Chuturgoon, A.A., in Nanoarchitectonics for Smart Delivery and Drug Targeting, 2016, 897-942

[62] Karmani L.; Labar D.; Valembois V.; Bouchat V., Nagaswaran PG: Antibody functionalized nanoparticles for imaging cancer: influence of conjugation to gold nanoparticles on the biodistribution of Zr-labeled cetuximab in mice; *Contrast Media Mol Imaging.* 8, 2013, 402-408

[63] Haruta, M.; Kobayashi, T.; Sano, H.; Yamada, N., Novel Gold Catalysts for the Oxidation of Carbon Monoxide at a Temperature far Below 0 °C. Chem. Lett. 16,1987, 405–408

[64] Hutchings, G. J., Vapor phase hydrochlorination of acetylene: correlation of catalytic activity of supported metal chloride catalysts. J. Catal. 96, 1985, 292–295

[65] Kim, K. J.; Ahn, H. G., Complete oxidation of toluene over bimetallic Pt–Au catalysts supported on ZnO/Al2O3. *Applied Catalysis B: Environmental*, 91(1-2), 2009, 308-318

[66] Prati, L.; Martra, G., New gold catalysts for liquid phase oxidation. *Gold Bull.* 32, 1999, 96–101

[67] Qian, Z.; Park, S. J., Silver seeds and aromatic surfactants facilitate the growth of anisotropic metal nanoparticles: gold triangular nanoprisms and ultrathin nanowires. Chemistry of Materials, 26(21), 2014, 6172-6177

[68] Pamies, R.; Cifre, J.G.H.; Espín, V.F.; Collado-González, M.; Baños, F.G.D.; García de la Torre, J., Aggregation behaviour of gold nanoparticles in saline aqueous media, Journal of Nanoparticle Research volume 16, Article number: 2376, 2014

[69] Thomas, L.H., Proc. Cambridge Phil. Soc., 23, 1927, 542

[70] Fermi, E., Rend. Accad. Naz. Lincei, 6, 1927, 602

[71] Becke, A. D., *J. Chem. Phys*., 84, 1986, 4524

[72] Perdew, J.P., *Phys. Rev.* B, 33, 1986, 8822

[73] Cramer, C.J., Essentials of Computational Chemistry, 2004, 165-179, 249-268, 393- 394

[74] P.J. Stephens, F.J. Devlin, C.F. Chabalowski, M.J. Frisch, *J. Phys. Chem.*, 98, 11623- 11627 (1994)
[75] A. D. McLean and G. S. Chandler, *J. Chem. Phys.,* 72, 5639-5948 (1980)
[76] Schäfer, A.; Horn, H.; Ahlrichs, R., *J. Chem. Phys*., 97, 1992, 2571-2577
[77] Andrae, U.; Häußermann, M. D.; Stoll, H.; Preuß, H., Energy-adjusted ab initio pseudopotentials for the second and third row transition elements, Theor. Chim. Acta 77, 1990, 123-141
[78] Ralphs, K.; D'Agostino, C.; Burch, R.; Chansai, S.; Gladden, L.F.; Hardacre, C.; James, S.L.; Mitchel, J.; Taylor, S.F.R., Assessing the surface modifications following the mechanochemical preparation of a Ag/Al_2O_3 selective catalytic reduction catalyst, Catal. Sci. Technol. 4, 2014, 531-539
[79] D'Agostino, C.; Chansai, S.; Bush, I.; Gao, C.; Mantle, M.D.; Hardacre, C.; James, S.L.; Gladden, L.F., Assessing the effect of reducing agents on the selective catalytic reduction of NOx over Ag/Al_2O_3 catalysts, Catal. Sci. Technol. 6, 2016, 1661-1666
[80] Haider, M.H.; D'Agostino, C.; Dummer, N.F.; Mantle, M.D.; Gladden, L.F.; Knight, D.W.; Willock, D.J.; Morgan, D.J.; Taylor, S.H.; Hutchings, G.J., The Effect of Grafting Zirconia and Ceria onto Alumina as a Support for Silicotungstic Acid for the Catalytic Dehydration of Glycerol to Acrolein, Chemistry A European Journal 20, 2014, 1743-1752
[81] D'Agostino, C.; Mitchell, J.; Mantle, M.D.; Gladden, L.F., Interpretation of NMR Relaxation as a Tool for Characterising the Adsorption Strength of Liquids inside Porous Materials, Chemistry-A European Journal 20, 2014, 13009-13015.
[82] Di Carmine, G.; Forster, L.; Wang, S.; Parlett, C.; Carlone, A.; D'Agostino, C., NMR relaxation time measurements of solvent effects in an organo-catalysed asymmetric aldol reaction over silica SBA-15 supported proline, Reaction Chemistry & Engineering 7 (2), 2022, 269-274
[83] Gaussian 16, Revision C.01, M. J. Frisch, G. W. Trucks, H. B. Schlegel, G. E. Scuseria, M. A. Robb, J. R. Cheeseman, G. Scalmani, V. Barone, G. A. Petersson, H. Nakatsuji, X. Li, M. Caricato, A. V. Marenich, J. Bloino, B. G. Janesko, R. Gomperts, B. Mennucci, H. P. Hratchian, J. V. Ortiz, A. F. Izmaylov, J. L. Sonnenberg, D. Williams-Young, F. Ding, F. Lipparini, F. Egidi, J. Goings, B. Peng, A. Petrone, T. Henderson, D. Ranasinghe, V. G. Zakrzewski, J. Gao, N. Rega, G. Zheng, W. Liang, M. Hada, M. Ehara, K. Toyota, R. Fukuda, J. Hasegawa, M. Ishida, T. Nakajima, Y. Honda, O. Kitao, H. Nakai, T. Vreven, K. Throssell, J. A. Montgomery, Jr., J. E. Peralta, F. Ogliaro, M. J. Bearpark, J. J. Heyd, E. N. Brothers, K. N. Kudin, V. N. Staroverov, T. A. Keith, R. Kobayashi, J. Normand, K. Raghavachari, A. P. Rendell, J. C. Burant, S. S. Iyengar, J. Tomasi, M. Cossi, J. M. Millam, M. Klene, C. Adamo, R. Cammi, J. W. Ochterski, R. L. Martin, K. Morokuma, O. Farkas, J. B. Foresman, and D. J. Fox, Gaussian, Inc., Wallingford CT (2016)
[84] Jain, A.; Ong, S.P.; Hautier, G.; Chen, W.; Richards, W.D.; Dacek, S.; Cholia, S.; Gunter, D; Skinner, D.; Ceder, G.; Persson, K.A.The Materials Project: A Materials Genome Approach to Accelerating Materials Innovation APL Materials, 2013, 1(1), 011002
[85] Bhattacharyya, K.; Danon, A.; Vijayan, B.K.; Gray, K.A.; Stair, B.C.; Weitz, E., Role of the Surface Lewis Acid and Base Sites in the Adsorption of CO_2 on Titania Nanotubes and Platinized Titania Nanotubes: An in Situ FT-IR Study, The Journal of Physical Chemistry C 117 (24), 2013, 12661-12678
[86] Chen, H.-Y. T.; Tosoni, S.; Pacchioni, G., A DFT Study of the Acid–Base Properties of Anatase TiO_2 and Tetragonal ZrO_2 by Adsorption of CO and CO_2 Probe Molecules. Surf. Sci. 652, 2016, 163-171
[87] Kouva, S.; Andersin, J.; Honkala, K.; Lehtonen, J.; Leffertsac, L.; Kanervo, J., Water and carbon oxides on monoclinic zirconia: Experimental and computational insights, Phys. Chem. Chem. Phys. 16, 2014, 20650-20664
[88] Chen, T.; Qin, Z.; Qi, Y.; Deng, T.; Ge, X.; Wang, J.; Hou, X., Degradable Polymers from Ring-Opening Polymerization of α-Angelica Lactone, a Five-Membered Unsaturated Lactone. Polym. Chem. 2 (5), 2011, 1190-1194
[89] Mascal, M.; Dutta, S.; Gandarias, I., Hydrodeoxygenation of the Angelica Lactone Dimer, a Cellulose-Based Feedstock: Simple, High-Yield Synthesis of Branched C7-C10 Gasoline-like Hydrocarbons. Angew. Chem. Int. Ed. 53, 2014 1854-1857
[90] Wang, X.J.; Hong, M., Lewis-Pair-Mediated Selective Dimerization and Polymerization of Lignocellulose-Based b-Angelica Lactone into Biofuel and Acrylic Bioplastic. Angew. Chem. 132, 2020, 2686-2690

[91] Bozell, J.J.; Petersen, G.R., Technology development for the production of biobased products from biorefinery carbohydrates—the US Department of Energy's "Top 10", Green Chem., 2010, 12, 539–554

[92] Perego, C.; Bianchi, D., Biomass upgrading through acid–base catalysis, Chemical Engineering Journal Volume 161, Issue 3, 2010, 314-322

[93] Mamman, A.S.; Lee, J.-M.; Kim, Y.-C.; Hwang, I.T.; Park, N.-J.; Hwang, J.K.; Chang, J.-S.; Hwang, J.S., Furfural: Hemicellulose/xylosederived biochemical, Biofpr, Volume2, Issue5, 2008, 438-454

[94] Sain, B.; Chaudhuri, A.; Borgohain, J. N.; Baruah, B. P.; Ghose, J. L., (1982). Furfural and furfural-based industrial chemicals. J. Sci. Ind. Res., 41, 1982, 431-438

[95] The Chemistry and Technology of Furfural and its Many By-Products 1st Edition - February 9, 2000
Author: K.J. Zeitsch

[96] Hoydonckx, H. E.; Van Rhijn, W. M., Application of novel furan resins in composites. JEC Magazine, 2008

[97] Tachibana, Y.; Masuda, T.; Funabashi, M.; Kasuya, K.; Kunioka, M., Synthesis of Biomass-Based Monomers from Biomass-Based Furfural for Polyesters and Evaluation of Their Biomass Carbon Ratios, Biobased Monomers, Polymers, and Materials, 2012, 7, 91-110

[98] Vazquez, M.; Oliva, M.; Tellez-Luis, S. J.; Ramirez, Ax, J., Hydrolysis of sorghum straw using phosphoric acid: evaluation of furfural production. Bioresour. Technol., 2007, 98, 3053-3060

[99] Pirolini, A. P. (2015). Materials used in space shuttle thermal protection systems. Available at: http://www.azom.com (accessed 2 April, 2015)

[100] Yuan, Q.; Zhang, D.; van Haandel, L.; Ye, F.; Xue, T.; Hensen, E.J.; Guan, Y., Selective liquid phase hydrogenation of furfural to furfuryl alcohol by Ru/Zr-MOFs, J. Mol., Catal. A-Chem. 2015, 406, 58-64

[101] Pang, S.H.; Medlin, J.W., Adsorption and Reaction of Furfural and Furfuryl Alcohol on Pd(111): Unique Reaction Pathways for Multifunctional Reagents, ACS Catal. 2011, 1, 1272-1283

[102] Kijeński, J.; Winiarek, P.; Paryjczak, T:; Lewicki, A.; Mikołajska, A., Platinum deposited on monolayer supports in selective hydrogenation of furfural to furfuryl alcohol, Appl. Catal., A: Gen. 2002, 233, 171-182

[103] Xu, L.; Nie, R.; Lyu, X.; Wang, J.; Lu, X., Selective hydrogenation of furfural to furfuryl alcohol without external hydrogen over N-doped carbon confined Co catalysts, Fuel Process. Technol., 2020, 197, 106205

[104] Jiménez-Gómez, C.P.; Cecilia, J.A:; Moreno-Tost, R.; Torres, P.M., Gas-phase hydrogenation of furfural over Cu/CeO2 catalysts, Top. Catal. 2017, 60, 1040-1053

[105] Pang, S.H.; Schoenbaum, C.A.; Schwartz, D.K.; Medlin, J.W., Directing reaction pathways by catalyst active-site selection using self-assembled monolayers, ACS Catal. 2014, 4, 3123-3131

[106] Cao, D.; Xia, S.; Pan, P.; Zeng, H.; Li, C.; Peng, Y. Light-driven MPV-type reduction of aryl ketones/aldehydes to alcohols with isopropanol under mild conditions. Green Chem. 2021, 23, 7539–7543

[107] Zhang, J.; Dong, K.; Luo,W.; Guan, H. Selective transfer hydrogenation of furfural into furfuryl alcohol on Zr-containing catalysts using lower alcohols as hydrogen donors. ACS Omega 2018, 3, 6206–6216

[108] Yang, J.; Guo, H.; Shen F., Highly Efficient Transfer Hydrogenation of Biomass-Derived Furfural to Furfuryl Alcohol over Mesoporous Zr-Containing Hybrids with 5-Sulfosalicylic Acid as a Ligand, Int. J. Environ. Res. Public Health, 2022, *19*(15), 9221

[109] Wang, D. S.; Li, Y.D., Bimetallic Nanocrystals: Liquid-Phase Synthesis and Catalytic Applications, Adv. Mater., 2011, 23, 1044–1060

[110] Stamenkovic, V.R.; Fowler, B.; Mun, B.S.; Wang, G.; Ross, P.N.; Lucas, C.A.; Markovic, N.M., Improved oxygen reduction activity on Pt3Ni(111) via increased surface site availability, Science 315 (2007) 493-7

[111] Tao, F.; Grass, M.E.; Zhang, Y.; Butcher, D.R.; Renzas, J.R.; Liu, Z.; Chung, J.Y.; Mun, B.S.; Salmeron, M.; Somorjai, G.A., Reaction-driven restructuring of Rh-Pd and Pt-Pd core-shell nanoparticles, Science 322, 2008, 932-4

[112] Lim, B.; Jiang, M.; Camargo, P.H.C.; Cho, E.C.; Tao, J.; Lu, X.; Zhu, Y; Xia, X., Science 324 (2009) 1302

[113] Omori, T.; Ando, K.; Okano, M.; Xu, X.; Tanaka, Y.; Ohnuma, I.; Kainuma, R.; Ishida, K., Science 333 (2011) 68

[114] González, E.; Arbiol, J.; Puntes, V.F., Carving at the nanoscale: sequential galvanic exchange and Kirkendall growth at room temperature, Science 334, 2011, 1377-80

[115] Liu, X.; Wang, D.; Li,Y., Synthesis and catalytic properties of bimetallic nanomaterials with various architectures, Nanotoday, Volume 7, Issue 5, 2012, 448-466

[116] Kyriakou, G.; Boucher, M.B.; Jewell, A.D.; Lewis, E.A.; Lawton, T.J.; Baber, A.E.; Tierney, H.L.; Flytzani-Stephanopoulos, M.; Sykes, E.C.H., Isolated Metal Atom Geometries as a Strategy for Selective Heterogeneous Hydrogenations, Science 335, 2012, 1209

[117] Yang, L.; Hu, C.; Wang, J.; Yang, Z.; Guo, Y.; Bai, Z.; Wang, K., Facile synthesis of hollow palladium/copper alloyed nanocubes for formic acid oxidation, Chem. Commun. 47, 2001, 8581

[118] Yu, X.; Wang, D.; Peng, Q.; Li, Y., High performance electrocatalyst: Pt–Cu hollow nanocrystals, Chem. Commun. 47, 2011, 8094

[119] Liu, X.; Li, X.; Wang, S.; Yu, R.; Cui, Y.; Peng, Q.; Li, Y., Palladium/tin bimetallic single-crystalline hollow nanospheres, Chem. Commun. 48, 2012, 1683

[120] Huang, X.; Tang, S.; Liu, B.; Ren, B.; Zheng, N., Enhancing the photothermal stability of plasmonic metal nanoplates by a core-shell architecture, Adv. Mater. 23, 2011, 3420

[121] Kim, D.; Lee, Y.W.; Lee, S.B.; Han, S.W., Convex polyhedral Au@Pd core-shell nanocrystals with high-index facets, Angew. Chem. Int. Ed. 51, 2012, 159

[122] Xu, J.; Wilson, A.R.; Rathmell, A.R.; Howe, J.; Chi, M.; Wiley, B.J., Synthesis and Catalytic Properties of Au-Pd Nanoflowers, ACS Nano 5, 2011, 6119

[123] Taufany, F.; Pan, C.J.; Rick, J.; Chou, H.L.; Tsai, M.C.; Hwang, B.J.; Liu, D.G.; Lee, J.F.; Tang, M.T.; Lee, Y.C.; Chen, C.I., Kinetically controlled autocatalytic chemical process for bulk production of bimetallic core-shell structured nanoparticles, ACS Nano 5, 2011, 9370

[124] Singh, S.K.; Singh, A.K.; Aranishi, K.; Xu, Q.; Am, J., Noble-metal-free bimetallic nanoparticle-catalyzed selective hydrogen generation from hydrous hydrazine for chemical hydrogen storage, Chem. Soc. 133, 2011, 1963

[125] Lee, Y.W.; Kim, M.; Kang, S.W.; Han, S.W., Polyhedral bimetallic alloy nanocrystals exclusively bound by {110} facets: Au-Pd rhombic dodecahedra, Angew. Chem. Int. Ed. 50, 2011, 3466

[126] Sharma, A.K.; Mehara, P.; Das, P., Recent Advances in Supported Bimetallic Pd−Au Catalysts:Development and Applications in Organic Synthesis with Focused Catalytic Action Study, ACS Catal. 2022, 12, 11, 6672–6701

[127] Du, Y.-P.; Bahmanpour, A.M.; Milošević, L.; Héroguel, F.; Mensi, M.D.; Kröcher, O.; Luterbacher; J.S., Engineering the ZrO2−Pd Interface for Selective CO2 Hydrogenationby Overcoating an Atomically Dispersed Pd Precatalyst, ACS Catal. 2020, 10, 20, 12058–12070

[128] Lewkowski J., Synthesis, chemistry and applications of 5-hydroxymethyl-furfural and its derivatives, Archive of Organic Chemistry, 2001, Issue 1, pp. 17-54

[129] Sousa, A.F.; Vilela, C.; Fonseca, A.C.; Matos, M.; Freire, C.S.R.; Gruter, G.-J. M.; Coelho, J.F.J.; Silvestre, A.J.D., Biobased polyesters and other polymers from 2, 5-furandicarboxylic acid: a tribute to furan excellency. Sousa A F, et al. Polym. Chem. 6(33), 2015, 5961-5983

[130] Deng, J.; Liu, X.; Li, C.; Jianga, Y.; Zhua, J., Synthesis and properties of a bio-based epoxy resin from 2, 5-furandicarboxylic acid (FDCA). Deng J, et al. Royal Society of Chemistry Advances 5(21), 2015, 15930-15939

[131] Li, H.-H.; Niu, Z.; Chen, L.; Jiang, H.-B.; Wang, Y.-P.; Cheng, P., Three luminescent metal organic frameworks constructed from trinuclear zinc (ii) clusters and furan-2, 5-dicarboxylate, CrystEngComm 17(27), 2015, 5101-5109

[132] Lomelí-Rodríguez, M.; Corpas-Martínez, J.R.; Willis, S.; Mulholland, R.; Lopez-Sanchez, J.A., Synthesis and Characterization of Renewable Polyester Coil Coatings from Biomass-Derived Isosorbide, FDCA, 1,5-Pentanediol, Succinic Acid, and 1,3-Propanediol, Polymers, 2018,10, 600

[133] Besson, M.; Gallezot, P., in Fine Chemicals through Heterogeneous Catalysis, ed. R. A. Sheldon and H. van Bekkum, Wiley-VCH, Weinheim, New York, Chichester, Brisbane, Singapore, Toronto, 2001, pp. 491–518

[134] Ban, H.; Zhang, Y.; Chen, S.; Cheng, Y.; Pan, T.; Wang, L.; Li, X., Production of 2,5-Furandicarboxylic Acid by Optimization of Oxidation of 5-Methyl Furfural over Homogeneous Co/Mn/Br Catalysts, ACS Sustainable Chemistry & Engineering 2020, 8 (21), 8011-8023

[135] Huang, Y.-T.; Wong, J.-J.; Huang, C.-J.; Li, C.-L.; Jang, G.-W. B., 2,5-Furandicarboxylic Acid Synthesis and Use. In Chemicals and Fuels from Bio-Based Building Blocks, Wiley-VCH Verlag GmbH& Co. KGaA: 2016; pp 191-216 83

[136] Partenheimer, W.; Grushin, Vladimir V., Synthesis of 2,5-Diformylfuran and Furan-2,5-Dicarboxylic Acid by Catalytic Air-Oxidation of 5-Hydroxymethylfurfural. Unexpectedly Selective Aerobic Oxidation of Benzyl Alcohol to Benzaldehyde with Metal=Bromide Catalysts. Advanced Synthesis & Catalysis 2001, 343 (1), 102-11

[137] Zhang, Z.; Huber, G. W., Catalytic oxidation of carbohydrates into organic acids and furan chemicals. Chemical Society Reviews 2018, 47 (4), 1351-1390

[138] Albonetti, S.; Lolli, A.; Morandi, V.; Migliori, A.; Lucarelli, C.; Cavani, F., Conversion of 5-hydroxymethylfurfural to 2,5-furandicarboxylic acid over Au-based catalysts: Optimization of active phase and metal–support interaction, Applied Catalysis B: Environmental, Volume 163, February 2015, Pages 520-530

[139] Zhaoa, D.; Sub, T.; Wangd Y.; Varmae, R.S.; Lenb, C., Recent advances in catalytic oxidation of 5-hydroxymethylfurfural, Molecular Catalysis, Volume 495, November 2020, 111133

[140] Hutchings, G.J., Nanocrystalline gold catalysts: a reflection on catalyst discovery and the nature of active sites, Gold Bull. 42 (2009) 260–266

[141] Kuwauchi, Y.; Yoshida, H.; Akita, T.; Haruta, M.; Takeda, S., Intrinsic catalytic structure of gold nanoparticles supported on TiO2, Angew. Chem. 124 (2012) 7849–7853,

[142] Song, W.; Hensen, E.J.M., A computational DFT study of CO oxidation on a Au nanorod supported on CeO_2(110): on the role of the support termination, Catal. Sci. Technol. 3 (2013) 3020–3029

[143] Wang, M.; Wang, F.; Ma, J.; Li, M.; Zhang, Z.; Wang, Y.; Zhang, X.; Xu, J., Investigations on the crystal plane effect of ceria on gold catalysis in the oxidative dehydrogenation of alcohols and amines in the liquid phase, Chem. Commun. 50 (2014) 292–294

[144] Casanova, O.; Iborra, S.; Corma, A., Biomass into chemicals: aerobic oxidation of 5-hydroxymethyl-2-furfural into 2,5-furandicarboxylic acid with gold nanoparticle catalysts, ChemSusChem 2 (2009) 1138–1144

[145] Pasini, T.; Piccinini, M.; Blosi, M.; Bonelli, R.; Albonetti, S.; Dimitratos, N.; Lopez-Sanchez, J.A.; Sankar, M.; He, Q.; Kiely, C.J.; Cavani, F., Selective oxidation of 5-hydroxymethyl-2-furfural using supported gold–copper nanoparticles, Green Chem., 2011,13, 2091-2099

[146] Gui, Z.; Cao, W.; Saravanamurugan, S.; Riisager, A.; Chen, L.; Qi, Z., Efficient aerobic oxidation of 5-hydroxymethylfurfural in aqueous media with Au-Pd supported on zinc hydroxycarbonate, ChemCatChem 8 (2016) 3636–3643

[147] Antonyraj, C.A.; Huynh, N.T.T.; Park, S.-K.; Shin, S.; Kim, Y.J.; Kim, S.; Lee, K.-Y.; Cho, J.K., Basic anion-exchange resin (AER)-supported Au-Pd alloy nanoparticles for the oxidation of 5-hydroxymethyl-2-furfural (HMF) into 2,5-furan dicarboxylic acid (FDCA), Appl. Catal. A: General 547 (2017) 230–236

[148] Wang, Q.; Hou, W.; Li, S.; Xie, J.; Li, J.; Zhou, Y.; Wang, J., Hydrophilic mesoporous poly(ionic liquid)-supported Au–Pd alloy nanoparticles towards aerobic oxidation of 5-hydroxymethylfurfural to 2,5-furandicarboxylic acid under mild conditions, Green Chem. 19 (2017) 3820–3830

[149] Villa, A.; Schiavoni, M.; Campisi, S.; Veith, G.M.; Prati, L., Pd-modified Au on carbon as an effective and durable catalyst for the direct oxidation of HMF to 2,5-furandicarboxylic acid, ChemSusChem 6 (2013) 609–612

[150] Davis, S. E.; Zope, B. N.; Davis, R. J. Green Chem. 2012, 14, 143-14

[151] Gao, F.; Goodman, D.W., Pd–Au bimetallic catalysts: understanding alloy effects from planar models and (supported) nanoparticlesw; Chem. Soc. Rev., 2012, 41, 8009–8020

[152] Gorbanev, Y. Y.; Klitgaard, S. K.; Woodley, J.M.; Christensen, C. H.; Riisager, A., Gold-Catalyzed Aerobic Oxidation of 5-Hydroxymethylfurfural in Water at Ambient Temperature Volume2, Issue7 July 20, 2009 Pages 672-675

[153] Davis, S.E.; Zope, B.N.; Davis, R.J., On the mechanism of selective oxidation of 5-hydroxymethylfurfural to 2,5-furandicarboxylic acid over supported Pt and Au catalysts, Green Chem. 14 (2012) 143–147
[154] Abbadi, A.; Gotlieb, K. F.; Meiberg, J. B. M.; Peters, J. A.; van Bekkum, H: New sequestering materials based on the oxidation of the hydrolysis products of lactose; Green Chem., 1, 231–235(1999)
[155] Korzh, E. N.; Sukhotin, A. M: Zh. Prikl. Khim. 54, 2404–2407 (1981)
[156] Walaszek, Z.; Szemraj, J.; Hanausek, M.; Adams, A. K.; Sherman, D-Glucaric acid content of various fruits and vegetables and cholesterol-lowering effects of dietary D glucarate in the rat; U. Nutr. Res., 16, 673–681 (1996)
[157] Sohst, O.; Tollens B., Über krystallisirte Zuckersäure (Zuckerlactonsäure); Liebigs Ann. Chem. 245, 1–27 (1888)
[158] National Institute for Occupational Safety and Health (NIOSH): Approaches to Safe Nanotechnology: Managing the Health and Safety Concerns Associated with Engineered Nanomaterials (March 2009)
[159] Moon, T.S.; Yoon, S.; Lanza, A.M.; Roy-Mayhew, J.D.; Jones, K.L., Prather: Production of Glucaric Acid from a Synthetic Pathway in Recombinant Escherichia coli; *Appl. Environ. Microbiol. 75*, 589–595 (2009)
[160] Monti, E.; Ventimiglia, A.; Forster, L.; Rodrìguez-Aguado, E.; Cecilia, J.A.; Ospitali, F.; Tabanelli, T.; Albonetti, S.; Cavani, F.; Rivalta, I.; D'Agostino, C.; Dimitratos, N. Influence of stabilisers on the catalytic activity of supported Au colloidal nanoparticles for the liquid phase oxidation of glucose to glucaric acid: understanding the catalyst performance from NMR relaxation and computational studies; Green Chem., 2023, 25, 2640
[161] Kru¨ckeberg et al., Eur. Phys. J. D 9, 169 (1999).
[162] A. Herlert et al., J. Electron Spectrosc. Relat. Phenom. 106, 179 (2000)
[163] Häkkinen, H.; Moseler, M.; Kostko, O.; Morgner, N.; Hoffmann, M.A.; Issendorff, B.V., Phys. Rev. Lett., 2004, 93, 093401
[164] Van den Bossche, M., DFTB-Assisted Global Structure Optimization of 13- and 55-Atom Late Transition Metal Clusters, J. Phys. Chem. A, 2019, 123, 3038– 3045
[165] Scurti, S.; Allegri, A.; Liuzzi, F.; Rodríguez-Aguado, E.; Cecilia, J.A.; Albonetti, S.; Caretti, D.; Dimitratos, N. TemperatureDependent Activity of Gold Nanocatalysts Supported on Activated Carbon in Redox Catalytic Reactions: 5-Hydroxymethylfurfural Oxidation and 4-Nitrophenol Reduction Comparison. Catalysts 2022, 12, 323
[166] Liuzzi, F.; Ventimiglia, A.; Allegri, A.; Rodríguez-Aguado, E.; Cecilia, J.A.; Rivalta, I.; Dimitratos, N.; Albonetti, S. Effect of Capping Ligands for the Synthesis of Gold Nanoparticles and on the Catalytic Performance for the Oxidation of 5-Hydroxymethyl-2-furfural. Catalysts 2023, 13, 990.